ION OPTICAL STUDY OF MASS ANALYZERS

A thesis submitted to Osaka University for the degree of Doctor of Philosophy in the Faculty of Science.

Morio Ishihara

March 1991

ABSTRACT

Since new ionization methods were developed in the 1980's, mass spectrometry has evolved to a very significant technique for the investigation in atomic physics, nuclear physics, materials science and, especially, biology and biochemistry. It is absolutely necessary to design and construct a high performance mass analyzer for supporting the progress of mass spectrometry. Here "high performance" means (1) high mass resolution, (2) high mass range, (3) high transmission (sensitivity), and (4) easy ON-LINE combination with another instrument.

This thesis consists of the two following subjects.

(1) Ion optical investigations of a high performance mass spectrometer are completed on the basis of the transfer matrix method with a newly developed parameter search program (MSPLEX) based on the simplex method. Three ion optical systems are designed: (1) a new double focusing mass spectrometer having high mass range; (2) a tandem mass spectrometer with quadrupole triplet interface; and (3) a zoom lens system consisting of a quadrupole-octapole-quadrupole configuration. The instruments employing these ion optical systems are constructed and the ion optical characteristics of the instruments are examined and the results are in good agreement with the theoretical predictions. The main purpose of construction of these instruments is to analyze heavy organic compounds which are important in the field of biochemistry. The results obtained by these instruments are: (1) high resolution mass spectra of biopolymer such as bovine insulin (M.W. 5730); (2) a structure characterization of hemoglobin variant using MS/MS analysis by a tandem mass spectrometer; and (3) a zoomed mass spectrum in high resolution and wide mass range.

(2) In order to design an ion optical system which is applicable to wide spread beam, a new ray tracing program (ELECTRA) is developed on the basis of the charge density method and the Runge-Kutta method. By using this program, the fringing field integrals of a quadrupole lens and the higher-order image aberrations up to seventh-order in the fringing fields of an electrostatic analyzer are calculated. The effect of the imperfect boundary shape of a sector magnet is investigated and the aberration observed for wide beam spread is well explained by this effect. Finally two apparatus are designed: (1) an NMR magnet with wide gap; and (2) a retardation lens system; where the combination of the programs ELECTRA and MSPLEX is skillfully used. These two will become powerful apparatus for atomic and nuclear physics.

CONTENTS

1. INTRODUCTION

Since the early 1980's mass spectrometry has evolved to a very significant technique for the investigation in atomic physics, nuclear physics, materials science and, especially recently, biology and biochemistry. In these studies, it is absolutely necessary to supply a high performance mass analyzer for supporting the progress of mass spectrometry. Here "high performance" means: (1) high mass resolution, (2) high mass range, (3) high transmission (sensitivity) and (4) easy ON-LINE combination with another instrument. In order to develop a high performance mass spectrometer, the following four steps are indispensable:

1) To investigate ion optics.
2) To design a system.
3) To construct it.
4) To examine its performance by experiments.

We report the results of the study along this line. The thesis consists of two subjects.

First, we designed and constructed (1) a high performance mass spectrometer, (2) a tandem mass spectrometer, and (3) a zooming equipment using quadrupole-octapole-quadrupole lenses. Ion optical calculations were done using transfer matrix method. The background and motivation of such study are explained briefly in the following.

In 1981 [1.1] a very powerful ionization technique was introduced in organic mass spectrometry. It was the fast atom bombardment (FAB) ionization which makes it possible to ionize directly large polar molecules such as peptides, carbohydrates and lipids. In FAB, the sample to be analyzed was dissolved in matrix (most case glycerol). Primary Ar or Xe atoms having 5 to 10 keV energy were used to bombard the sample. Subsequently the secondary ions of sample were produced in the protonated form $(M+H)^+$, extracted and focused into a mass analyzer. Since FAB was very simple to operate and gave reproducible secondary ions, it became widely used. Furthermore, since it also allowed the ionization of molecules much larger than previously ionizable by mass spectrometry, a new area of the study of "high-mass-range mass spectrometry" started. Thus instruments with much higher mass range had to be available. In order to satisfy such requirement, we designed and constructed a new double focusing mass spectrometer having large radius of curvature of the central beam in the magnet, which is explained in chapter 2.3.

Although conventional fast atom bombardment mass spectrometry (FAB-MS) primarily generates the protonated molecular ion $(M+H)^+$ of the biopolymer such as peptides, often little fragmentation, which is necessary to obtain reliable structural information, is observed. Fragmentation can be achieved by collision-induced decomposition (CID), in which the $(M+H)^+$ ion collides with a neutral atom (such as helium)[1.2]. In such experiments two mass analyzers in tandem (a tandem mass spectrometer) are used. The first mass analyzer (MS1) selects the $(M+H)^+$ ions of the molecule of interest (the

precursor ion), which are then transmitted into a collision cell where fragmentation takes place. The resulting fragment ions are then mass analyzed in the second mass spectrometer (MS2) and the CID spectrum of the precursor is recorded. The method is referred to as MS/MS. It should be emphasized that MS/MS is very useful for investigating mixtures, because a CID spectrum for each component in the mixture unaffected by other components. There are in principle various ways in which MS/MS experiments can be conducted. For the analysis of reasonably large molecule of unknown structure, high resolution, high mass range and high sensitivity are required. In this case it is necessary to use a four-sector instrument in which both MS1 and MS2 are high mass double focusing magnetic spectrometers. A tandem mass spectrometer with quadrupole triplet interface will be discussed in chapter 2.4.

Since the beam intensity of fragment ions produced by collision - induced decomposition (CID) is very low, an array detector placed in the focal plane is effectively used [1.3]. The detection efficiency is increased by a factor of 100 using an array detector. The development of this type of detector has been directed primarily towards the determination of peptide sequence information using pico- to femto- mol of sample [1.4]. The simultaneously detectable mass ranges of conventional mass spectrometers are usually limited to approximately 5-10%. It is, therefore, necessary to carry out a series of measurements to obtain a complete mass spectrum over a large mass range. To overcome this tedious time and sample consuming procedure, it is desirable to develop a mass spectrometer which can vary mass range which is focused on the array detector. We have developed a zoom lens system consisting of a quadrupole-octapole-quadrupole configuration which is discussed in chapter 2.5.

Second, we have developed a ray tracing program "ELECTRA" and studied some ion optical problems using this program. The background of this study is as follows:

The next requirement for a high performance mass spectrometer is a system which satisfies "high transmission" or in other words " large beam acceptance". For this purpose, we have to pursue the treatment of not only narrow ion beam but also wide spread beam. Then, we know the matrix method itself has following limitations:

1) Only paraxial rays are calculated.
2) The higher-order effects cannot be estimated.
3) The ion optical components that are not specified in the program cannot be calculated.

Accordingly, in order to improve the numerical calculation for a system treating wide spread beams, we have developed a ray tracing program.

The procedure of the ray tracing method is that the field is specified by either an analytical or numerical formula, then the trajectories are calculated by numerically integrating the Lorentz's equation of motion. Thus an arbitrary ion trajectory in an arbitrary field can be obtained; the obtained trajectories include all higher order effects. Therefore the ray tracing method does not have the limitations of paraxial rays.

The most difficult part of the ray tracing method is to specify the electromagnetic field. The accuracy of the specified field is very important because the accuracy of calculated trajectories strongly depend on it. The field can be specified by using (1)

measured values, (2) approximation formula, (3) exact analytical formula or (4) values obtained by solving Laplace's equation numerically. For special cases the specification using the manners (1), (2) or (3) is possible, but in general case the field can only be specified in the manner(4). For this purpose we studied the numerical field calculation method based on the charge density method [1.5], which is described in chapter 3.2.

The next step of the ray tracing method is to integrate the equations of motion. The Runge-Kutta method was employed because it permits relatively easy calculation of arbitrary fields, various geometrical regions (through which the integration can be carried out), and different step sizes. On the basis of the charge density method and Runge-Kutta method, we developed a computer program 'ELECTRA' (ELECTric field calculation and RAy tracing) which is discussed in chapter 3.

The program ELECTRA could estimate precisely the higher order aberration caused by a fringing field of electrostatic analyzer; this is discussed in chapter 4. ELECTRA is also applied to calculate the fringing field of quadrupole lenses and the effect of the boundary shape of a sector magnet.

The combination of the ray tracing method and the simplex method was discussed in chapter 5 where two examples are presented. One is a design of a magnet for an NMR spectrometer where the homogeneity of the magnetic field is optimize. Another example is a retardation lens system for a hybrid mass spectrometer.

REFERENCES

[1.1] M. Barber, R.S. Bordoli, R.D. Sedgwick and A.N. Tyler, Chem. Commun., 1981 (1981) 325.

[1.2] F.W. MacLafferty, Ed., Tandem Mass Spectrometry, John Wiley and Sons, New York, 1983.

[1.3] J.S. Cottrell and S. Evans, Anal. Chem., 59 (1987) 1990.

[1.4] J.A. Hill, S.A. Martin, J.E. Biller and K. Biemann, Biomed. Environ. Mass Spectrom., 17 (1988) 147.

[1.5] T. Kohno and T. Takuma, Numerical Calculation Method of Electric Field, Corona, Tokyo, 1980 (in Japanese).

2. DESIGN AND CONSTRUCTION OF A HIGH PERFORMANCE MASS SPECTROMETER

2.1 INTRODUCTION

Before the invention of the fast atom bombardment (FAB) ionization-technique, a mass spectrometer having "high transmission" and "high resolving power" was recognized to be a "high-performance mass spectrometer". The mass spectrometer constructed at Osaka university [2.1.1] was a typical example. This instrument consisted of a cylindrical electrostatic analyzer, an electrostatic quadrupole lens and a homogeneous sector magnet designed by Matsuda [2.1.2]. The second- and third- order aberrations of the system were calculated to be very small and this was examined experimentally [2.1.1]. The measured aberration coefficients were in good agreement with the calculated values. The instrument was mainly used for measuring organic compounds of less than three thousand daltons by the field desorption (FD) ionization techniques [2.1.3]. The development of FAB made it possible to ionize organic compounds having much larger molecular weight than before and therefore "high mass range" became the third key point of a high performance mass spectrometer. There is a relationship as

$$M/z = B^2 r_m^2/2V_a \qquad (2.1.1)$$

where M is the mass of the ion, z is the charge of the ion, B is the magnetic field strength, r_m the radius of the magnetic sector, and V_a is accelerating potential. Equation (2.1.1) defines the upper limit of detectable mass under the given r_m and the maximum field strength B_{max}. It can be seen that to increase the detectable mass, either B_{max} or r_m must be increased, or V_a must be decreased. The magnetic field strength is limited because of the saturation of magnet material. To decrease V_a is not favorable because ion extraction efficiency also decreases. Hence we have to increase r_m. Though it is possible to increase r_m by scaling up a conventional instrument, such an instrument, however, will require a very big and heavy magnet and large floor space. To overcome this problem, an ion optical system that can increase r_m while keeping the magnet in reasonable size by decreasing the deflection angle is preferable. In this chapter we discuss (1) the design and performance of a new mass spectrometer having large magnet radius, (2) the design and performance of a tandem mass spectrometer with quadrupole triplet interface and (3) a "zooming" function of a mass spectrometer.

Since an automatic search program was indispensable to determine the best values of ion optical parameters, a computer program "MSPLEX" using the simplex method was developed and is described in section 2.2.

Transfer matrix method

The coordinate system (x,y,z) is defined with its origin on the optical axis, with the z direction along the optical axis as shown in Fig.2.1.1. In principle, ion trajectories in

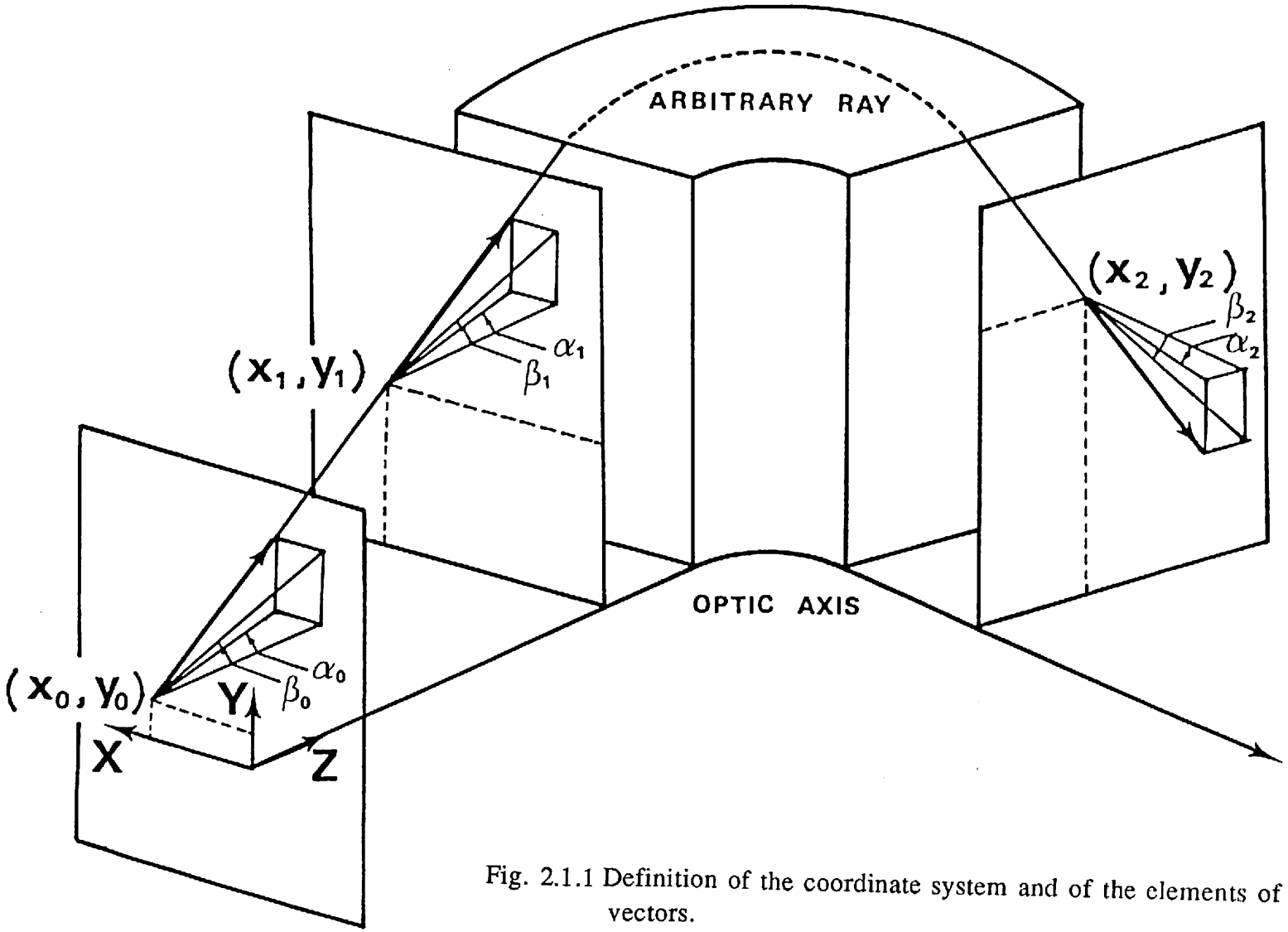

Fig. 2.1.1 Definition of the coordinate system and of the elements of ion optical position vectors.

an electric or magnetic field can be calculated by solving the equations of motion and can be specified in terms of an ion optical position vector $\mathbf{P}(x, \alpha, y, \beta, \gamma, \delta)$ where x and y are the coordinates of an ion, α and β are the horizontal and vertical inclination angles, γ and δ are relative mass and energy deviations, respectively. The ion optical position vector **P** for any arbitrary position is a function of the initial vector $\mathbf{P}_0(x_0, \alpha_0, \beta_0, \gamma, \delta)$. The relationship between **P** and $\mathbf{P}_0$ can be expressed by the transfer matrix [2.1.4][2.1.5]. The first-order relationship is in the horizontal direction

$$\begin{bmatrix} x \\ \alpha \\ \gamma \\ \delta \end{bmatrix} = \begin{bmatrix} (x|x) & (x|\alpha) & (x|\gamma) & (x|\delta) \\ (\alpha|x) & (\alpha|\alpha) & (\alpha|\gamma) & (\alpha|\delta) \\ 0 & 0 & 1 & 0 \\ 0 & 0 & 0 & 1 \end{bmatrix} \begin{bmatrix} x_0 \\ \alpha_0 \\ \gamma \\ \delta \end{bmatrix} \qquad (2.1.1a)$$

and in the vertical direction

$$\begin{bmatrix} y \\ \beta \end{bmatrix} = \begin{bmatrix} (y|y) & (y|\beta) \\ (\beta|y) & (\beta|\beta) \end{bmatrix} \begin{bmatrix} y_0 \\ \beta_0 \end{bmatrix} \qquad (2.1.1b)$$

The transfer matrix coefficients $(x|x),(x|\alpha),...$ can be obtained by, for example, the program TRIO [2.1.5].

The total transfer matrix of a complete mass spectrometer system can be simply calculated as the products of the transfer matrices of the individual components. When the matrix elements of the first row of the total transfer matrix are written A_x, A_α,... in the x-direction and A_y, A_β,... in the y-direction, the position of an ion in the final profile plane(x,y) can be expressed as

$$x=A_x x_0+A_\alpha \alpha_0+A_\gamma \gamma+A_\delta \delta+A_{xx} x_0^2+A_{x\alpha} x_0 \alpha_0+.....$$

$$y=A_y y_0+A_\beta \beta_0+A_{yx} y_0 x_0+..... \qquad (2.1.2)$$

The theoretical mass resolution R of a spectrometer is given by

$$R = \frac{A_\gamma}{A_x s+d+\Delta} \qquad (2.1.3)$$

where s is the width of the source slit, d is the width of the collector slit A_x and A_γ are the overall image magnification and mass dispersion coefficient, respectively, and Δ is the total amount of image aberration. The most efficient detection is obtained in the case $d=A_x s+\Delta$. In this case the resolving power is given by

$$R = \frac{A_\gamma}{2(A_x s+\Delta)} \qquad (2.1.4)$$

If the aberration Δ is sufficiently small, the resolving power is proportional to A_y / A_x.

REFERENCES

[2.1.1] H. Matsuda, Nucl. Instr. Meth., 187 (1981) 127.

[2.1.2] H. Matsuda, Int. J. Mass Spectrom Ion Phys., 14 (1974) 219.

[2.1.3] H.D. Beckey, Principles of Field Ionization and Field Desorption Mass Spectrometry, Pergamon, Oxford, 1977.

[2.1.4] K.L. Brown, R. Belbeach and P. Bounin, Rev. Sci. Instrum., 35 (1964) 481.

[2.1.5] T. Matsuo, H. Matsuda, Y. Fujita and H. Wollnik, Mass Spectrosc., 24 (1976) 19.

2.2 "MSPLEX" OPTIMIZATION PROGRAM USING SIMPLEX METHOD

2.2.1 INTRODUCTION

For designing ion optical systems, we have to determine many ion optical parameters to fulfill requirements of a system. For most cases we have to repeat the ion optical calculations again and again in order to find the optimum parameters. This is very tedious and time consuming process. Therefore it is preferable and effective to do this job automatically by the help of a parameter search program. Many types of algorithm for parameter search have been proposed [2.2.1]. Among them, the simplex method has been widely used because of its flexibility and stability [2.2.2, 2.2.3].

The optimization program "TRIOFIT" developed by Matsuo was formerly used [2.2.2]. However, this program sometimes failed to search or sometimes showed "instability" because it contained too much complicated and sophisticated facilities. The simplex program in TRIOFIT might be written so that it could be applied to the general use. Here, a parameter search program named "MSPLEX" that is mainly suitable for the determination of ion optical parameters has been prepared.

2.2.2 DESCRIPTION OF SIMPLEX METHOD

The simplex method was developed by Nelder and Mead [2.2.4]. A brief description of the method is as follows. First a "simplex" with N+1 apexes is constructed in an N-dimensional variable space. For example a triangle is constructed in a two-dimensional variable space. Then the simplex approaches step by step to the minimum point by changing its shape and position (see Fig.2.2.1). When the simplex becomes sufficiently small, the search is finished. More detailed explanation of the simplex method is given in ref [2,2,5]

Boundary condition

The simplex method itself is only a procedure to approach a local minimum point. the ranges of the variables are unlimited. Actually, the variables have a finite range where they can vary. Therefore, a practical program have to introduce some algorithm that can limit the variables within the range. We assume that variables x_i (i=1 to N) have the following boundary conditions:

$$l_i \leq x_i \leq u_i \qquad (2.2.1)$$

where l_i and u_i are lower and upper limits, respectively. In MSPLEX the variable x_i is transferred to a new variable y_i as

$$x_i = l_i + (u_i - l_i) \sin^2(y_i) \qquad (2.2.2)$$

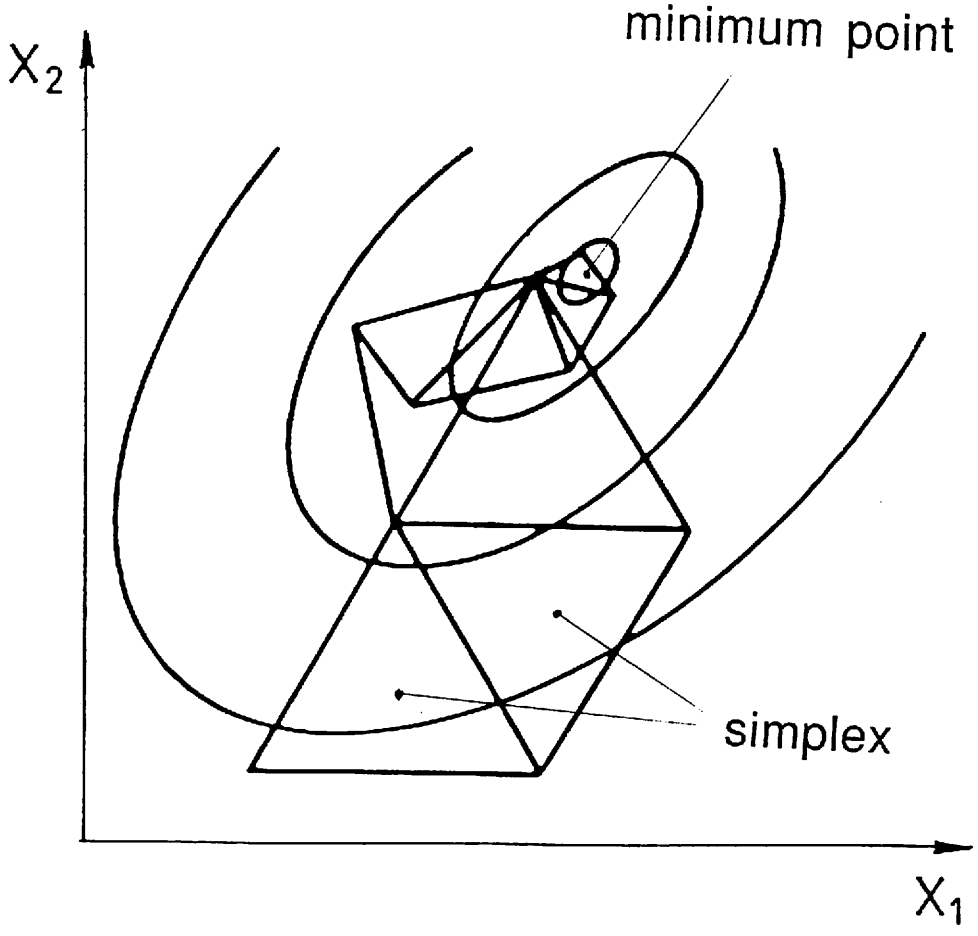

Fig. 2.2.1. Schematic drawing of simplex method.

The new variable y_i can vary $-\infty$ to $+\infty$, while the variable x_i does not exceed the ranges defined by Eqn.2.2.1. Therefore we can apply the simplex method using y_i without any boundary condition. This transformation does not create any new optimum point of the function to be minimized.

The stopping condition is also quite simple in MSPLEX; that is

$$\max\{ d_j, j=1,..,N+1\} \leq \varepsilon \qquad (2.2.3)$$

where ε is a small constant, d_j is the length between j-th apex and the apex where the function to be minimized has the smallest value in the simplex. If this condition is satisfied, the difference between the value of x_i of the apex having the smallest value and that of other apex is within $|u_i - l_i|\varepsilon$.

2.2.3 THE USE OF THE PROGRAM "MSPLEX"

The program "MSPLEX" is a set of subroutines written in FORTRAN77. The subroutines are described in this section.

1. SUBROUTINE INSET(L,U,X,NP)

This routine sets the ranges and the initial values of the variables.

input data

L(i): lower limit of i-th variable. (real)
U(i): upper limit of i-th variable. (real)
X(i): initial value of i-th variable. (real)
NP: number of variables. (integer)

2. SUBROUTINE MSPLEX(EPS, NMAX, NREP, IP)

This routine executes the simplex method.

input data

ESP: a small value used for ending the search (see Eqn.2.2.3).
NMAX: limit of search steps.
NREP: period of print out.
IP: parameter to control print out form.
If IP = -1; nothing is printed out.
= 0; print out information of initial and final simplex.
= 1; print out simple information of each period in addition to the case IP = 0.
= 2; print out full information for all period.

2.2. SUBROUTINE ANSWER(X)

This routine out put the variables of the minimum point of the final simplex.

output data

X(i): the value of i-th variable.

4. FUNCTION FUNC(X)

This is the function to be minimized. The name must be FUNC.
Figure 2.2.2 shows an example of a main program and a target function. The result of the example is also shown in Fig.2.2.2.

REFERENCES

[2.2.1] J. Kowalik and M.R. Osborne, Methodes For Unconstrained Optimization Programs, Elsevier, New York, 1968.
[2.2.2] T. Matsuo, Jpn. J. Appl. Phys., 23 (1984) 1581.
[2.2.3] H. Ikegami, Nucl. Instr. Meth., 187 (1981) 13.
[2.2.4] J. A. Nelder and R. Mead, Computer J., 7 (1965) 308.
[2.2.5] M.J. Box, D. Davies and W.H. Swann, Non-Linear Optimization Techniques, I. C. I., Edinburgh, 1969.

```
C*******************************************************
C
C          EXAMPLE OF MAIN ROUTINE FOR SIMPLEX METHOD
C
      REAL U(10), L(10), X(10)
C
C         DEFINE L, U, X
C
      L(1)=-0.0
      L(2)=-0.0
C
      U(1)= 10.0
      U(2)= 10.0
C
      X(1)= 3.0
      X(2)= 7.0
C
      NPARA=2
C
      CALL INSET(L,U,X,NPARA)
C
      CALL MSPLEX(0.001,100, 1,1)
C
      CALL ANSWER(X)
C
      WRITE(6,100) X(1), X(2)
  100 FORMAT(///'     RESULT OF SIMPLEX',
     &          ' X(1)=',F10.3,5X,' X(2)=',F10.3)
      STOP
      END
C*******************************************************
C
C          EXAMPLE OF FUNCTION FOR SIMPLEX METHOD
C
      FUNCTION FUNC(X)
      DIMENSION X(1)
C
      FUNC = (X(1) - 5.0)**2 + (X(2) - 5.0)**2
C
      RETURN
      END
```

Fig. 2.2.2. An example of a main program of MSPLEX.

```
X  1     3.0000        7.0000
X  2     4.5140        7.0000
X  3     3.0000        8.3182
F( 1)=   8.0000
F( 2)=   4.2362
F( 3)=   15.011
 N=       1    FI(IS)=  1.2459        ALENG=  .39270        NN= 2222
 N=       2    FI(IS)=  1.2459        ALENG=  .32383        NN= 1111
 N=       3    FI(IS)=  .86877        ALENG=  .27278        NN= 3333
 N=       4    FI(IS)=  .46560        ALENG=  .17841        NN= 3333
 N=       5    FI(IS)=  .34584        ALENG=  .11766        NN= 3333
 N=       6    FI(IS)=  .34584        ALENG=  .12885        NN= 1111
 N=       7    FI(IS)=  .12029        ALENG=  .92076E-01    NN= 3333
 N=       8    FI(IS)=  .10596        ALENG=  .81163E-01    NN= 3333
 N=       9    FI(IS)=  .38875E-01    ALENG=  .49381E-01    NN= 3333
 N=      10    FI(IS)=  .38875E-01    ALENG=  .38642E-01    NN= 3333
 N=      11    FI(IS)=  .33371E-01    ALENG=  .38642E-01    NN= 1111
 N=      12    FI(IS)=  .98561E-02    ALENG=  .21068E-01    NN= 3333
 N=      13    FI(IS)=  .94143E-02    ALENG=  .24665E-01    NN= 2222
 N=      14    FI(IS)=  .61335E-02    ALENG=  .15469E-01    NN= 3333
 N=      15    FI(IS)=  .91460E-03    ALENG=  .12590E-01    NN= 3333
 N=      16    FI(IS)=  .91460E-03    ALENG=  .77027E-02    NN= 3333
 N=      17    FI(IS)=  .91460E-03    ALENG=  .63761E-02    NN= 3333
 N=      18    FI(IS)=  .34764E-03    ALENG=  .40779E-02    NN= 3333
 N=      19    FI(IS)=  .12672E-03    ALENG=  .41187E-02    NN= 3333
 N=      20    FI(IS)=  .12672E-03    ALENG=  .21684E-02    NN= 3333
 N=      21    FI(IS)=  .12672E-03    ALENG=  .21684E-02    NN= 1111
 N=      22    FI(IS)=  .19628E-04    ALENG=  .15278E-02    NN= 3333
 N=      23    FI(IS)=  .15585E-04    ALENG=  .14144E-02    NN= 3333
 N=      24    FI(IS)=  .15585E-04    ALENG=  .71533E-03    NN= 3333
***** SEARCH END  NFLAG=  1 *****
 N=      24    FI(IS)=  .15585E-04    ALENG=  .71533E-03    NN= 3333
X  1     5.0035        5.0027
X  2     5.0030        4.9974
X  3     4.9961        4.9992
F( 1)=   .19628E-04
F( 2)=   .15585E-04
F( 3)=   .16215E-04


   result of simplex x(1)=      5.003       x(2)=      4.997
```

Fig. 2.2.3. Example of calculation result of MSPLEX.

2.3 ION OPTICAL SYSTEM OF A NEW DOUBLE FOCUSING MASS SPECTROMETER

2.3.1 PROCESS OF DETERMINATION OF FIELD PARAMETERS

A mass spectrometer has to be designed according to the following general procedure:

1) Specify the mass spectrometer's performance characteristics in terms of the first order coefficients A_x, A_α, A_γ, A_δ, A_y and A_β which are defined in Eqn. 2.1.2.
2) Define the instrument's geometry in terms of the first order parameters and the dimensions and positions of the electric and magnetic sectors and of the electrostatic quadrupole lens.
3) Specify and optimize the second order parameters so as to minimize the second order aberration coefficients.
4) Calculate the third order coefficients to estimate the third order aberrations.

First order parameters

A configuration consisting of a cylindrical electric sector, an electrostatic quadrupole lens and a homogeneous magnetic sector was considered. For simplicity of construction, the similar cylindrical electric sector and an electric quadrupole lens as Matsuda's design [2.3.1] were used. Then, the first order parameters to be determined were the field strength of the quadrupole lens(Q_k), the radius of the magnet(r_m), the deflection angle (w_m) of the magnet, and the entrance (ε') and the exit(ε'') angles of the magnet. Those parameters should be determined along the following guide line.

1) In order to increase the radius of the magnet (r_m) under the condition of keeping the magnet in reasonable size, the deflection angle (w_m) of the magnet must be decreased.
2) The lens action of a sector magnet decreases accordingly with the decrease of w_m and therefore the focusing length increases. In order to compensate this, the lens actions caused by large entrance (ε') and exit(ε'') angles of the magnet must be introduced.
3) The field strength of the quadrupole lens (Q_k) was determined so as to maximize ion beam transmission in the vertical direction through a magnet.

Various combinations of r_m and w_m were investigated. The set (r_m = 2.4, w_m= 40°) turned out to be the best combination from the view point of second order image aberrations.

Second order parameters

When a suitable set of the first-order parameters(r_m, w_m, ε', ε'',Q_k) was found, then second order aberrations must be minimized. The second-order parameters used here were the radius of curvature of the curved boundaries in the vertical direction at the

entrance(ρ_e') and the exit (ρ_e") of the electric sector, and those of the magnetic sector in the horizontal direction at the entrance (ρ_m') and at the exit(ρ_m"). The second-order parameters were optimized by the program MSPLEX. The function to be minimized was

$$FUNC(\rho_e',\rho_e'',\rho_m',\rho_m'') = w|A_{\alpha\alpha}|+|A_{\alpha\delta}|+|A_{\delta\delta}|+|A_{yy}|+|A_{y\beta}|+|A_{\beta\beta}| \quad (2.3.1)$$

where w is a weight factor. If the second-order aberrations cannot be satisfactorily reduced we have to repeat with other first-order parameters.

The new ion optical system

The first order parameters and aberration coefficients of the new ion optical system are shown in (A) of Table 2.3.1 and those of Matsuda's design in (B) for the comparison. The system B was originally designed so as to achieve complete second order focusing i.e. $A_{\alpha\alpha}=A_{\alpha\delta}=A_{\delta\delta}=A_{yy}=A_{y\beta}=A_{\beta\beta}\approx 0$. It should be noted that the second and third order aberration coefficients of a new system are nearly the same order, although the image aberrations tend to increase when the radius r_m increases. It was hardly possible to find such sets of parameters without the aid of MSPLEX.

In addition, the ratio A_γ / A_x ,which is proportional to mass resolution, is 1.76 for both systems. Therefore it is expected that both systems have the same resolving power under the same slit condition.

The radius of the magnetic sector of a new system is 2.4 times larger than that of Matsuda's; this means that the mass range becomes 5.76 times higher. The size of the magnetic sector (r_m w_m) of the new system increases only 30%. Consequently, the purpose of a new system which was to increase mass range without increasing the magnet size, is achieved. The ion optical block diagram is shown in Fig.2.3.1.

2.3.2 EXPERIMENTAL RESULTS AND DISCUSSION

An instrument, JMS-HX110 (JEOL Ltd. Tokyo), based on the new ion optical system discussed in the previous section was constructed and its performance was tested experimentally. The radius of the magnet was 72cm and the acceleration voltage was 10kV.

First, the mass resolution was measured. Figure 2.3.2 shows the mass spectrum of a doublet of m/Δm=54260 at m/z=84 (m/z= 83.953356 of $^{12}CH_2{}^{35}Cl_2$ and m/z= 83.951808 of $^{12}CD^{35}Cl_2$) produced by electron impact ionization(EI). The mass resolution of 150000(10% valley) was obtained under the source slit width of S=1.7μm and the collector slit width of d=0.9μm. This value was in good agreement with the calculated value of 155000.

Second, the mass range was examined by measuring the mass spectrum of the $(CsI)_nCs^+$ cluster ions using Xe-atom bombardment. Figure 2.3.3 shows the spectrum where clusters up to m/z=13902.8 were obtained at 10 kV acceleration. The spectrum of CsI cluster is often used to calibrate the instrument for wide mass range.

Third, we took mass spectra of heavy organic compounds by FAB to show its

applicability to biochemistry. A mass spectrum of bovine insulin (M.W.=5729.6 $C_{254}H_{377}O_{75}N_{65}S_6$) is shown in Fig.2.3.4. The peaks in the figure are the protonated-molecular ions $(M+H)^+$ which has distribution pattern owing to the effect of the natural occurring isotope of the elements, mainly the existence of ^{13}C. The theoretical mass distribution of the bovine insulin is shown in the upper part (a) of Fig.2.3.4 and the mass spectrum obtained by the mass spectrometer at Osaka University of Matsuda's design is shown in the middle diagram (b). The spectrum obtained by the new mass spectrometer is shown in the lower diagram (c). It is clearly seen that the mass resolution of the spectrum (c) has very much improved than that of (b) and that the spectrum pattern of (c) shows good agreement with the simulated peak (a).

It is very important and useful that we can obtain mass spectrum of such heavy organic compound such as insulin using a high mass range mass spectrometer with the help of soft ionization technique [2.3.2]. If the mass resolution is high enough to separate isotope peaks completely, we can determine not only chemical molecular weight but the physical molecular weight of each isotope. To determine the precise molecular weight of the compound is the first step of structural analysis of a unknown compound, since the molecular weight is one of the basic physical quantity to characterize the compound. The high resolution mass spectrum shown in Fig.2.3.4 gives key information for biological compounds.

REFERENCES

[2.3.1] H. Matsuda, Nucl. Instr. Meth., 187 (1981) 127.

[2.3.2] H.R. Morris, Ed., Soft Ionization Biochemical Mass Spectrometry, Heyden, London, 1981.

Table 2.3.1 First order parameters and aberration coefficients of (A) the new ion optical system and (B) Matsuda's [2.3.1]. The scale of the length is normalized to be r_m=1.0 and r_e=1.272 for the system B and r_m=2.4 and r_e=1.272 for A. The mass range of A is 5.76(=2.4^2) times larger than that of B. The meaning of overall transfer matrix elements A_{ij} is given in Eqn.2.1.2.

	A	B
r_e	1.272	1.272
w_e	85°	85°
r_m	2.4	1.0
w_m	40°	72.5°
ε'	-30°	-15°
ε''	-30°	0°
Q_k	-1.5	-1.91
A_x	0.531	0.440
A_γ	0.934	0.776
A_y	-3.00	-1.63
A_β	-2.00	-1.31
$A_{\alpha\alpha}$	0.00	0.02
$A_{\alpha\delta}$	0.00	-0.02
$A_{\delta\delta}$	0.23	0.01
A_{yy}	-0.19	-0.17
$A_{y\beta}$	0.15	0.21
$A_{\beta\beta}$	0.27	-0.02
$A_{\alpha\alpha\alpha}$	10.7	15.3
$A_{\alpha\alpha\delta}$	-9.2	-11.3
$A_{\alpha\delta\delta}$	12.7	16.5
$A_{\alpha yy}$	12.5	-1.2
$A_{\alpha y\beta}$	43.9	4.3
$A_{\alpha\beta\beta}$	77.6	8.6
$A_{\delta\delta\delta}$	-4.7	-5.7
$A_{\delta yy}$	4.3	0.7
$A_{\delta y\beta}$	16.2	-3.6
$A_{\delta\beta\beta}$	-35.5	-8.3
mass range (relative value)	5.76	1.0

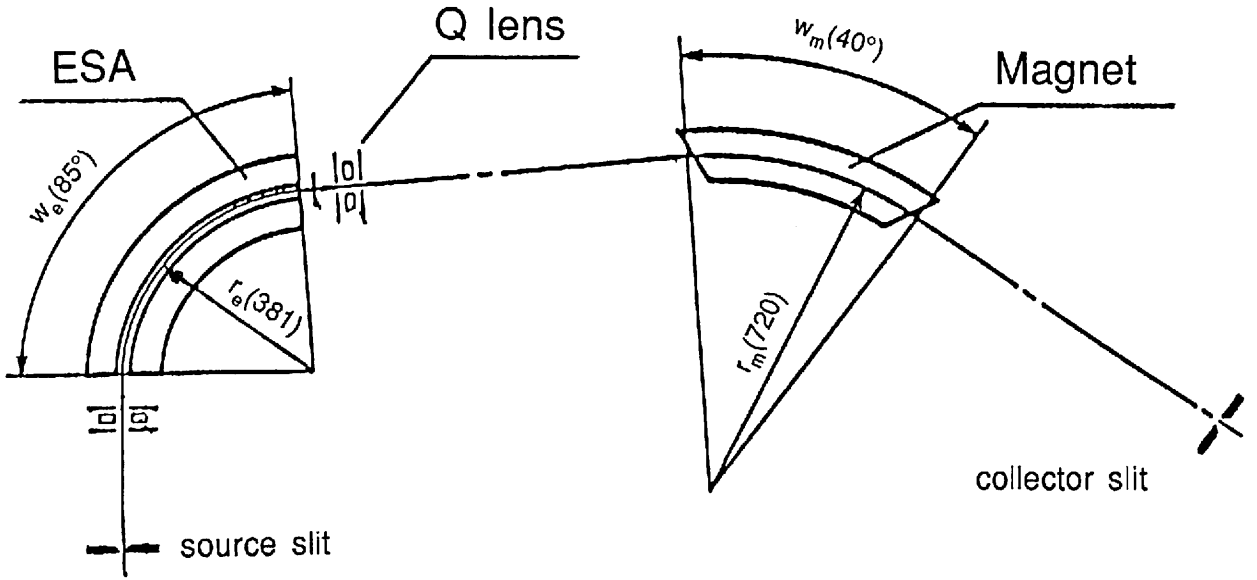

Fig. 2.3.1 Schematic drawing of the new ion optical system.

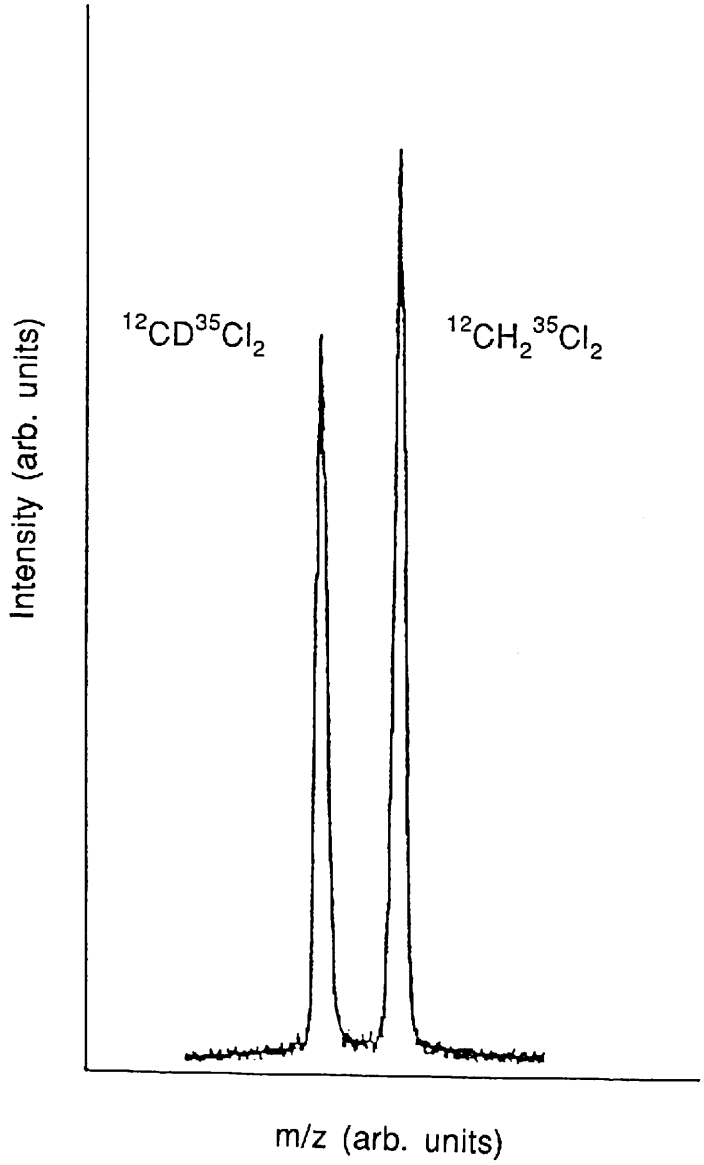

Fig. 2.3.2 Mass spectrum of $^{12}CH_2{}^{35}Cl_2$ and $^{12}CD^{35}Cl_2$ mass doublet at m/z 84 (m/Δm=54260). A mass resolution of 150000 (10% valley definition) is achieved. Whereas the theoretical mass resolution of 155000 is expected. This mean that higher order image aberrations are sufficiently small.

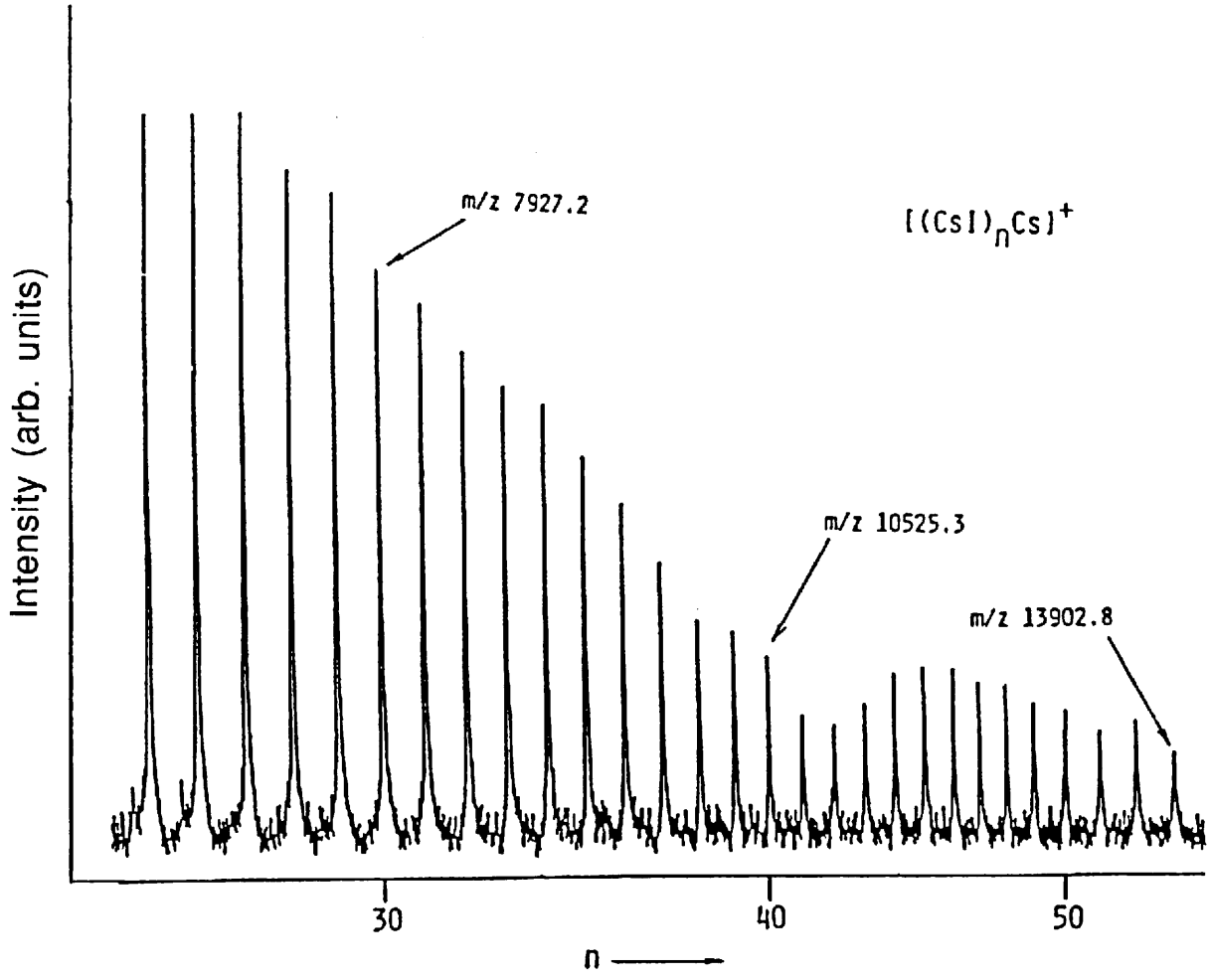

Fig. 2.3.3 Mass spectrum of CsI clusters.

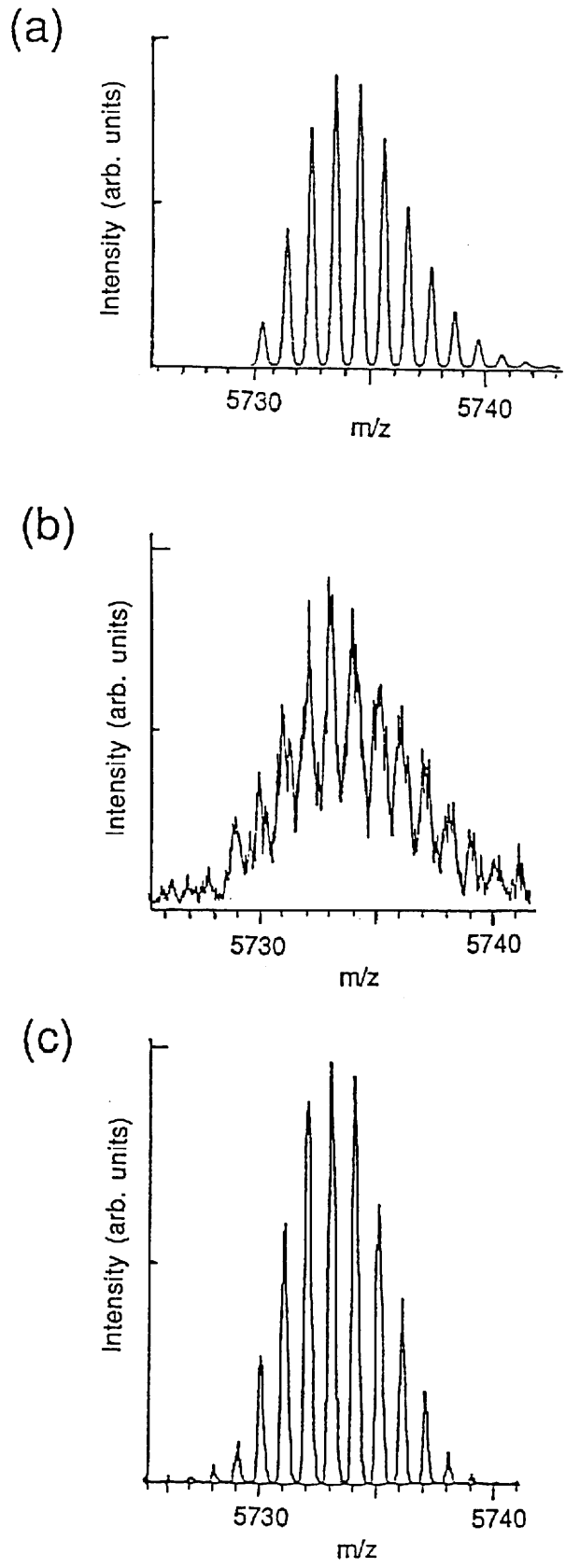

Fig. 2.3.4 Mass spectra of bovine insulin of the protonated molecular ion region.
(a) Simulated mass spectrum.
(b) Measured mass spectrum by the mass spectrometer at Osaka University.
Acceleration voltage: 3kV, source slit: 50μm
(c) Measured mass spectrum by the new mass spectrometer.
Acceleration voltage: 10kV, source slit: 26μm

2.4 ION OPTICAL SYSTEM OF A FOUR SECTOR MASS SPECTROMETER

2.4.1 INTRODUCTION

The recent development of high mass spectrometry have opened the wide application field in biochemistry. The first purpose was to determine the precise molecular weight of heavy biological compounds. We have succeeded in getting this information as discussed in the previous section. The second target was to develop the techniques of getting useful structural information such as amino acid sequence of a protein. For this purpose, we have designed and constructed a tandem mass spectrometer with high efficient interface. The design and its performances are discussed in this section.

2.4.2 Design and functions of a tandem mass spectrometer

We adopted the new double focusing mass spectrometer discussed in the previous section for MS1 and MS2, since high mass range is required. The next question is to employ how effective interface can be introduced between MS1 and MS2. The set of Einzel lens were formerly used, however its ion transmission was not satisfactory. We have newly introduced a quadrupole triplet lens (QT) as an interface. Ion optical block diagram of a tandem mass spectrometer is shown in Fig. 2.4.1. The geometrical parameters of each mass spectrometer are the same as shown in Fig. 2.3.1. The distance between the position of detector slit (C_1) and the position of source slit (S_2) was chosen arbitrary, say 0.36m. The focussing conditions were adjusted by tuning the field strength of three quadrupole lenses. The optimization program MSPLEX was effectively used for this purpose.

It should be noted that two types of operation mode are possible using a tandem mass spectrometer (four sector instrument), which are (1) conventional MS/MS mode and (2) newly introduced enhanced mass resolution mode.

MS/MS mode

In order to obtain high resolution mass spectrum of CID ions by MS2, the mass selected precursor ion beams have to be focused at a source slit of MS2. Such focusing condition could be realized using first two quadrupole lenses (Q1 and Q2). In order to define the function to be minimized, we introduce the following transfer matrices: the matrix [S2] is related to the region from the source slit of MS1 (S_1) to that of MS2 (S_2): [Eo] is related to the region from S_1 to the exit of the second electric sector: [D2] is the overall matrix (from S_1 to the collector slit of MS2). The potentials of two quadrupole lenses Q1 and Q2 are chosen as free parameters and that of Q3 is set to the ground potential. "The point to point focusing" in the horizontal direction from collector slit of MS1 (C_1) to the source slit of MS2 (S_2) is required for higher mass resolution. It is also required to compress and to make ion beams parallel in the vertical direction for the purpose of efficient transmission of daughter ions through MS2. Taking into account of above requirements, the function

to be minimized becomes

$$\text{FUNC}(Q1,Q2) = w\ |(x|\alpha)|_{S2} + |(y|y)|_{S2} + |(y|\beta)|_{S2} + |(y|y)|_{Eo} + |(y|\beta)|_{Eo} + |(y|y)|_{D2} + |(y|\beta)|_{D2} \quad (2.4.1)$$

where $(x|\alpha)_{S2}$,..., $(y|\beta)_{D2}$ are elements of matrices [S2],...,[D2] and w is a weight factor; here we use w = 100. The first term of Eqn. 2.4.1 is the requirement for the point to point focusing and other terms are for minimizing the divergence of the ion beam in the vertical direction. The calculated beam envelopes are shown in Fig. 2.3.2.

Enhanced mass resolution mode

We have noticed that a tandem mass spectrometer which consists of two electric and two magnetic sector can be used as a single four sector instrument. In this mode, better mass resolution can be expected without decreasing ion beam intensity, since mass dispersion can increase and image magnification can decrease. The free parameters are Q1,Q2,Q3. In this mode S_2 is removed, however the apertures in this region are still narrow. "The point to parallel focusing" in the horizontal direction is, therefore, required in order to keep the beam size small in this region. In addition, the virtual image must be focused to S_2 so that the double focusing condition is satisfied at C_2. The function to be minimized becomes

$$\text{FUNC}(Q1,Q2,Q3) = w\ |(\alpha|\alpha)|_{S2} + |(y|y)|_{S2} + |(y|\beta)|_{S2} + |(y|y)|_{Eo} + |(y|\beta)|_{Eo} + |(y|y)|_{D2} + |(y|\beta)|_{D2} \quad (2.4.2)$$

The first term is the requirement for the point to parallel focusing and another terms are for minimizing the divergence of the ion beam in the vertical direction.

The beam envelopes are shown in Fig. 2.4.3 at suitable initial conditions.

2.4.3 EXPERIMENTAL

The two types of operation mode were examined experimentally. The measurements were carried out with a four-sector tandem mass spectrometer JEOL HX110–HX110 [2.4.3]. The ion optical block diagram is shown in Fig. 2.4.1. and its photograph is shown in Fig. 2.4.2. The acceleration voltage was 10kV. Mass spectra were recorded with a JEOL DA5000 data system. MS1 and MS2 were calibrated with an alkali iodide mixture (LiI, NaI, CsI). The samples { xenon and perfulorokerosene(PFK)} were introduced through an inlet system and ionized by electron impact (EI) ionization. The samples(melittin and hemoglobin Nishiyama) were ionized by FAB method. Xenon of 6 keV was used as the primary atom beam. Glycerol was used as a matrix.

MS/MS mode

The main purpose of MS/MS measurement is to give the structural information

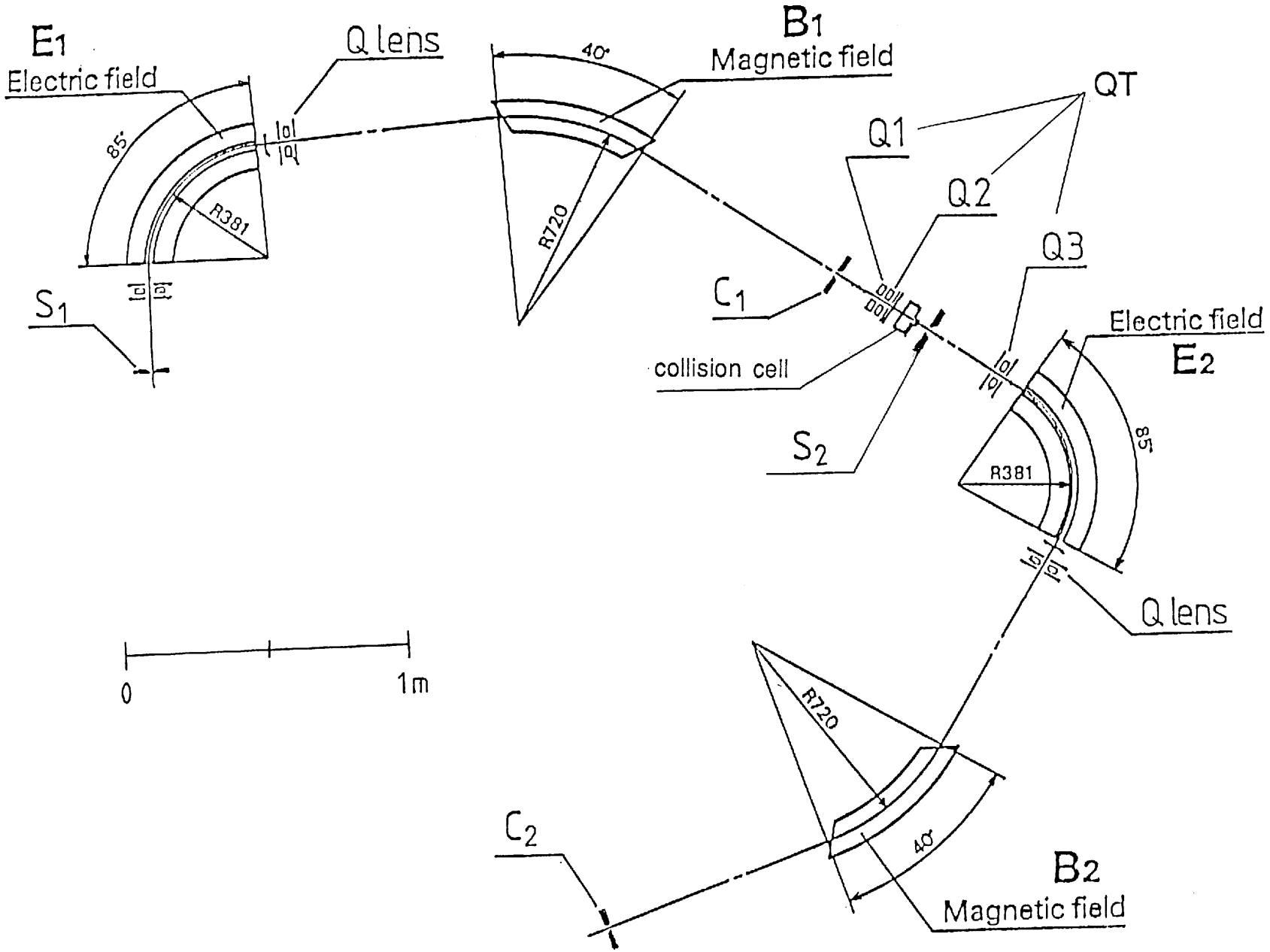

Fig. 2.4.1 Ion optics of the new tandem mass spectrometer with the quadruple triplet(QT) interface.

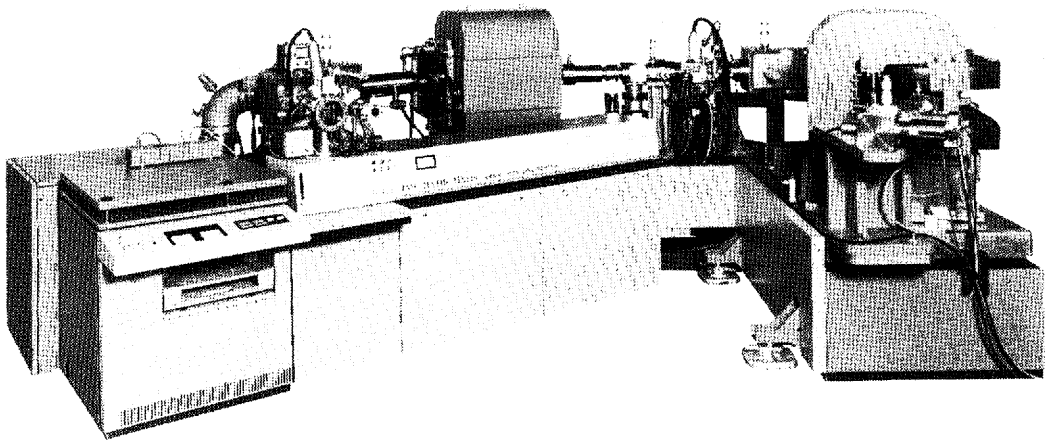

Fig. 2.4.2 Photograph of the new tandem mass spectrometer.

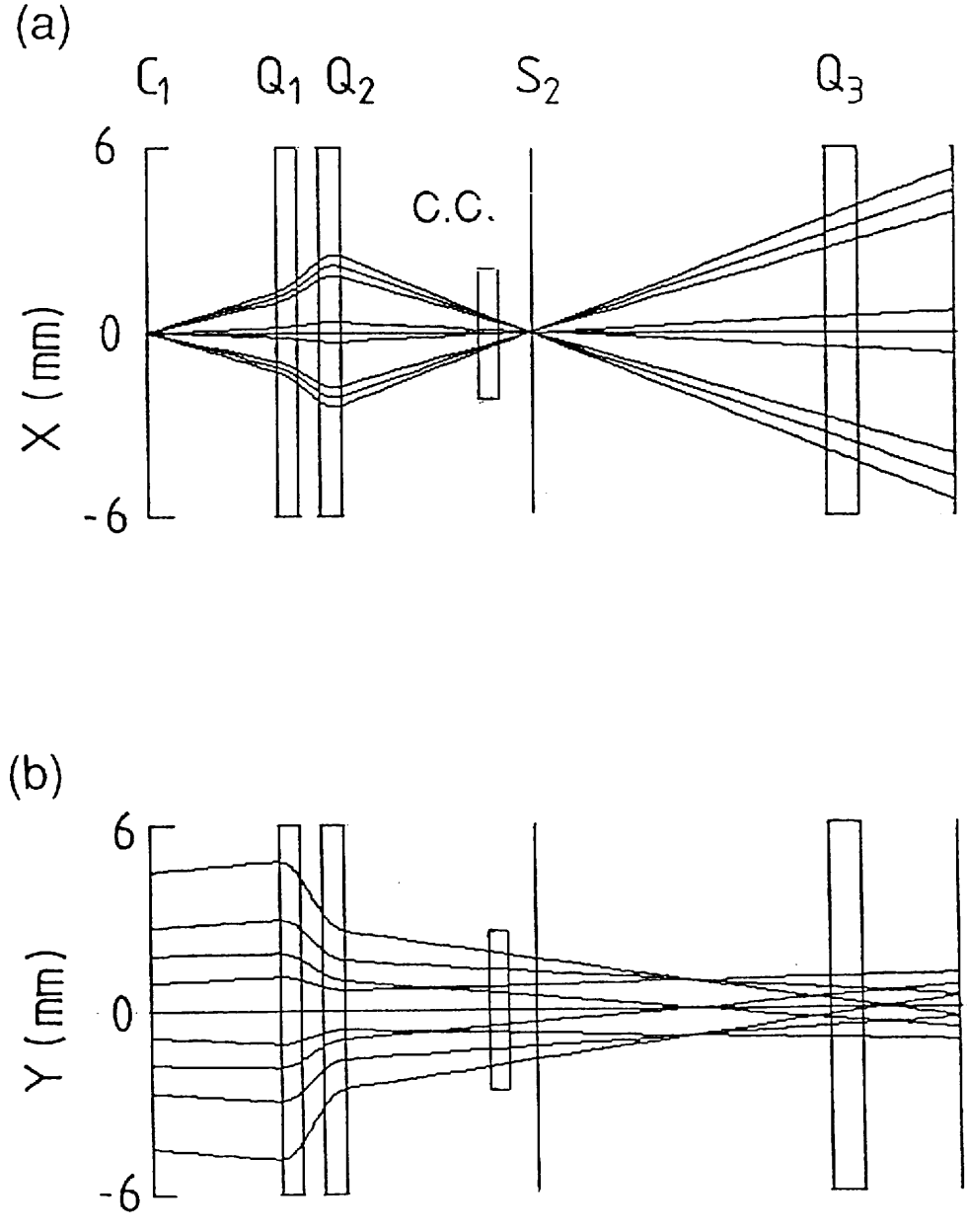

Fig. 2.4.3 Beam envelopes in the interface region in the MS/MS mode; (a) horizontal and (b) vertical envelopes, where C_1 and S_2 denote the collector slit of MS1 and source slit of MS2, respectively and C.C. denotes the collision cell. The beam is focused to S_2 in the horizontal(x) direction and the beam size in the vertical(y) direction is reduced by Q_1 and Q_2.

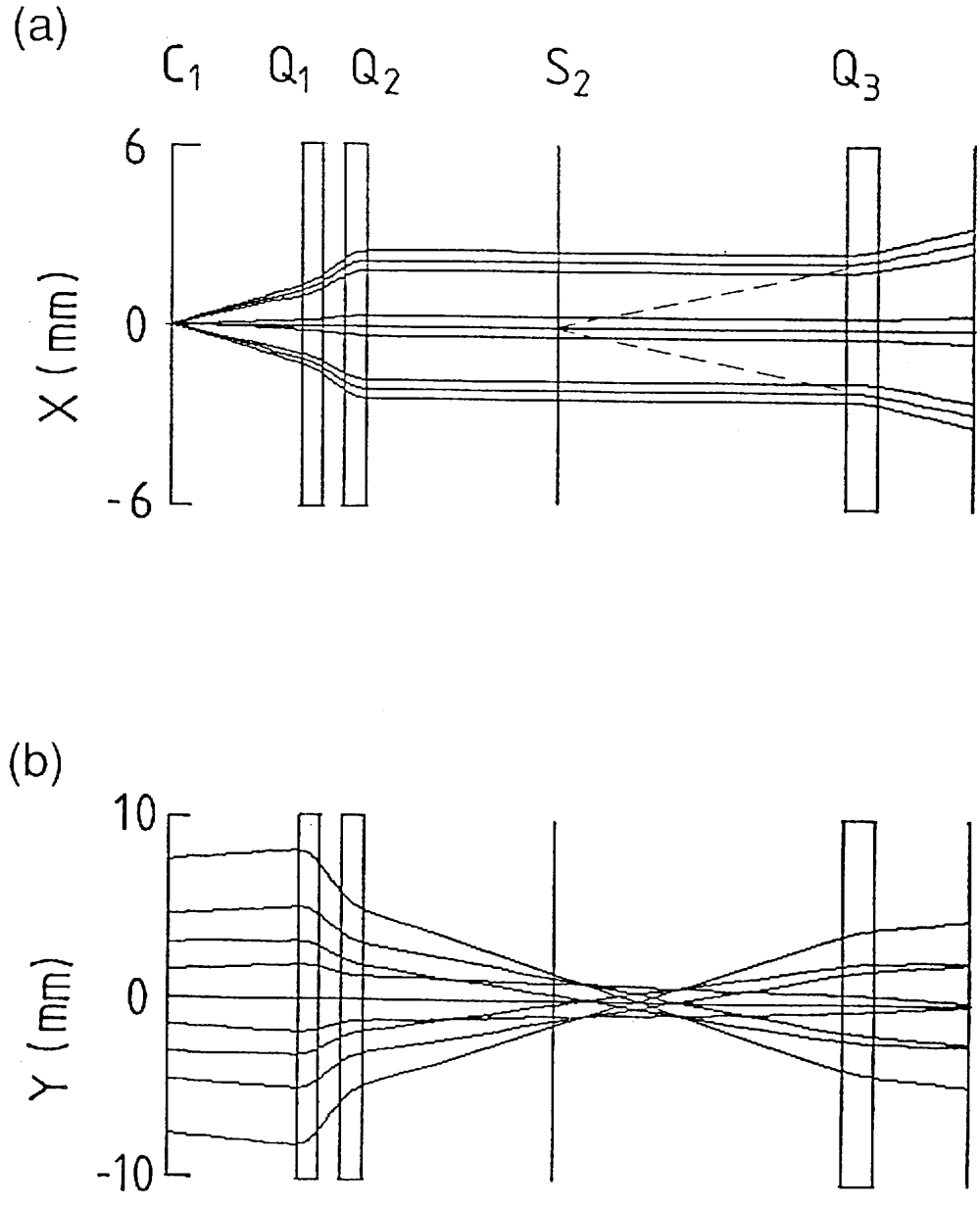

Fig. 2.4.4 Beam envelopes in the interface region in the enhanced resolution mode; (a) horizontal and (b) vertical envelopes, where C_1 and S_2 denote the collector slit of MS1 and source slit of MS2, respectively. The point to parallel focusing is achieved in the horizontal(x) direction and the virtual image is focused to S_2.

concerning a specific ion peak selected by MS1 from the mixture sample. We discuss the MS/MS capability by explaining the procedure of characterizing hemoglobin variant (Hb-Nishiyama).

Generally, a protein consists of a number of amino acids and its sequence is inherent. If one amino acid is mutated to the other, then its biological character is affected. This protein is called to be "variant" and causes the "molecular disease" in most cases. It is very important to elucidate the type and the position of amino acid mutation from the view point of clinical diagnosis. The hemoglobin β-chain consists of 142 amino acids and contains many same type of amino acids. In order to specify the position of the mutation, the whole hemoglobin variant has to be digested by trypsin into fourteen peptide fragments. The mass spectrum of the tryptic mixture is shown in Fig. 2.4.5. The peak with an arrow can be identified as a "variant" peak of m/z=1256.6 by comparing with the normal case; the mass of normal fragment should be m/z=1314.6. The decrease of 58.0 u suggested one of the substitutions: (A) 21Asp →Gly, (B) 22Glu→Ala, or (C) 26Glu→Ala. In order to determine the decisive sequence of the variant, collision-induced decomposition (CID) technique was used. Mainly nine type of fragment ions are usually produced from protonated peptide by CID as shown in Fig.2.4.6. Calculated masses of six type fragment ions (a_n, b_n, c_n, x_n, y_n, z_n) for the normal and these three candidate sequences are predicted in Fig. 2.4.7. The fragment ions formed in a collision cell were analyzed by MS2 using a linked scan operation [2.4.4]. The MS/MS spectrum from the variant peak is shown in Fig. 2.4.8. We assigned the obtained CID peaks with respect to the three candidate sequences given in Fig.2.4.7 and could determine the real sequence of Hb-Nishiyama to be the sequence (B) 22Glu→Ala. The process of the elucidation is explained in the figure captions of Fig.2.4.8.

As shown in this case, the MS/MS technique can do its task quite easily in the structural analysis of variants. A detailed discussion of characterizing protein valiant by MS/MS technique was given, for example, ref. 2.4.5.

Enhanced resolution mode [2.4.6]

The detector slit of MS1 was removed for creation an aperture about 8 mm wide and the source slit of MS2 was also removed. The procedure of measurement was as follows. (1) the ion beam under study was detected using the variable slit (set to 90 μm) of MS1. (2) the magnet of MS2 was scanned to sweep the ion beam across the MS2 detector slit (70 μm) and the resulting mass spectrum was recorded and stored in the data system. Under these conditions, the detectable mass range through MS1 and MS2 with the fixed magnetic field of MS1 was approximately 1.4%. Ion beam transmission through MS2 was measured by comparing the relative ion current of $(CsI)_{11}Cs^+$ ions at the detector of MS1 and MS2, respectively and found to be 1 : 0.9, i.e. 90% transmission from MS1 through MS2.

First, a doublet of Δm=0.087 u at m/z 131 (m/z 130.905 of Xe and m/z 130.992 of PFK generated by EI) was measured by MS1 alone shown (Fig. 2.4.9a) and then by the combination of (MS1 + MS2) (Fig. 2.4.9b). Both scan range and scan speed were kept identical to produce comparable peak shape and mass dispersion. The mass resolution

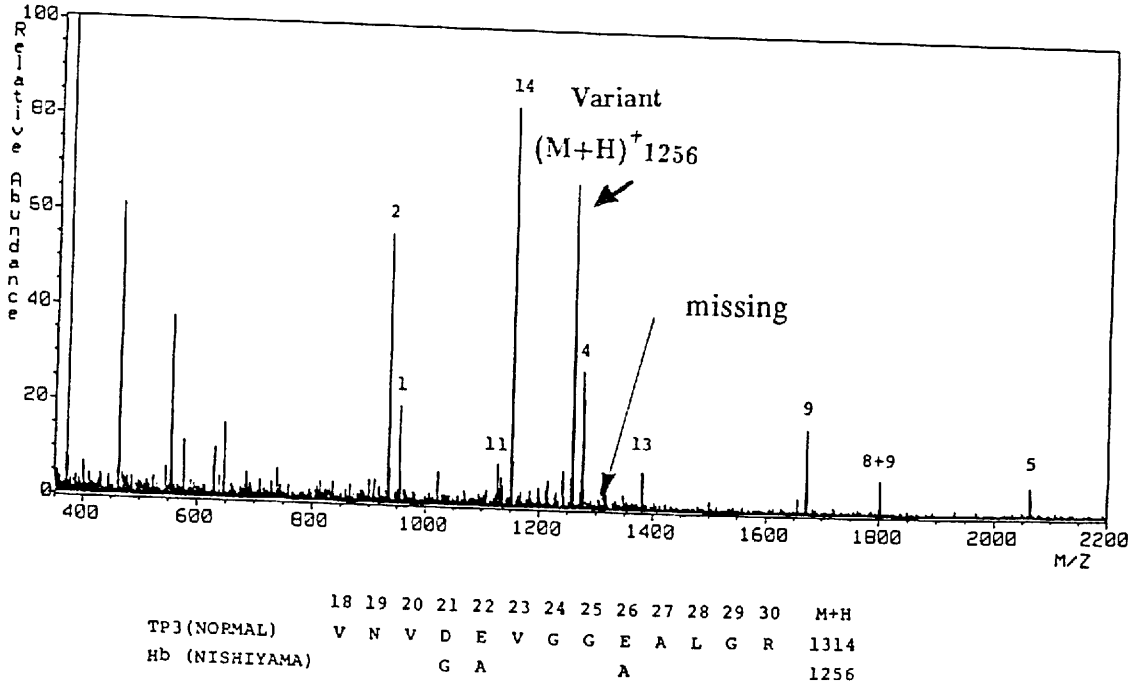

	18	19	20	21	22	23	24	25	26	27	28	29	30	M+H
TP3(NORMAL)	V	N	V	D	E	V	G	G	E	A	L	G	R	1314
Hb (NISHIYAMA)				G	A				A					1256

Fig. 2.4.5. Normal mass spectrum of tryptic Hb-β variant Nishiyama.

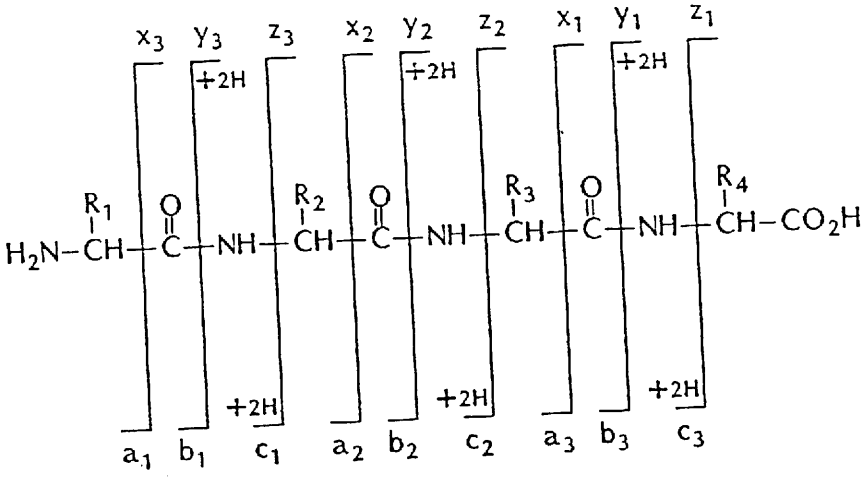

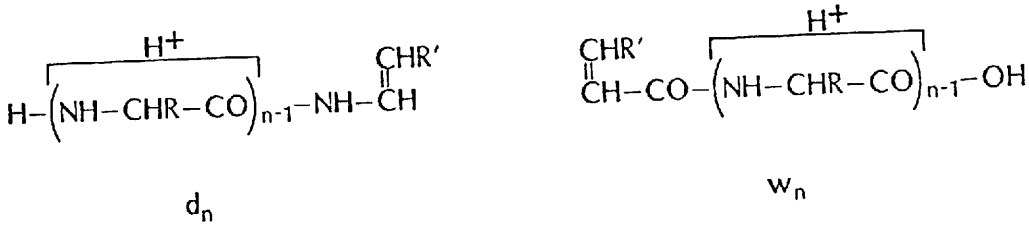

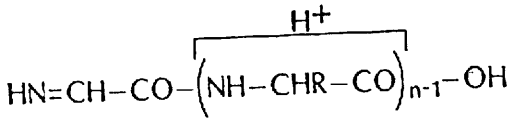

Fig. 2.4.6 Notation of fragment ions.

A. 21Asp → Gly

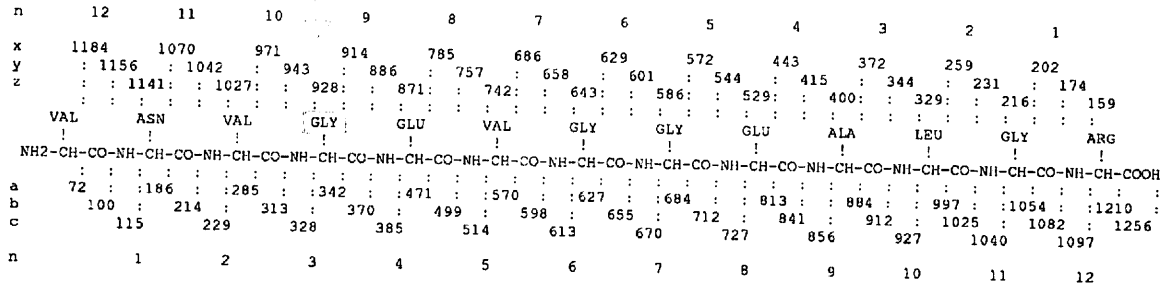

B. 22Glu → Ala

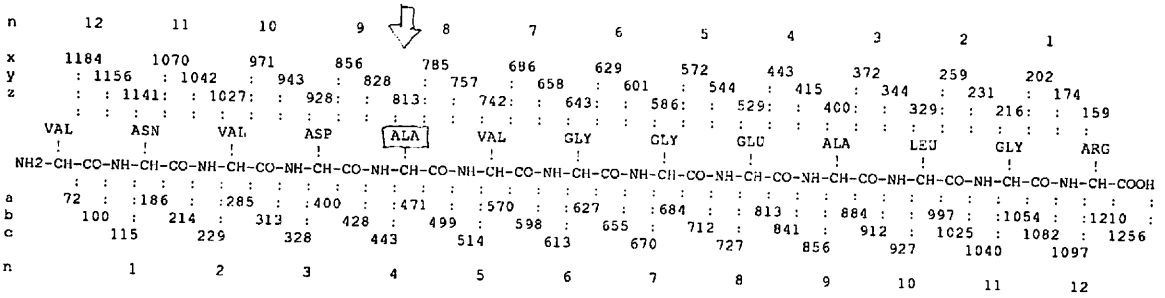

C. 26Glu → Ala

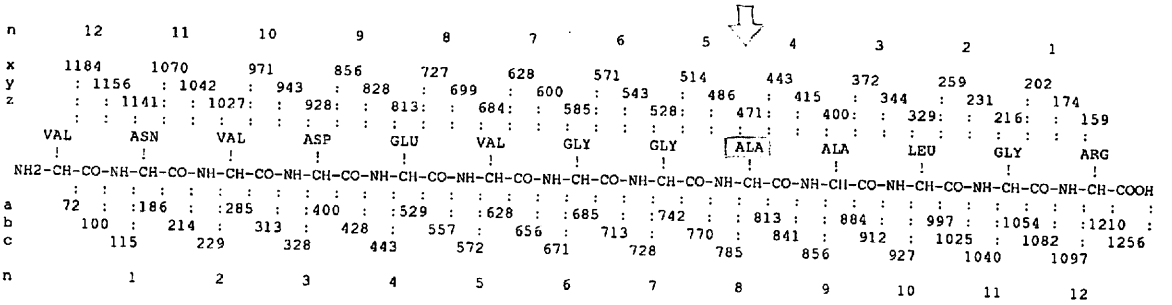

D. Normal

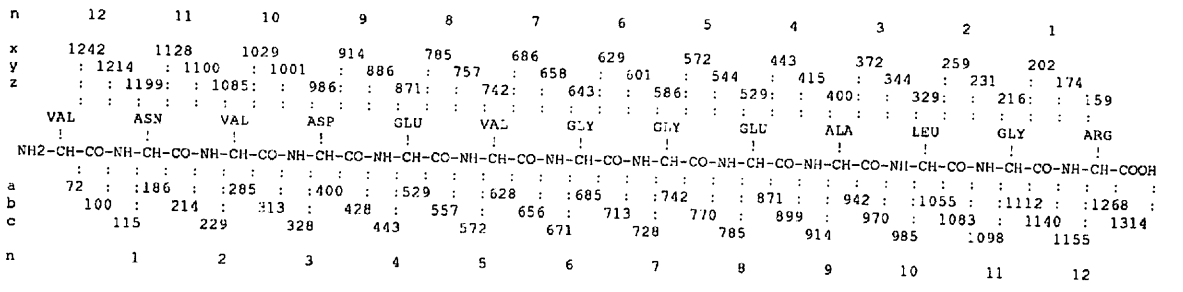

Fig. 2.4.7 Calculated masses of six type fragment ions.

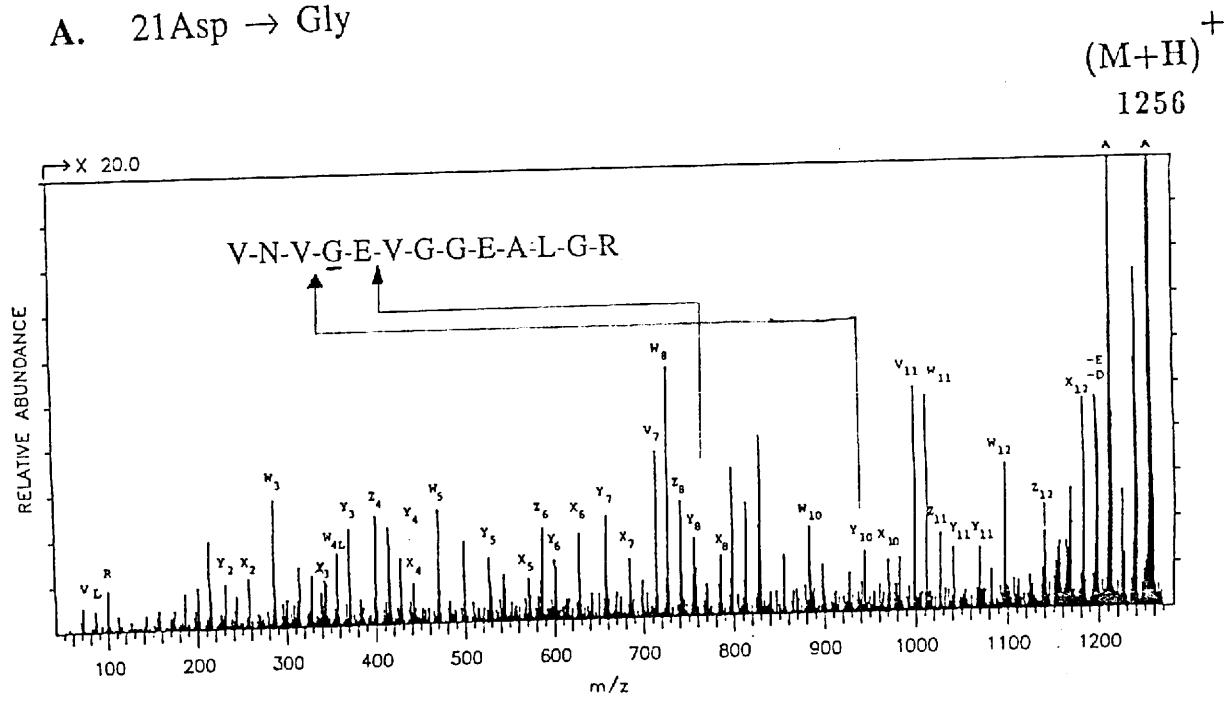

Fig. 2.4.8.a. MS/MS spectrum from variant peak of HB-β Nishiyama. The peaks are assigned according to the candidate sequence **A** in Fig.2.4.7 (21Asp → Gly). The peaks x_9, y_9, z_9 cannot be assigned in this case. This means that the part (-G-E-) of the candidate sequence indicated in the figure is not correct.

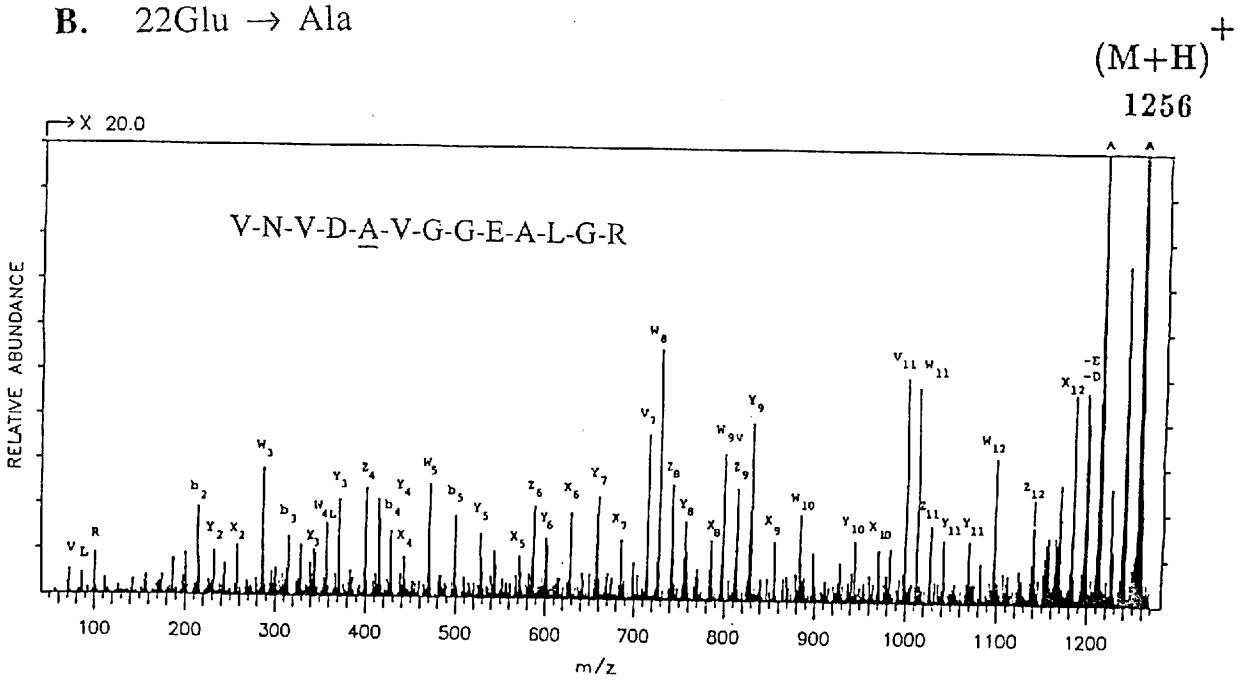

Fig. 2.4.8.b. MS/MS spectrum from variant peak of HB-β Nishiyama. The peaks are assigned according to the candidate sequence **B** in Fig.2.4.7 (22Glu → Ala). Almost all x_n, y_n, z_n peaks can be assigned. This means that this candidate sequence is correct.

C. 26Glu → Ala

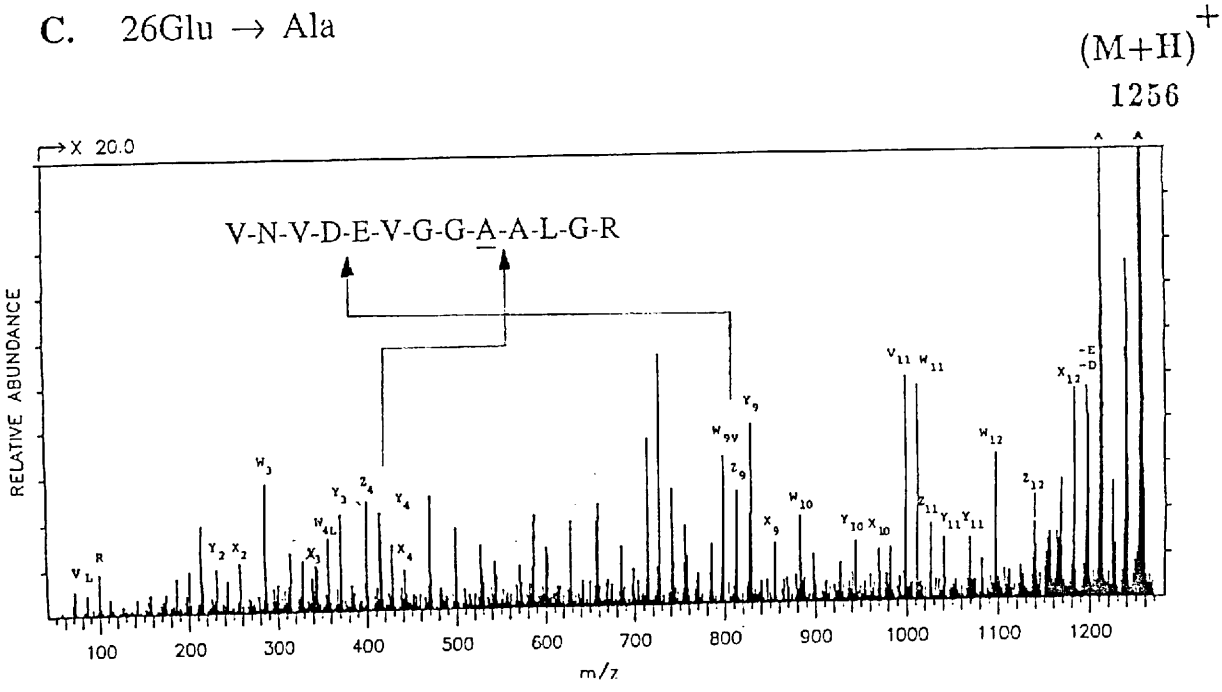

Fig. 2.4.8.c. MS/MS spectrum from variant peak of HB-β Nishiyama. The peaks are assigned according to the candidate sequence C in Fig.2.4.7 (26Glu → Ala). The peaks x_n, y_n, z_n (n=5 to 8) cannot be assigned. This means that the part (-E-V-G-G-A-) of the candidate sequence indicated in the figure is not correct.

predicted by theoretical calculations and that found experimentally are compared in Table 2.4.1. The improvement factor of image magnification, mass dispersion and mass resolution between MS1 and (MS1+MS2) is shown in Table 2.4.2. Both theoretical and experimental values agree quite well, confirming the ion optical considerations put forward in the preceding theoretical discussion.

Second, the protonated molecular ion $(M+H)^+$ region of the FAB spectrum of melittin was recorded by MS1 and (MS1 + MS2), respectively. The results are shown in Fig. 2.4.10a and FIg. 2.4.10b. These mass spectra were taken with the same sample amount and source slit width (giving the same ion current measured with the variable detector slit of MS1). Mass resolution is clearly improved, while a transmission efficiency of 90% is obtained as demonstrated by the CsI measurement. Thus a four sector mass spectrometer operated in this enhanced resolution mode results in more than two times higher mass resolution while retaining almost the same beam intensity. Although the same improved resolution could be obtained by narrowing the slits of a single double-focusing mass spectrometer, it would be at the expense of a proportionally reduced sensitivity.

The enhanced resolution mode is useful to detect the molecular ion cluster in high mass resolution using a simultaneous detector (an array detector). This was demonstrated by Biemann's group experimentally [2.4.7], where the molecular cluster of glucagon (m/z 3481.6) was detected with a mass resolution of 5500.

2.4.4 CONCLUSION

A tandem mass spectrometer consisting of four sectors has the following three functions: (1) single MS mode by using either MS1 or MS2, (2) MS/MS mode, and (3) enhanced mass resolution mode by using (MS1+MS2). We demonstrated these three functions experimentally. The ion optical performance agreed well with the calculated expectations. The key feature is the proper beam transmission through the quadrupole triplet located between MS1 and MS2. The function and the usefulness of a tandem mass spectrometry in biological compound such as "variant protein" could be demonstrated by experiments. Many scientists have been using this type of mass spectrometer in various field of biochemistry.

REFERENCES

[2.4.1] F.W. McLafferty, Ed., Tandem Mass Spectrometry, John Wiley and Sons, New York, 1983.

[2.4.2] K. Biemann, Biomed. Environ. Mass Spectrom., 16 (1988) 99.

[2.4.3] Y. Kammei, Y. Itagaki, E. Kubota, F. Kunihiro and M. Ishihara, 33rd Annual Conference on Mass Spectrometry and Allied Topics, ASMS, San Diego, CA, 1985, p.855.

[2.4.4] K. Sato, T. Asada, M. Ishihara, F. Kunihiro, Y. Kammei, E. Kubota, C.E. Costello, S.A. Martin, H.A. Scoble and K. Biemann, Anal. Chem., 59 (1987) 1652.

[2.4.5] Y. Wada, T. Matsuo and T. Sakurai, Mass Spectrom. Rev., 8 (1989) 379.
[2.4.6] T. Matsuo, M. Ishihara, S.A. Martin and K. Biemann, Int. J. Mass Spectrom. Ion Processes, 86 (1988) 83.
[2.4.7] J.A. Hill, S.A. Martin, J.E. Biller and K. Biemann, Biomed. Environ. Mass Spectrom., 17 (1988) 147.

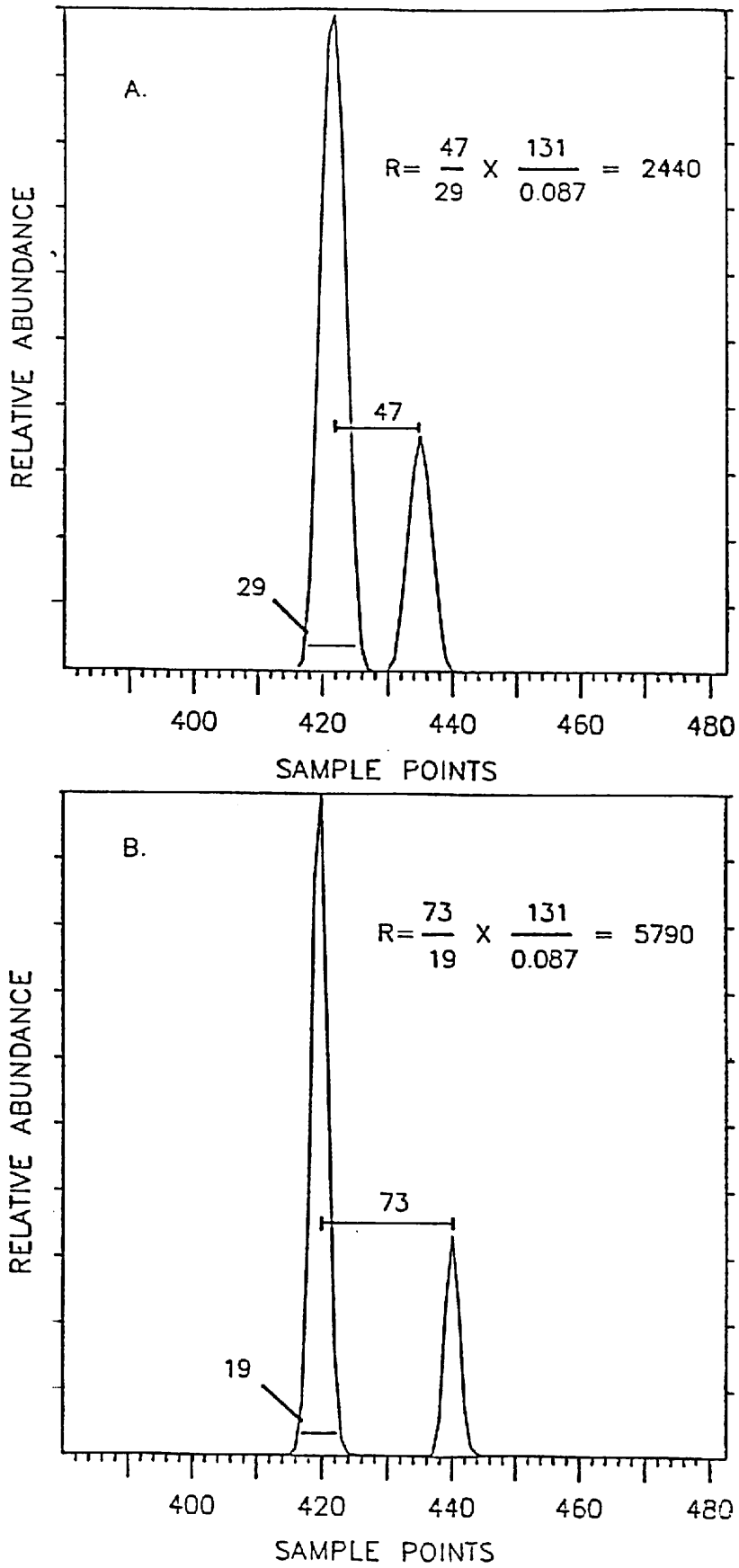

Fig. 2.4.9. Electron impact (EI) mass spectra of xenon and PFK mass doublet at m/z 131(Δm=0.087u);(a) MS1 only; (b) (MS1+MS2). The numerical values represent the peak width at 5% peak height and distance from center in mm on the original recording before reduction of the figure.

Table 2.4.1 Comparison of magnification, mass dispersion and mass resolution of MS1 only and the enhanced reaolution mode (MS1+MS2)

	Mass resolution (MS-1)	Mass resolution (MS-1 + MS-2)
Theoretical	$\frac{0.28}{2(0.53\ x_0)} = 2600$	$\frac{0.47}{2(0.36\ x_0)} = 6500$
Experimental	2440	5790

Table 2.4.2 Comparison of theoretical and expreimental mass resolution

	Magnification	Mass dispersion	Mass resolution
Theoretical	$\frac{0.36}{0.53} = 0.68$	$\frac{0.47}{0.28} = 1.68$	$\frac{0.47/0.36}{0.28/0.53} = 2.49$
Experimental	$\frac{19}{29} = 0.66$	$\frac{73}{47} = 1.55$	$\frac{73/19}{47/29} = 2.37$

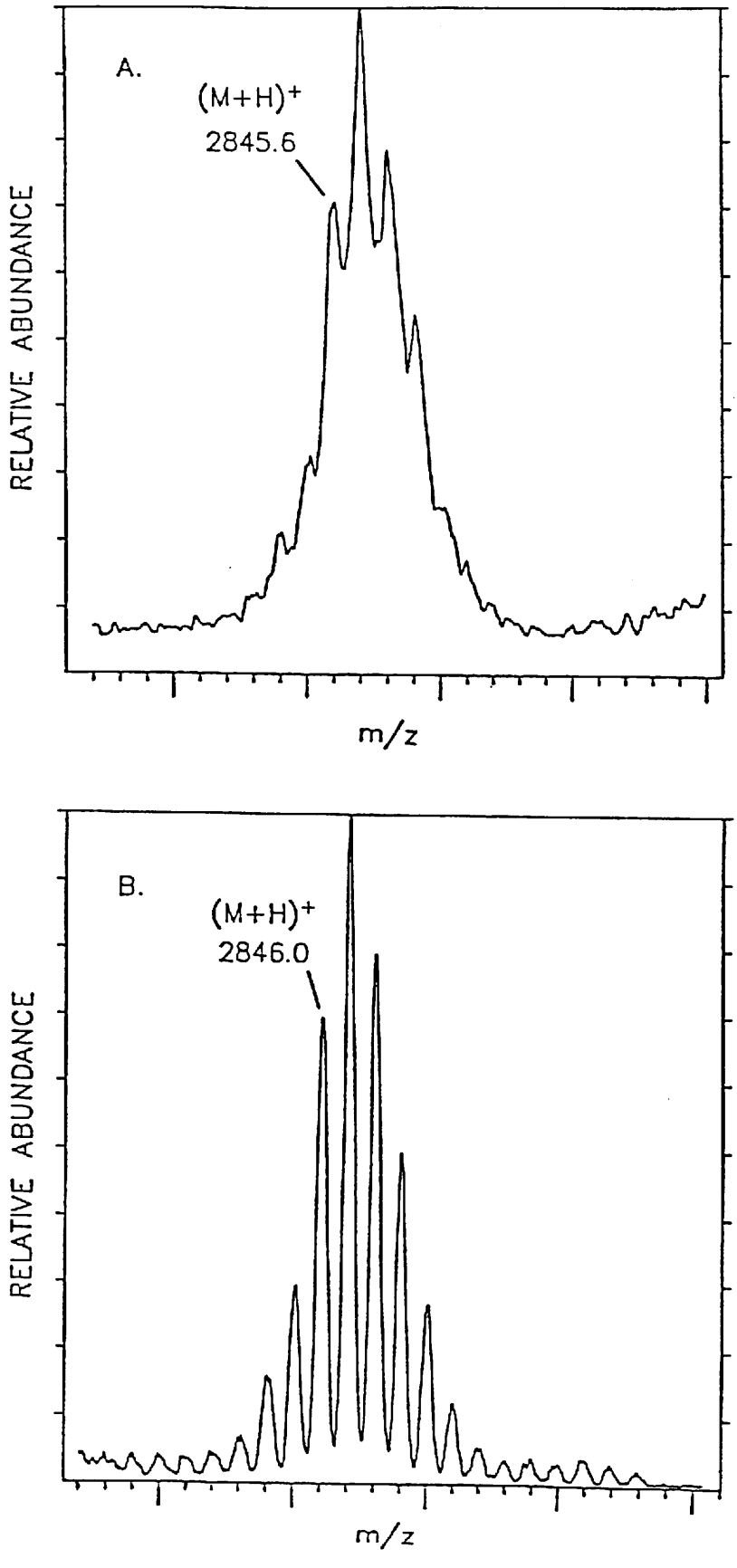

Fig. 2.4.10. The protonated molecular ion $(M+H)^+$ region of the FAB mass spectra of melittin. (a) MS1 only; (b) (MS1+MS2). Each represents a single scan.

2.5 ZOOMING FUNCTION OF A MASS SPECTROMETER USING QUADRUPOLE-OCTAPOLE-QUADRUPOLE ARRANGEMENT

2.5.1 INTRODUCTION

A simultaneous ion detector (an array detector) is very powerful apparatus to detect weak ion beams having different masses. It is necessary to vary mass dispersion of a mass spectrometer, since an array detector has the limited size and its space resolution is also limited. A method for varying the mass dispersion by using quadrupole lenses has been proposed by Tuithof and Boerboom [2.5.3]. They have constructed an instrument which consists of a magnetic quadrupole lens, a magnetic sector having a radius of 165mm and an electrostatic quadrupole lens. This single focusing instrument can vary the mass range 1 : 1.01 through 1 : 1.60 on a 20mm focal plane. Their method, however, is not suitable for a double focusing mass spectrometer, because additional quadrupole lenses placed before a magnetic sector strongly disturb the double focusing condition. We have, therefore, developed a new zooming system which is suitable for a double focusing mass spectrometer. Two electrostatic quadrupole lenses (a quadrupole doublet) and an electrostatic octapole lens are introduced after a magnetic sector. Ion optical study and experimental results of this new zooming apparatus are described in this section.

2.5.2 GEOMETRY

This system consists of the double focusing mass spectrometer (JEOL JMS-HX110) and three additional lenses. The geometry is shown in Fig.2.5.1. The point P_0 is the double focusing point of the original system where a point detector is placed. One of the features of the new system is that when all the electric potentials applied to the additional lenses are set to zero, we can operate the new system following as the original way; thus either a conventional point detector or array detector can be used.

An electrostatic quadrupole doublet (QD1,QD2) is introduced to vary the simultaneously detectable mass range on an array detector and an electrostatic octapole lens (O) is introduced to correct the curvature of the focal plane due to third order aberrations. An array detector is placed at the focusing point of the new system (P_1) with inclination angle θ_α which is the angle between the optic axis and the angle focal plane.

2.5.3 QUADRUPOLE DOUBLET

The transfer matrix method with MSPLEX was used for ion optical calculations. Three matrices are defined to investigate the function of the quadrupole doublet (see the lower part of Fig. 2.5.1): the matrix [A] is related to the total ion optical system (from the source slit to the point P_1); [B] is related to the region from the source slit to the exit of the magnetic sector; [C] is related to the region from the exit of the magnetic

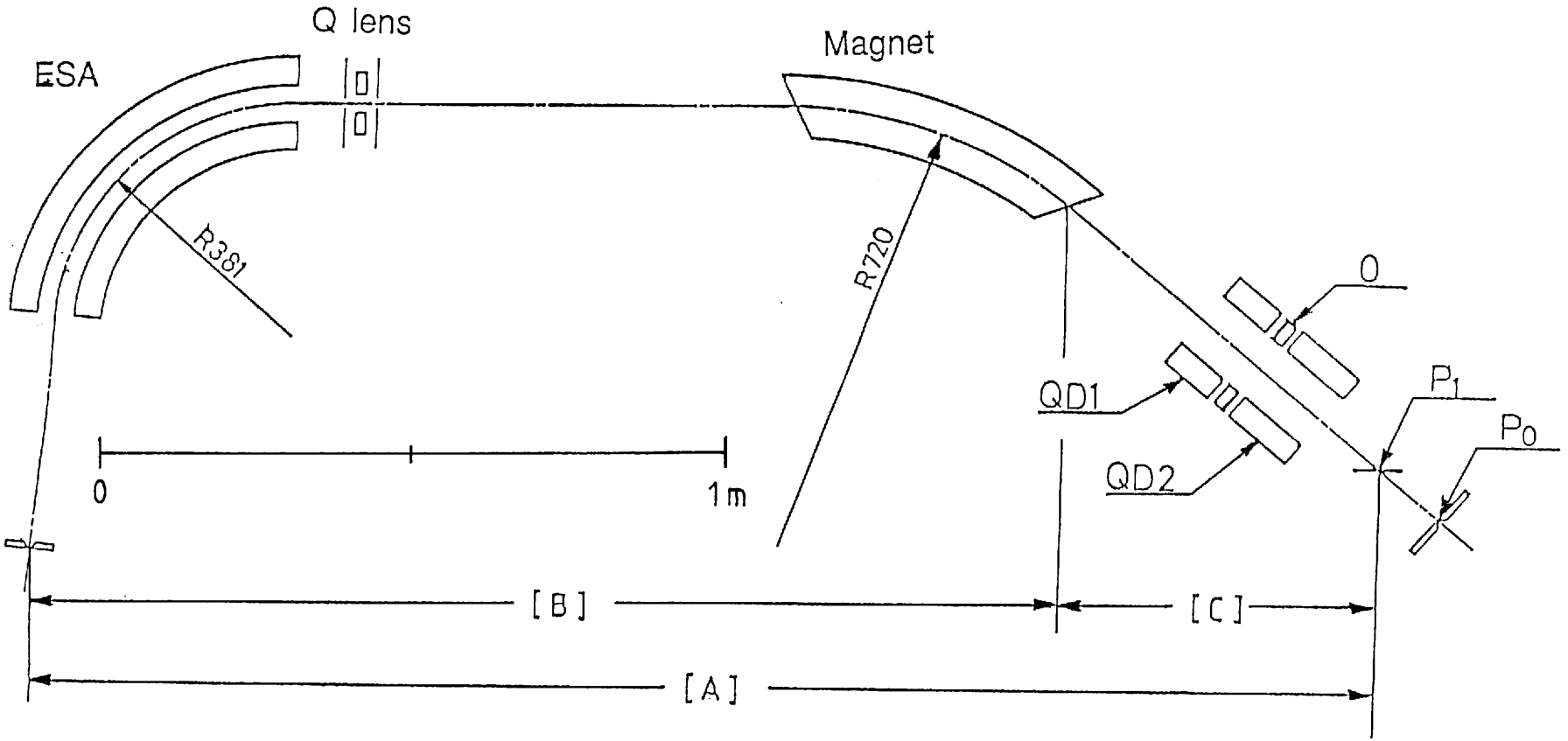

Fig. 2.5.1 Schematic drawing of the geometry of the new ion optical system. It consists of the double focusing mass spectrometer (JEOL JMS-HX110) and three additional lenses: two quadrupole lenses(QD1,QD2) and an octapole lens(O). The position P_0 is the double focusing point in the case where all additional lenses are off. A simultaneous detector is located at the position P_1.

sector to P_1. The position vector $(x_1,\alpha_1,\gamma,\delta)$ at P_1 is expressed in the first order as

$$\begin{bmatrix} x_1 \\ \alpha_1 \\ \gamma \\ \delta \end{bmatrix} = \begin{bmatrix} (x|x)_A & (x|\alpha)_A & (x|\gamma)_A & (x|\delta)_A \\ (\alpha|x)_A & (\alpha|\alpha)_A & (\alpha|\gamma)_A & (\alpha|\delta)_A \\ 0 & 0 & 1 & 0 \\ 0 & 0 & 0 & 1 \end{bmatrix} \begin{bmatrix} x_0 \\ \alpha_0 \\ \gamma \\ \delta \end{bmatrix} \qquad (2.5.1)$$

where $(x|x)_A$,$(x|\alpha)_A$,...are the elements of[A] and $(x_0,\alpha_0,\gamma,\delta)$ is the initial position vector at the source slit. The matrix [A] is given by the product of [C] and [B] as

$$\begin{bmatrix} (x|x)_A & (x|\alpha)_A & (x|\gamma)_A & (x|\delta)_A \\ (\alpha|x)_A & (\alpha|\alpha)_A & (\alpha|\gamma)_A & (\alpha|\delta)_A \\ 0 & 0 & 1 & 0 \\ 0 & 0 & 0 & 1 \end{bmatrix} =$$

$$\begin{bmatrix} (x|x)_B & (x|\alpha)_B & (x|\gamma)_B & (x|\delta)_B \\ (\alpha|x)_B & (\alpha|\alpha)_B & (\alpha|\gamma)_B & (\alpha|\delta)_B \\ 0 & 0 & 1 & 0 \\ 0 & 0 & 0 & 1 \end{bmatrix} \cdot \begin{bmatrix} (x|x)_C & (x|\alpha)_C & (x|\gamma_C & (x|\delta)_C \\ (\alpha|x)_C & (\alpha|\alpha)_C & (\alpha|\gamma)_C & (\alpha|\delta)_C \\ 0 & 0 & 1 & 0 \\ 0 & 0 & 0 & 1 \end{bmatrix}$$

(2.5.2)

where $(x|x)_C$,$(x|\alpha)_C$,... are the elements of [C] and $(x|x)_B$,$(x|\alpha)_B$,... are the elements of [B]. It should be noted that the matrix [B] is only related to the original system and [C] is only related to the additional lenses.

Double focusing condition

If the point P_1 is not the angle focusing point, the distance d_α between P_1 and the angle focusing point is given by, for example, in ref.2.5.5.

$$d_\alpha = -(x|\alpha)_A/(\alpha|\alpha)_A \qquad (2.5.3)$$

The distance d_δ between P_1 and the energy focusing point is given by

$$d_\delta = -(x|\delta)_A/(\alpha|\delta)_A \qquad (2.5.4)$$

When we fulfill the angle focusing condition at the point $P_1(d_\alpha=0)$, then the energy focusing condition ($d_\delta=0$) is also satisfied; this is proved as follows. The distance d_0 from the exit of the magnetic sector to the double focusing point P_0 of the original system is given by

$$d_0 = -(x|\alpha)_B/(\alpha|\alpha)_B = -(x|\delta)_B/(\alpha|\delta)_B \qquad (2.5.5)$$

Using Eqn(2.5.5), we obtain

$$(x|\alpha)_B(\alpha|\delta)_B - (x|\delta)_B(\alpha|\alpha)_B = 0 \qquad (2.5.6)$$

The matrix[C] is composed of drift spaces, electrostatic quadrupole lenses and an electrostatic octapole lens. These components have neither mass nor energy dispersing action in a first order; thus $(x|\gamma_C) = (x|\delta)_C = (\alpha|\gamma)_C = (\alpha|\delta)_C = 0$. Then, if we define a following sub matrix of[A] from Eqn(2.5.2), this sub matrix is simply expressed by sub matrices of [B] and [C] as

$$\begin{bmatrix} (x|\alpha)_A & (x|\delta)_A \\ (\alpha|\alpha)_A & (\alpha|\delta)_A \end{bmatrix} = \begin{bmatrix} (x|x)_C & (x|\alpha)_C \\ (\alpha|x)_C & (\alpha|\alpha)_C \end{bmatrix} \cdot \begin{bmatrix} (x|\alpha)_B & (x|\delta)_B \\ (\alpha|\alpha)_B & (\alpha|\delta)_B \end{bmatrix} \qquad (2.5.7)$$

The determinant of this matrix is then obtained as

$$\begin{vmatrix} (x|\alpha)_A & (x|\delta)_A \\ (\alpha|\alpha)_A & (\alpha|\delta)_A \end{vmatrix} = \begin{vmatrix} (x|x)_C & (x|\alpha)_C \\ (\alpha|x)_C & (\alpha|\alpha)_C \end{vmatrix} \begin{vmatrix} (x|\alpha)_B & (x|\delta)_B \\ (\alpha|\alpha)_B & (\alpha|\delta)_B \end{vmatrix} = 0 \qquad (2.5.8)$$

Here we use Eqn.2.5.6. Using Eqns.2.5.3, 2.5.4 and 2.5.8, we obtain

$$d_\alpha - d_\delta = -((x|\alpha)_A(\alpha|\delta)_A - (x|\delta)_A(\alpha|\alpha)_A)/((\alpha|\alpha)_A(\alpha|\delta)_A) = 0 \qquad (2.5.9)$$

Hence, $d_\alpha = d_\delta$; in other words, the double focusing point can be moved among the optic axis by using additional lenses without disturbing the double focusing condition.

Relationship between mass range and focal plane angle

The simultaneously detectable mass range (R) is defined as

$$R = (m_2-m_1)/m_0 \qquad (2.5.10)$$

where m_0 is the mass of the ion detected at the center of the detector, and m_1 and m_2 are the minimum and the maximum mass of the ions simultaneously detected, respectively (see Fig. 2.5.2). The ratio m_1:m_2 can be approximately expressed as 1:1+2R/(2-R). We can vary R by varying the lens strength of two quadrupole lenses(QD1,QD2) while holding the double focusing condition at $P_1(d_\alpha = d_\delta = 0)$, because we can vary two parameters. For example, if QD1 is given, then QD2 is determined so that P_1 is the double focusing point. However, we cannot vary R without changing θ_α even if we can use another quadrupole lens. Let us now investigate the relationship between R and θ_α. To the first order approximation, R is given by the following equation from geometrical consideration

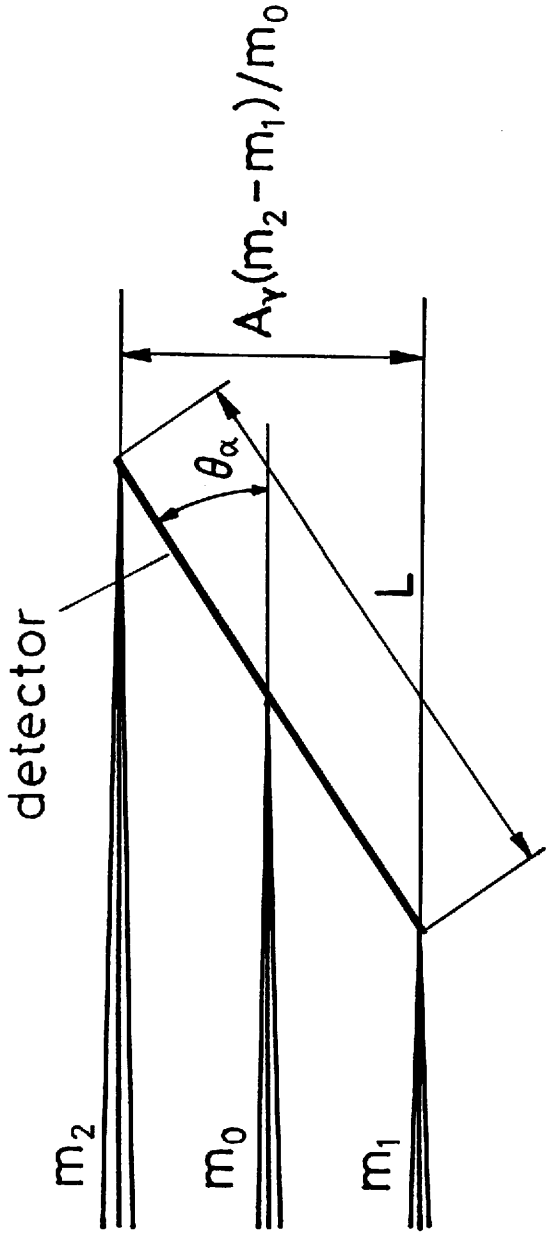

Fig. 2.5.2 Focusing details on the detector, where L is the detector length and A_γ is the mass dispersion.

$$R = (L / A_\gamma) \sin \theta_\alpha \qquad (2.5.11)$$

where $A_\gamma=(x|\gamma)_A$ is the mass dispersion and L is the detector length (see Fig. 2.5.2). The relationship between the mass dispersion A_γ and θ_α is given by (see Appendix)

$$\tan \theta_\alpha = K / A_\gamma \qquad (2.5.12)$$

where

$$K = - \{(x|\gamma)_B(\alpha|\alpha)_B - (x|\alpha)_B(\alpha|\gamma)_B\}^2 / \{(x|\alpha\gamma)_B(\alpha|\alpha)_B - (x|\alpha)_B(\alpha|\alpha\gamma')_B\} \quad (2.5.13)$$

The constant K only depends on the original system. Eliminating A_γ from Eqn(2.5.11) by using Eqn(2.5.12), we obtain the relationship between R and θ_α as

$$R = (L / K) \tan \theta_\alpha \sin \theta_\alpha \qquad (2.5.14)$$

It should be noted that the constant K is independent of the additional lenses; thus we cannot vary the mass range R without changing the angle θ_α.

Simulation of ion trajectories

The ion trajectories of the lens system were calculated by using the program TRIO. In order to determine the parameters QD1 and QD2, the parameter search program MSPLEX discussed in section 2.2 was used. Figure 2.5.3 shows the simulated [2.5.4] ion trajectories calculated up to the third order approximation under typical conditions: (a) θ_α = 38°; (b) θ_α = 27°; (c) θ_α = 16°. For this system K = 98.8mm, then the mass range covered by a 50mm detector under conditions of (a),(b) and (c) are 24% (R=0.24), 12% (R=0.12) and 4% (R=0.04), respectively. The inclination angle θ_δ of the energy focal plane also depends on the mass range. Figure 2.5.4 shows θ_α and θ_δ as a function of the mass range on a 50mm-detector. Since the angle θ_α approximately coincides with θ_δ, the double focusing condition approximately holds at least near the double focusing point P_1.

2.5.4 OCTAPOLE LENS

The focal plane is usually curved because of the third-order focusing actions of the system. It is ,therefore, possible to correct the curvature by using a third order focusing element; an electrostatic octapole lens (O) is introduced for this purpose. Figure 2.5.5 shows the simulated[2.5.4] ion trajectories with and without the octapole lens where θ_α=42°. It is clearly shown that without the octapole lens, the focal plane is strongly curved, but with octapole lens, the curvature of the focal plane is corrected. The octapole lens is expected to compensate the third order aberrations efficiently.

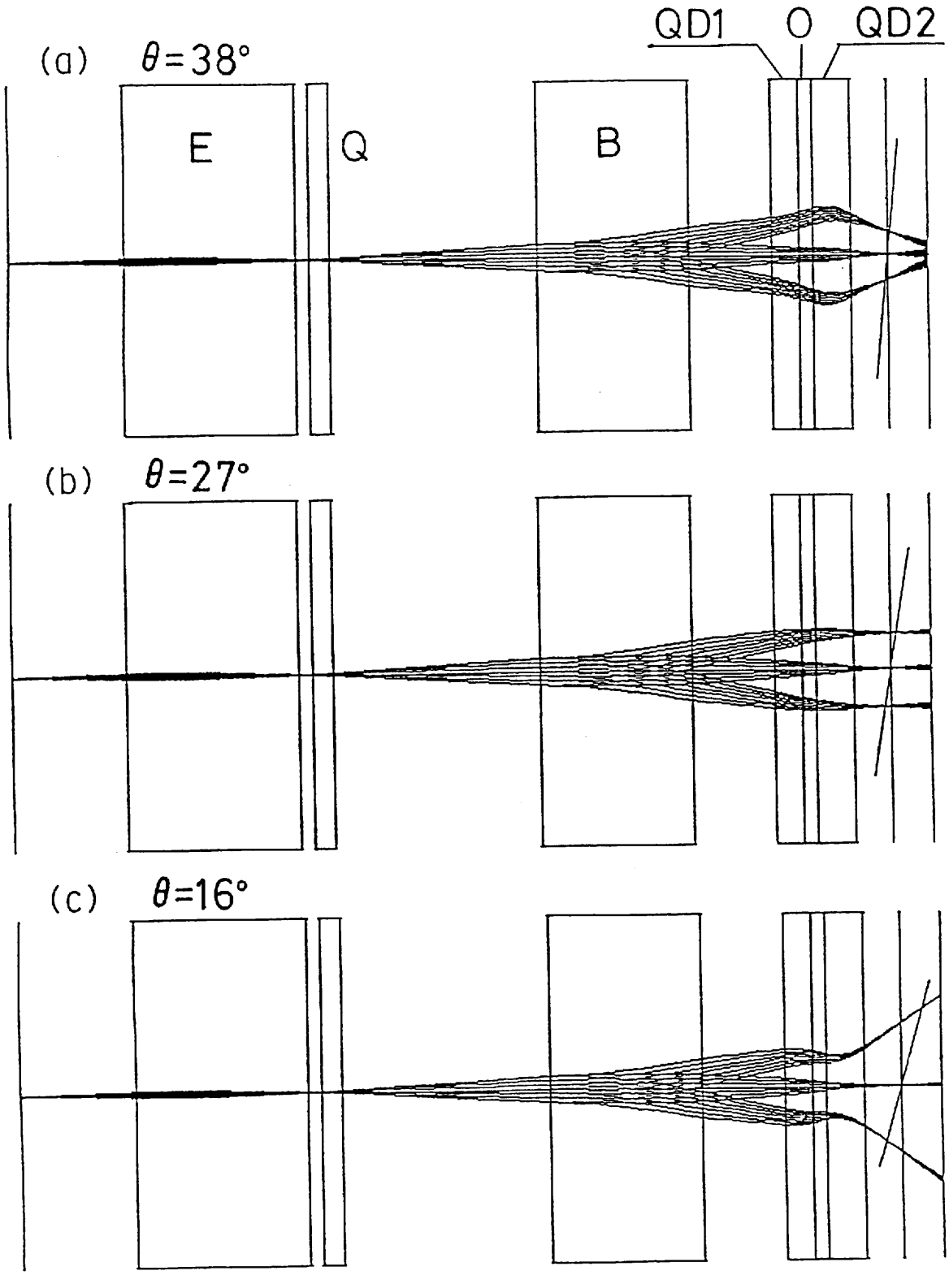

Fig. 2.5.3 Simulated ion trajectories under typical conditions. The mass difference of beam packets is 5%.
(The inclination angle of the focal plane θ_α shown in this figure is not real, because the scales of the vertical and horizontal directions are not identical.)

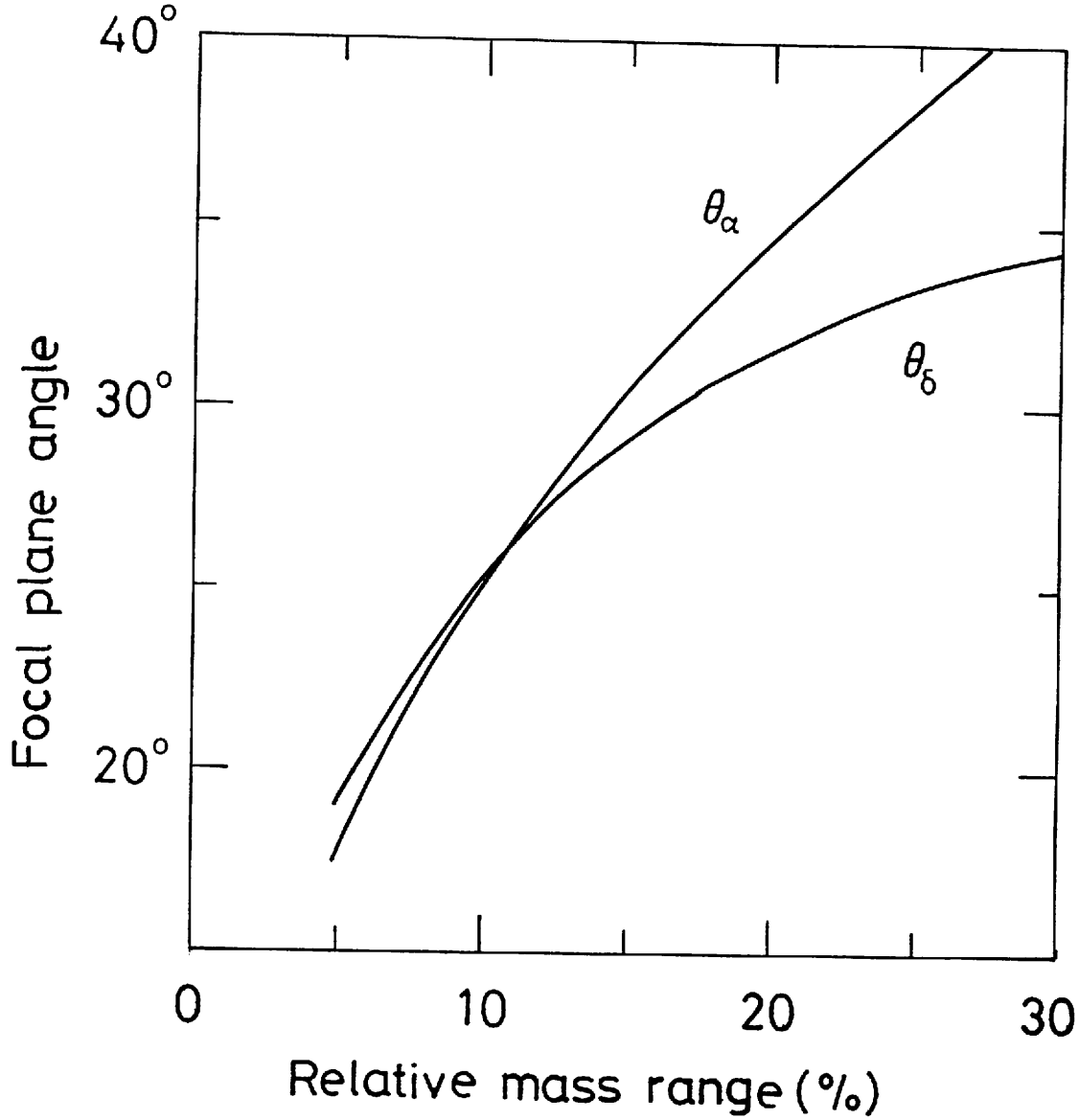

Fig. 2.5.4 Inclination angles of the angle focal plane θ_α and the energy focal plane θ_δ vs. simultaneously detectable mass range on a 50-mm detector.

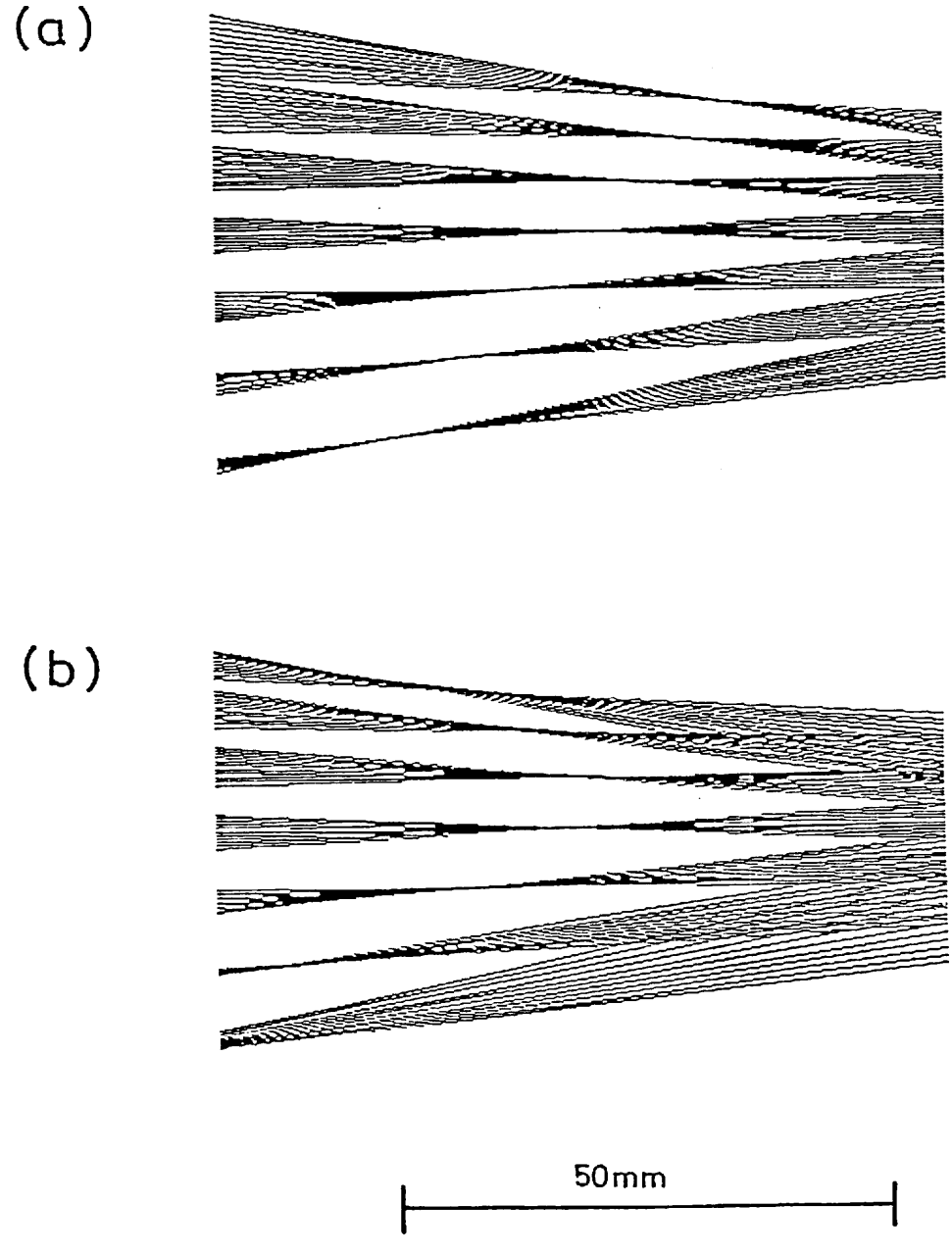

Fig. 2.5.5 Simulated ion trajectories (a) with and (b) without the octapole lens, where θ_α = 42 . The mass of beam packets distributes 15% around the center beam by 5% each. (The scales of the vertical and horizontal directions are identical.)

2.5.5 EXPERIMENTAL

The functions of the zoom lens system were tested experimentally using a 50mm and 2048 channel array detector[2.5.2]. The function of the octapole lens at θ_α=38.8° is shown in Fig 2.5.6, where the peak broadening in the high and low mass region of the spectrum is compensated by using octapole lens. Accordingly it was confirmed that the use of the octapole lens is indispensable for the zoom lens system. The mass range of the spectrum is calculated to be (460-359)/400=0.253 which is in good agreement with the theoretical value of 0.255. This is the widest mass range ever detected by a double focusing mass spectrometer using an array detector with a reasonable mass resolution. Table 2.5.1 shows the calculated and measured mass ranges for θ_α=14.9° to 38.8°. The agreement between the calculated and the measured values is quite well.

2.5.6 CONCLUSION

The ion optical system described here has following features:

1) Simultaneously detectable mass range can be varied without disturbing the double focusing condition.
2) Either a conventional point detector or array detector can be used in the same spectrometer without geometrical modification.
3) The relationship between the detectable mass range R and the inclination angle of the angle focal plane is simply given by Eqn.2.5.14.
4) The curvature of the focal plane is corrected by using the octapole lens. This is important for detecting a wide mass range simultaneously.

Finally it should be noted that by using the quadrupole-octapole-quadrupole lens system, any type of double focusing mass spectrometer can be modified for simultaneous detection of wider mass range.

REFERENCES

[2.5.1] J. S. Cottrell and S. Evans, Anal. Chem.,59 (1987) 1990.

[2.5.2] J. A. Hill, S. A. Martin, J. E. Biller and K. Biemann, Biomed. Environ. Mass Spectrom., 17 (1988) 147.

[2.5.3] H. H. Tuithof and A. J. H. Boerboom, Int. J. Mass Spectrom. Ion Phys., 20 (1976) 107.

[2.5.4] T. Matsuo, H. Matsuda, Y. Fujita and H. Wollnik, Mass Spectrosc., 24 (1976) 19.

[2.5.5] T. Matsuo, T. Sakurai and P. Derrick, Int. J. Mass Spectrom. Ion Processes, 91 (1989) 41.

Table 2.5.1 Calculated and measured mass ranges with a 50mm detector. The calculated values are obtained by using Eqn.2.5.14.

θ_α (deg)	24.9	30.1	35.9	38.8
Calculated mass range(%)	9.9	14.7	21.5	25.5
measured mass range(%)	10.0	14.5	21.0	25.3

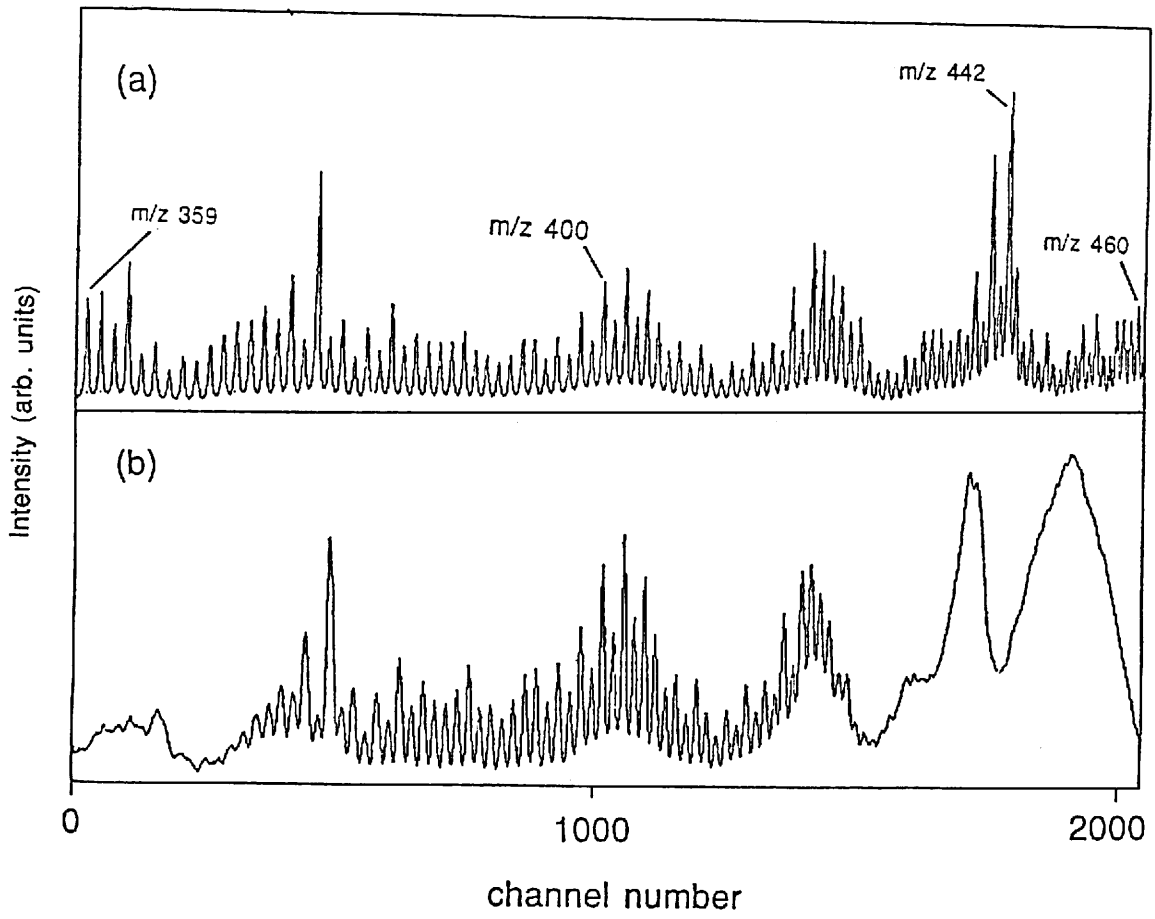

Fig. 2.5.6 Mass spectra of perfluoroalkayl phosphazine recorded by a 50mm and 2048 channel array detector (a) with, (b) without octapole lens, where $\theta_{\alpha}=38.8^{\circ}$.

3. "ELECTRA" ELECTRIC FIELD CALCULATION AND RAY TRACING PROGRAM

3.1 INTRODUCTION

In recent years, several numerical field calculation methods have been developed together with the development of the high speed computers with large memory storages[3.1]. Among these calculation methods, the charge density method is most suitable for the present purpose, because the accuracy of obtained field is very high and both two dimensional and three dimensional calculation can easily be completed. A program suitable for a ray tracing, specially for the case of a three dimensional case, did not exist. Therefore, a field calculation and ray tracing program named "ELECTRA" has been developed.

The object of this chapter is to describe the program ELECTRA which is used to calculate the electric field specified by electrodes and calculate ion trajectories of charged particles traveling in the field. The program ELECTRA can solve Laplace's equation in two dimensional, axially symmetric three dimensional and three dimensional spaces using the charge density method. In section 3.2, the charge density method is compared with other field calculation methods, then the detail of the calculation is described. The program ELECTRA has ray tracing routines employing the fourth-order Runge-Kutta method. Ion trajectories in an arbitrary electrostatic field can be obtained using the ray tracing function of ELECTRA. The program ELECTRA is a set of SUBROUTINEs written in FORTRAN77. The final section of this chapter describes the detail of the routines.

3.2 CHARGE DENSITY METHOD

3.2.1 FIELD CALCULATION METHODS

In the program ELECTRA (electric field calculation and ray tracing), a charge density method is adopted to calculate an electric field. Three methods, a Finite Difference Method (FDM), a Finite Element Method (FEM) and a Charge Density Method are mainly used for the electric field calculation in charged particle optics. These calculation methods can be divided into two categories i.e. domain method (FDM, FEM) and boundary method (Charge Density Method) [3.1]. In this section, features of those field calculation methods are discussed.

Domain method (FDM, FEM)

The procedure of the domain method is as follows:

1) The domain is divided into small elements.
2) A system of linear algebraic equations that approximate the Laplace's equation is constructed.
3) The system of equations is solved to obtain the potential values of each mesh point (node). (see Fig. 3.1)

In a finite difference method (FDM), the shape of elements is usually uniform square. Therefore the mesh generation and the construction of the system of linear equations are quite simple. Owing to this merit, the FDM have been used for long years since when digital computers were not available. However, it is difficult to specify complex electrode structures.

In an FEM, the shape of elements is typically arbitrary triangle. Accordingly it is easy to express shapes of arbitrary electrodes. Thus this method can be applied to many applications with high flexibility. However, the mesh generation and the construction of the system of linear equations are complex. These are demerits of the FEM. The use of a high speed computer with large memory storage is, therefore, indispensable for the FEM.

In those two methods (FDM, FEM), first the potential values at each mesh point are calculated, then the electric field is derived from the calculated potential values at each mesh point by numerical differentiation. Therefore, even if the potential values have small errors, the derived values of the electric field may have large errors generated in the numerical differentiation.

Boundary Method

In a boundary method, we numerically solve an integral equation which determine the charge distribution on the boundary under the applied boundary conditions. The procedure is as follows:

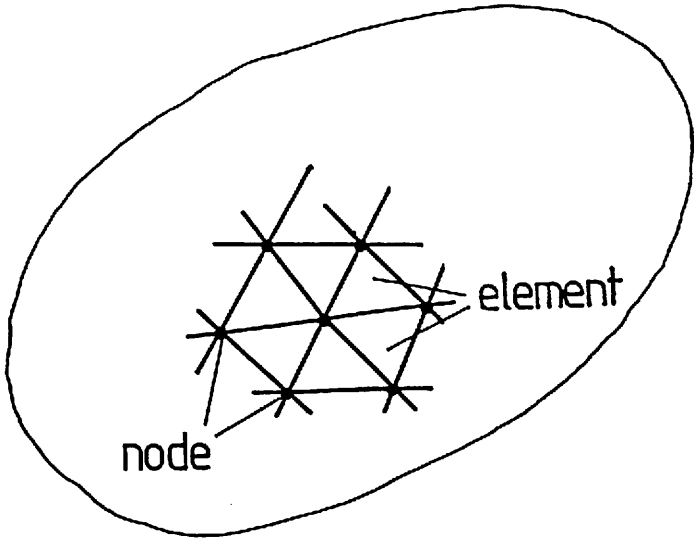

Fig. 3.1. Mesh in domain method.

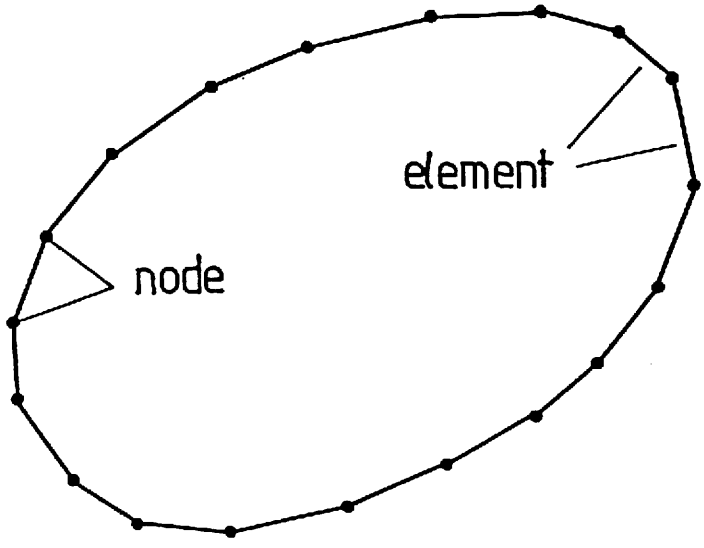

Fig. 3.2. Mesh in boundary method.

1) Only the boundary is divided into elements in order to approximate the continuous charge distribution (see Fig.3.2).

2) A system of linear algebraic equations that approximate the integral equation is constructed. By solving this, the charges of the elements are obtained.

3) The electric potential and the electric field at any point are obtained by integrating the contributions of the charges on the elements.

In contrast to domain methods, the calculated values of electric field are expected to have smaller errors because numerical differentiation process is unnecessary. This is one of merits of a boundary method. Furthermore, the mesh generation for the boundary method is much easier than that for the domain method, because only the boundary is divided into elements. This is a great advantage of the boundary method; this is very important for three dimensional problem. An example of the boundary methods is a charge density method (surface charge method). This method was developed in the 1960s [3.2] and was applied to some electrostatic lenses for electron optics [3.3]. The charge density method was originally developed under the physical consideration that the electric field can be specified by the surface charges on the electrodes. Now this method can be assumed as a special case of a more general method i.e. the Boundary Element Method (BEM) [3.4].

Since the electric potential or the electric field is calculated from the charges on elements by using Coulomb's law, the obtained potential or field exactly satisfy Maxwell's equations within round off error. Therefore even if the solution does not exactly satisfy the specified boundary condition, the solution can be assumed as an "exact solution" for a certain boundary condition. This is very important for calculations of charged particle trajectories, because the calculated trajectories can also be assumed as an "exact solution".

3.2.2 THREE DIMENSIONAL PROBLEM

The procedure of the three dimensional charge density method used in "ELECTRA" is described in this section. The brief description of the method is that first, the surface of electrodes are divided into a finite number of triangle elements. Second, the surface charge distributions of those elements are obtained under an approximation. Finally the electric field is calculated from the obtained charge distributions by using Coulomb's law.

Suppose that the electrodes are divided into m elements E_e (e=1 to m) with n nodes P_i (i=1 to n), and suppose that $\mathbf{R}_i$ is the position vector and σ_i is the charge density of the node P_i, respectively. (see Fig.3.3) Let us now discuss the expression of the charge distribution $\sigma(\mathbf{R})$. Since $\sigma(\mathbf{R})$ cannot be expressed by an analytical form, we use an approximation. Here we assume that $\sigma(\mathbf{R})$ is varied linearly in an individual element (linear element), see Fig.3.4. This is not a necessary choice. For example we can assume $\sigma(\mathbf{R})$ is constant (constant element). However, in this case, accuracy of the calculation decreases, while complexity of the calculation decreases a little. Another possibility is to use higher order approximation. But, in this case, the expression of the function becomes very complex. Thus we use the linear element here.

Supposing that P_i, P_j, P_k are the nodes of an element E_e, we can express the charge density distribution $\sigma_e(\mathbf{R})$ on the element as

$$\sigma_e(\mathbf{R}) = f_{ie}(\mathbf{R})\sigma_i + f_{je}(\mathbf{R})\sigma_j + f_{ke}(\mathbf{R})\sigma_k \qquad (3.1)$$

where the values of functions $f_{ie}(\mathbf{R})$, $f_{je}(\mathbf{R})$, $f_{ke}(\mathbf{R})$ vary linearly in E_e and are zero if the point $\mathbf{R}$ does not lie on surface of the element, see Fig.3.5. These functions can be specified if their values are given at three nodes E_e as

$$\sigma_i = \sigma_e(\mathbf{R}_i) = f_{ie}(\mathbf{R}_i)\sigma_i + f_{je}(\mathbf{R}_i)\sigma_j + f_{ke}(\mathbf{R}_i)\sigma_k$$

$$\sigma_j = \sigma_e(\mathbf{R}_j) = f_{ie}(\mathbf{R}_j)\sigma_i + f_{je}(\mathbf{R}_j)\sigma_j + f_{ke}(\mathbf{R}_j)\sigma_k$$

$$\sigma_k = \sigma_e(\mathbf{R}_k) = f_{ie}(\mathbf{R}_k)\sigma_i + f_{je}(\mathbf{R}_k)\sigma_j + f_{ke}(\mathbf{R}_k)\sigma_k \qquad (3.2)$$

Then the functions should satisfy the following equations.

$$f_{ie}(\mathbf{R}_i) = 1 \quad f_{je}(\mathbf{R}_i) = 0 \quad f_{ke}(\mathbf{R}_i) = 0$$

$$f_{ie}(\mathbf{R}_j) = 0 \quad f_{je}(\mathbf{R}_j) = 1 \quad f_{ke}(\mathbf{R}_j) = 0$$

$$f_{ie}(\mathbf{R}_k) = 0 \quad f_{je}(\mathbf{R}_k) = 0 \quad f_{ke}(\mathbf{R}_k) = 1 \qquad (3.3)$$

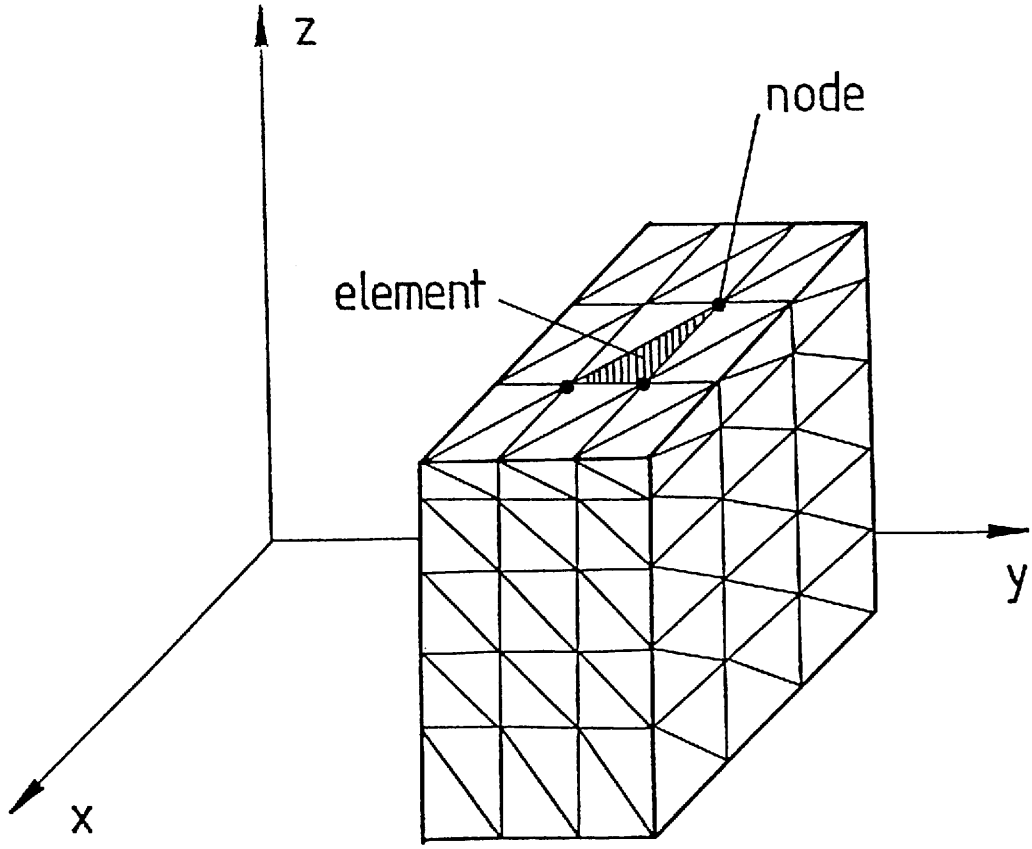

Fig. 3.3. Schematic drawing of the mesh on the surface.

A position on the element can be expressed by introducing two variables u_1, u_2 as

$$\mathbf{R} = \mathbf{R}_i + 1/2(1+u_1)(\mathbf{R}_j-\mathbf{R}_i) + 1/4(1+u_1)(1+u_2)(\mathbf{R}_k-\mathbf{R}_j)$$

$$(-1 < u_1 < 1, -1 < u_2 < 1) \qquad (3.4)$$

Using these variables, we can express $f_{ie}(\mathbf{R})$, $f_{je}(\mathbf{R})$ and $f_{ke}(\mathbf{R})$ as

$$f_{ie}(\mathbf{R}) = (1-u_1)/2$$

$$f_{je}(\mathbf{R}) = (1+u_1)(1-u_2)/4$$

$$f_{ke}(\mathbf{R}) = (1+u_1)(1+u_2)/4 \qquad (3.5)$$

Define that $f_{ie}(\mathbf{R}) = 0$ if the element E_e dose not include P_i, then we can rewrite Eqn 3.1 as

$$\sigma_e(\mathbf{R}) = \sum_{i=1}^{n} f_{ie}(\mathbf{R})\sigma_i \qquad (3.6)$$

The charge distribution of all elements $\sigma(\mathbf{R})$ can be then obtained as

$$\sigma(\mathbf{R}) = \sum_{e=1}^{m} \sigma_e(\mathbf{R}) = \sum_{i=1}^{n} \sigma_i \sum_{e=1}^{m} f_{ie}(\mathbf{R}) \qquad (3.7)$$

Now the expression of the charge distribution has been obtained. (This expression was newly derived). The next step is to obtain a system of linear equations which gives charge densities σ_i. The electric potential $V(\mathbf{R})$ at an arbitrary position is given from Coulomb's law as

$$V(\mathbf{r}) = \int \frac{\sigma(\mathbf{R})}{|\mathbf{r}-\mathbf{R}|}\, ds$$

$$= \sum_{i=1}^{n}\sigma_i \sum_{e=1}^{m} \int_{s_e} \frac{f_{ie}(\mathbf{R})}{|\mathbf{r}-\mathbf{R}|}\, ds \qquad (3.8)$$

where S_e denotes the surface of the element E_e. We put the dielectric constant $\varepsilon_0=1/4\pi$ for simplicity. Substituting $\mathbf{r}_i$ into Eqn.3.8 gives

$$V(\mathbf{R}_i)= v_i = \sum_{i=1}^{n}\sigma_i \sum_{e=1}^{m} \int_{s_e} \frac{f_{ie}(\mathbf{R})}{|\mathbf{R}_i-\mathbf{R}|}\, ds = \sum_{j=1}^{n}\sigma_i \sum_{e=1}^{m} A_{ije} = \sum_{j=1}^{n} A_{ij}\sigma_i \qquad (3.9)$$

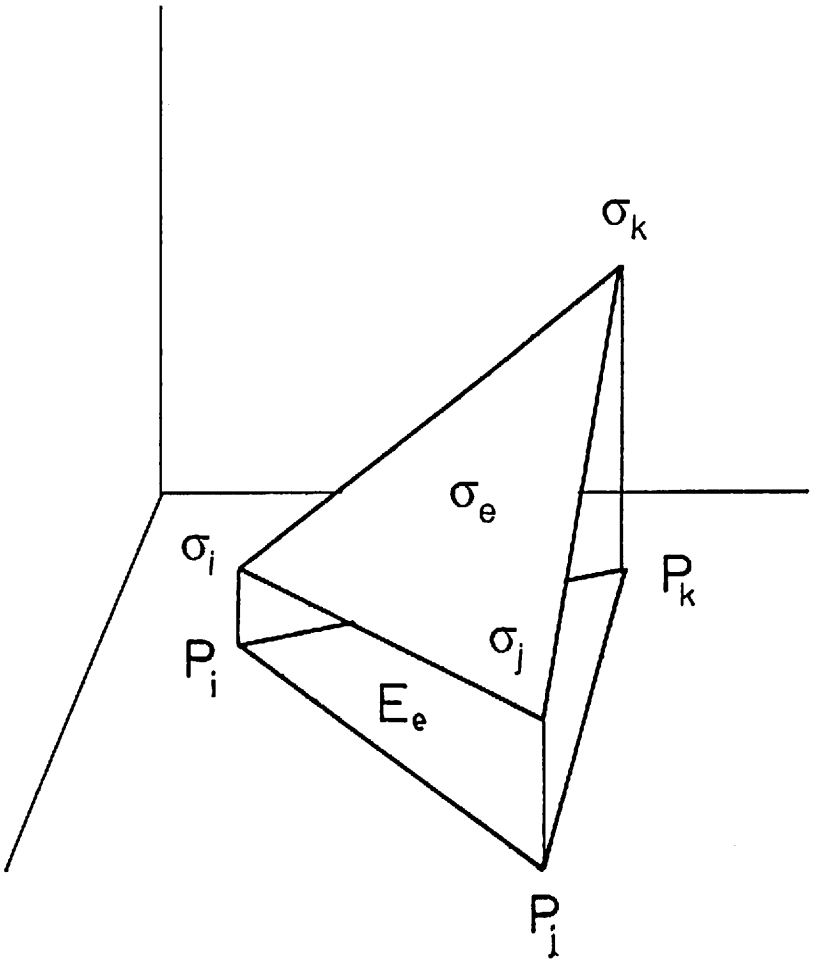

Fig. 3.4. Schematic drawing of charge distribution σ_e on a element.

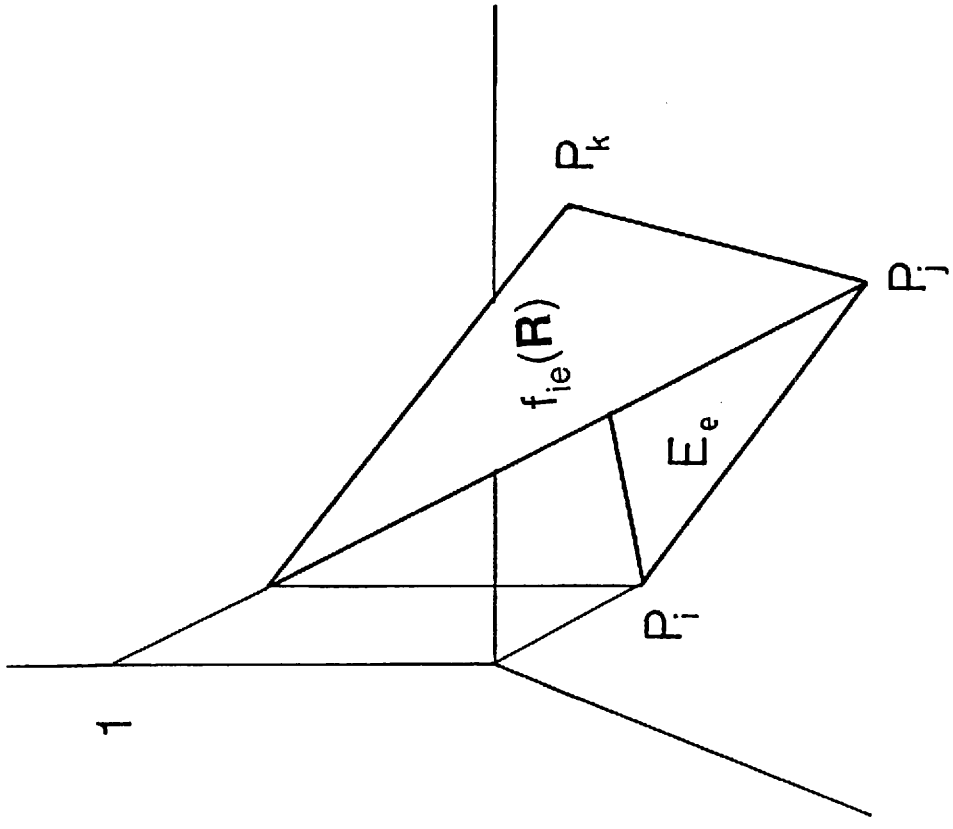

Fig. 3.5. Schematic drawing of function $f_{ie}(\mathbf{R})$.

where

$$A_{ije} = \int_{s_e} \frac{f_{je}(\mathbf{R})}{|\mathbf{R}_i - \mathbf{R}|} ds \qquad (3.10)$$

$$A_{ij} = \sum_{e=1}^{n} A_{ije}$$

The relationship between the potential V_i and the charge density σ_i is then expressed by the following system of linear equations

$$\begin{bmatrix} A_{11} & A_{12} & \cdots & A_{1n} \\ A_{21} & A_{22} & \cdots & A_{2n} \\ & & & \\ A_{n1} & A_{n2} & \cdots & A_{nn} \end{bmatrix} \begin{bmatrix} \sigma_1 \\ \sigma_2 \\ \\ \sigma_n \end{bmatrix} = \begin{bmatrix} V_1 \\ V_2 \\ \\ V_n \end{bmatrix} \qquad (3.11)$$

When the shape of the elements and the potentials at the nodes are given, then we can integrate Eqn.3.10 and can solve Eqn.3.11 for σ_i.

In order to calculate A_{ije}, we have to integrate a function over the triangle region. The integration can be done using variables u_1, u_2 defined by Eqn.3.4. Supposing here that $g(\mathbf{R})$ is an arbitrary function defined in the element E_e which include the nodes P_i, P_j, P_k, we have the following equation as

$$I = \int_{s_e} g(\mathbf{R})\, ds$$

$$= S_e/4 \int_{-1}^{1}\int_{-1}^{1} (1+u_1) g\{\mathbf{R}(u_1,u_2)\}\, du_1 du_2 \qquad (3.12)$$

where S_e is the area of E_e. Since usually it is very difficult to integrate this analytically, a numerical method is used. We use, in ELECTRA, a Gauss integration formula for integrating with respect to both u_1 and u_2. The formula is

$$I \approx 1/4\ S_e \sum_{a=1}^{N}\sum_{b=1}^{N} w_a w_b (1+u_{1a}) g(r_{ab}) \qquad (3.13)$$

where

$$r_{ab} = \mathbf{R}_i + 1/2(1+u_{1a})(\mathbf{R}_j - \mathbf{R}_i) + 1/4(1+u_{1a})(1+u_{2b})(\mathbf{R}_k - \mathbf{R}_j)$$

and where u_{1a},u_{2b} are the abscissas and w_a,w_b are the weight factors of the N-point Gauss integration formula, respectively. The values of those parameters are generated by a method described in Ref.3.7.

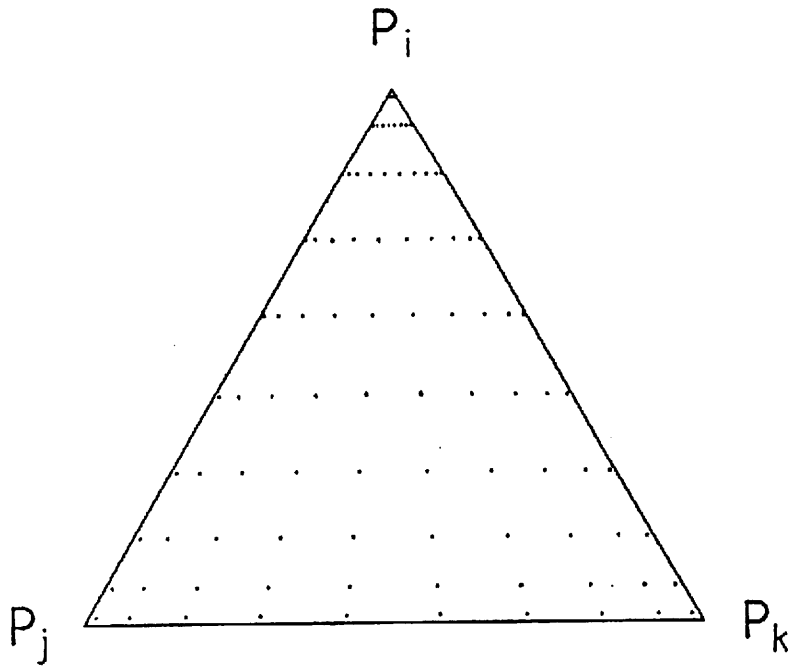

Fig. 3.6. Distribution of the sampling points in two dimensional Gauss integration on a triangle element.

Figure 3.6 shows a distribution of the sampling points r_{ab} for N = 10. It is shown that the density of the sampling points near P_i is higher than that of P_j or P_k. This difference is caused by the definition of the variables u_1, u_2.

When we calculate such values A_{iie}, we have to be careful to use this formula, because the integrand

$$\{f_{ie}(\mathbf{R})/|\mathbf{R}-\mathbf{R}_i|\}ds \qquad (3.14)$$

has a singular point at $\mathbf{R}=\mathbf{R}_i$. If we use the variables defined by Eqn 3.4, we can neglect the effect of the singular point. In this case the integrand of A_{iie} is expressed as

$$\frac{f_{ie}(\mathbf{R})}{|\mathbf{R}_i-\mathbf{R}|}ds = \frac{(1+u_1)f_{ie}\{\mathbf{R}(u_1,u_2)\}}{|(1+u_1)(\mathbf{R}_j-\mathbf{R}_i) + 1/2(1+u_2)(\mathbf{R}_k-\mathbf{R}_j)|}du_1du_2$$

$$= \frac{f_{ie}\{\mathbf{R}(u_1,u_2)\}}{|(\mathbf{R}_j-\mathbf{R}_i) + 1/2(1+u_2)(\mathbf{R}_k-\mathbf{R}_j)|}du_1du_2 \qquad (3.15)$$

Since the vectors $(\mathbf{R}_i-\mathbf{R}_j)$ and $(\mathbf{R}_k-\mathbf{R}_j)$ are independent of each other, the denominators of Eqn 3.15 never has the value of zero; thus the equation has no singular point. However, if we use the same variables, we cannot neglect the affect of the singular point $\mathbf{R}_j$ of A_{jje}. Therefore it is expected that the accuracy of the numerically calculated value of A_{iie} is much higher than that of A_{jje}. This is clearly shown in Table 3.1, where an example of the results of the numerical calculations of A_{iie} and A_{jje} are given. Both values, A_{iie} and A_{jje}, must be identical in this case, because the element is an regular triangle. Therefore the difference between A_{iie} and A_{jje} shown in Table 3.1. is only caused by the definition of the variables (Eqn.3.4). Hence we can also calculate A_{jje} with high accuracy by changing the definition of the variables. (This calculation method was newly derived.)

Once the charge density σ_i is obtained, the electric field at an arbitrary position $\mathbf{E}(\mathbf{r})$ can be calculated by the following formula:

$$\mathbf{E}(\mathbf{r}) = \int \frac{\mathbf{r}-\mathbf{R}}{|\mathbf{r}-\mathbf{R}|^3}\sigma(\mathbf{R})ds \qquad (3.16)$$

Table 3.1 Values of A_{iie} and A_{jje} calculated by the Gauss integration formula.

N	A_{iie}	A_{jje}
2	.474341649025257	.373333203740171
3	.475797480326466	.425272694431533
4	.475707690488951	.445655879814213
5	.475713426894629	.455754173655190
6	.475713052157209	.461491310391398
7	.475713077008890	.465063626790946
8	.475713075342710	.467439142233652
9	.475713075455347	.469099037337788
10	.475713075447682	.470304665235698
11	.475713075448207	.471208005586244
12	.475713075448171	.471902363206605
13	.475713075448173	.472447610174208
14	.475713075448173	.472883603788097
15	.475713075448172	.473237714387217
16	.475713075448173	.473529244139603
17	.475713075448173	.473772122770582
18	.475713075448173	.473976607712658
19	.475713075448172	.474150387895313
20	.475713075448174	.474299318871473
21	.475713075448174	.474427923615532
22	.475713075448173	.474539740651761
23	.475713075448174	.474637570490820
24	.475713075448173	.474723652967471
25	.475713075448172	.474799796771868
26	.475713075448173	.474867475358529
27	.475713075448174	.474927898851450
28	.475713075448174	.474982068574925
29	.475713075448172	.475030818848234
30	.475713075448174	.475074849334369

3.2.3 TWO DIMENSIONAL PROBLEM

The principle of the two dimensional problem is almost the same as that of the three dimensional problem. We assume here that the potential V(x,y) is anti-symmetry with x-axis

$$V(x,y)= -V(x,-y) \qquad (3.17)$$

In this case the charge distribution is also anti-symmetry with x-axis. Thus, if the line charge density (charge per unit length) at the point (X,Y) is λ then the line charge density at (X,–Y) must be $-\lambda$. The contribution of the charge density λ at (X,Y) to the potential at (x,y) is then expressed as

$$V(x,y) = \lambda/2\ [\log\{(x-X)^2 + (y-Y)^2\}-\log\{(x-X)^2 + (y+Y)^2\}]$$

$$= \lambda\ F(x,y,X,Y) \qquad (3.18)$$

where the contribution of the charge density at (X,-Y) is included. We put here the dielectric constant $\varepsilon_0=1/2\pi$ for simplicity. A function F(x,y,X,Y) is also defined here. In this expression, x–axis is the earth potential and the boundary condition

$$V(x,y) = 0 \qquad \left(\sqrt{(x-X)^2+(y-Y)^2} \rightarrow \infty \right) \qquad (3.19)$$

is satisfied.

The construction of the system of linear algebraic equations is similar to that of the three dimensional problem. In the two dimensional problem, the surfaces of electrodes is divided into m elements of linear strings E_e (e=1 to m) with n nodes P_i(i=1 to n), see Fig.3.7. Supposing that σ_i are charge density (charge per unit area) at nodes P_i and suppose that the charge density is assumed to vary linearly on each element (see Fig. 3.8). Then the charge density distribution on an element E_e including P_i and P_j can be expressed as

$$\sigma_e = f_{ie}(x,y)\ \sigma_i + f_{je}(x,y)\ \sigma_j \qquad (3.20)$$

The functions $f_{ie}(x,y)$ and $f_{je}(x,y)$ can be specified from the definition of σ_i and σ_j:

$$\sigma_i = \sigma_e(X_i,Y_i)= f_{ie}\ (X_i,Y_i)\sigma_i + f_{je}(X_i,Y_i)\ \sigma_j$$

$$\sigma_j = \sigma_e(X_j,Y_j)= f_{ie}\ (X_j,Y_j)\sigma_i + f_{je}(X_j,Y_j)\ \sigma_j \qquad (3.21)$$

where (X_i,Y_i) and $(X_j.Y_j)$ are the coordinates of P_i and P_j, respectively. For example

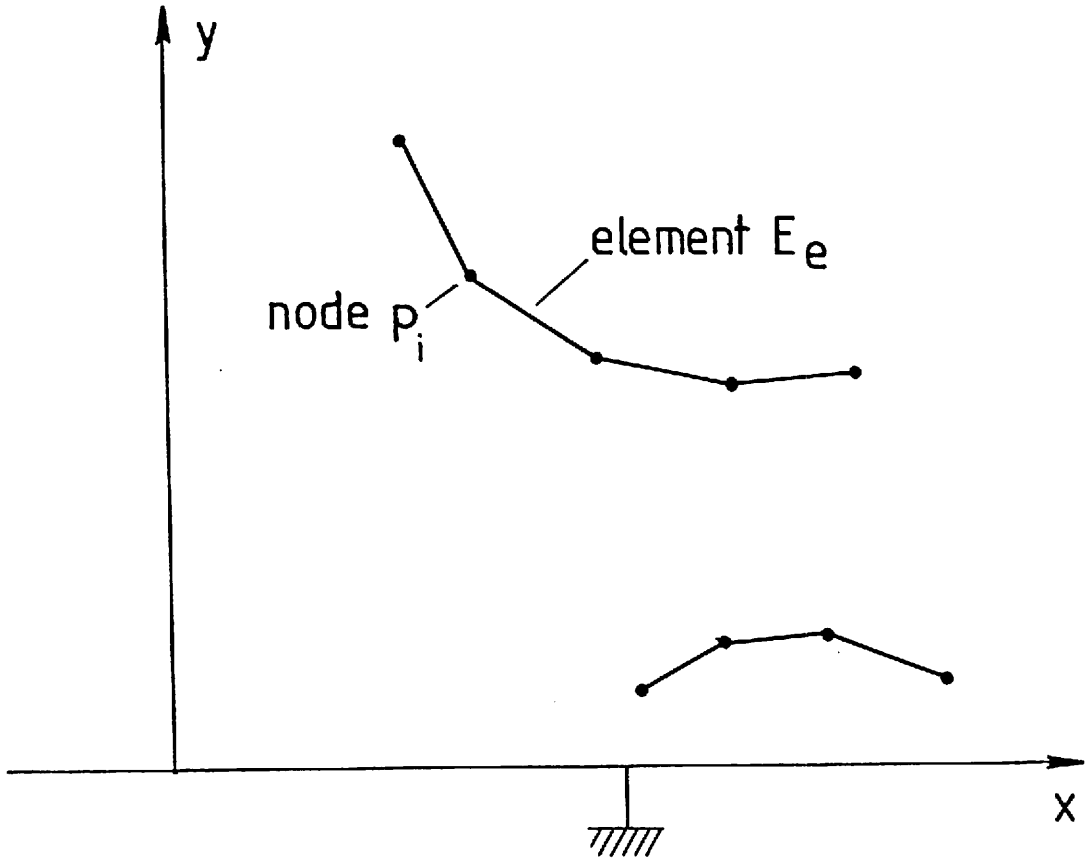

Fig. 3.7. Schematic drawing of two dimensional mesh.

$f_{ie}(x,y)$ and $f_{je}(x,y)$ can be expressed as

$$f_{ie}\{x(u),y(u)\} = (1-u)/2 \quad f_{ie}(x(u),y(u)) = (1+u)/2 \qquad (3.22)$$

where

$$x(u) = (1-u)X_i/2 + (1+u)X_j/2$$

$$y(u) = (1-u)Y_i/2 + (1+u)Y_j/2 \qquad (3.23)$$

Similar to Eqn. 3.7, the charge distribution on all elements is expressed (see Fig. 3.8) as

$$\sigma(X,Y) = \sum_{i=1}^{n} \sigma_i \sum_{e=1}^{m} f_{ie}(X,Y) \qquad (3.24)$$

(This expression was newly derived). If the charge distribution is obtained, the potential is given by using Eqn.3.18; $v(x,y) = \int F(x,y,X,Y)d\lambda = \int F(x,y,X,Y)\sigma ds$.
If the potential value V_i at the node P_i is given then we have

$$V_i = V(X_i,Y_i)$$

$$= \sum_{j=1}^{n} \sigma_j \sum_{e=1}^{m} \int_{s_e} f_{je}(X,Y)\ F(X_i,Y_i,X,Y)\ ds$$

$$= \sum_{j=1}^{n} \sigma_j \sum_{e=1}^{m} A_{ije}$$

$$= \sum_{j=1}^{n} A_{ij}\sigma_j \qquad (3.25)$$

where

$$A_{ije} = \int_{s_e} f_{je}(X,Y)F(X_i,Y_i,X,Y)\ ds \qquad (3.26)$$

$$A_{ij} = \sum_{e=1}^{m} A_{ije}$$

Using Eqn.3.25, we have a system of linear equations

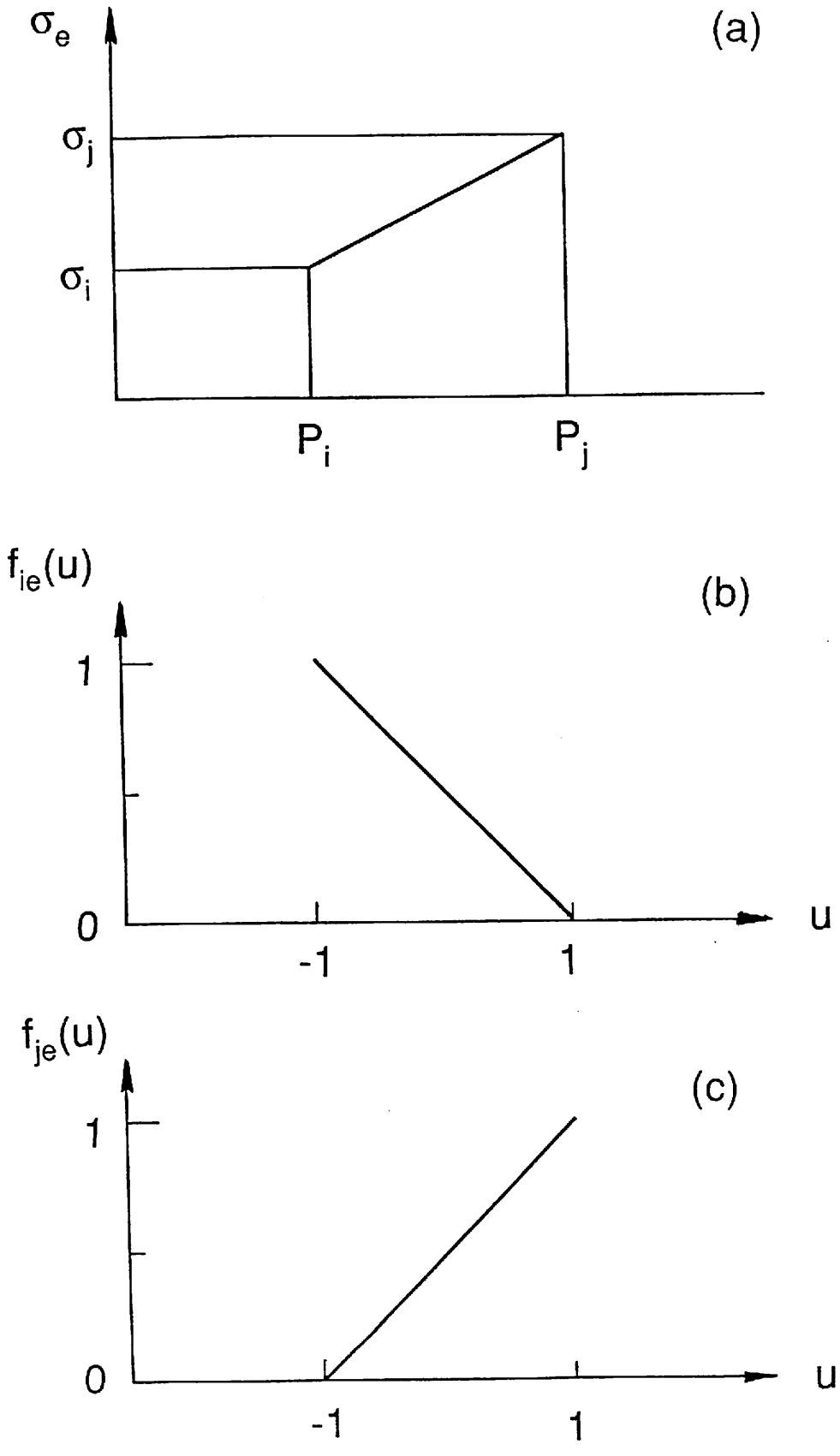

Fig. 3.8. Schematic drawings of (a) charge distribution σ_e, (b) function $f_{ie}(u)$, (c) function $f_{je}(u)$.

$$\begin{bmatrix} A_{11} & A_{12} & \cdots\cdots & A_{1n} \\ A_{21} & A_{22} & \cdots\cdots & A_{2n} \\ & & & \\ A_{n1} & A_{n2} & \cdots\cdots & A_{nn} \end{bmatrix} \begin{bmatrix} \sigma_1 \\ \sigma_2 \\ \\ \sigma_n \end{bmatrix} = \begin{bmatrix} v_1 \\ v_2 \\ \\ v_n \end{bmatrix} \qquad (3.27)$$

We can obtain the values of σ_i by solving above equation.

We use a Gauss integration formula for integrating Eqn.3.26.

$$A_{ije} = l_e \sum_{k=1}^{N} w_k \, f_{je}\{X(u_k),Y(u_k)\} \; F\{X_i,Y_i,X(u_k),Y(u_k)\} \qquad (3.28)$$

where

$$l_e = \sqrt{(X_i-X_j)^2 + (Y_i-Y_j)^2}$$

and where u_k and w_k are respectively the abscissas and weight factors for N point gauss integration formula.

The integrand of A_{iie} has singular point at (X_i,Y_i). In this case, we can calculate this value analytically. The singularity appear in the first term of F(x,y,X,Y) as

$$[f_{ie}(X,Y) \log\{(X_i-X)^2 + (Y_i-Y)^2\}]ds$$

$$= l_e[(1-u)/2 \log\{1/4 \; l_e^2(1+u)^2\}]du \qquad (3.29)$$

where u = -1 is the singular point. This integration can be done analytically, the result is

$$\int_{-1}^{1} [(1-u)/2 \log\{(1/4) \; l_e^2(1+u)^2\}]du = 2\log(l_e)-1 \qquad (3.30)$$

The electric field is also calculated from the charge densities as

$$E_x(x,y) = \int_S (x-X)(1/L_+^2 + 1/L_-^2)\sigma(X,Y)ds$$

$$E_y(x,y) = \int_S \{(y-Y)/L_+^2 + (y+Y)/L_-^2)\sigma(X,Y)\}ds \qquad (3.31)$$

where

$$L_+^2 = (x-X)^2 + (y-Y)^2$$

$$L_-^2 = (x-X)^2 + (y+Y)^2$$

3.2.4 AXIALLY SYMMETRIC THREE DIMENSIONAL PROBLEM

The axially symmetric three dimensional problem can be solved by a similar way to the two dimensional problem. The notation of the nodes P_i and the elements E_e used in this section are almost the same as that of the two dimensional problem (see section 3.3).

However the expression of the potential becomes much complex because a point (R,Z) of cylindrical coordinates means a ring in the three dimensional space (see Fig. 3.9). The contribution of the charge Q on this ring to the potential value of a point (r,z) is given as [3.1]

$$v(r,z) = \frac{K(k)}{\{(r+R)^2+(z-Z)^2\}^{1/2}} \quad Q \qquad (3.32)$$

where

$$k = \left\{ \frac{4rR}{(r+R)^2+(z-Z)^2} \right\}^{1/2} \qquad (3.33)$$

and where K(k) is the complete elliptic integral of the first kind

$$K(k) = \int_0^{\pi/2} \frac{d\theta}{(1-k^2\sin^2\theta)^{1/2}} \qquad (3.34)$$

In above expression we put the dielectric constant $\varepsilon_0 = 1/2\pi^2$ for simplicity.

Suppose that σ_i is charge density of a node $P_i(R_i,Z_i)$. We define here linear charge density $\lambda_i = 2\pi R_i\sigma_i$. Then the charge distribution $\lambda_e(R,Z)$ on an element E_e including P_i and P_j is given as the similar form as Eqn.3.20

$$\lambda_e(R,Z) = f_{ie}(R,Z)\ \lambda_i + f_{je}(R,Z)\ \lambda_j \qquad (3.35)$$

where the functions $f_{ie}(R,Z)$, $f_{je}(R,Z)$ are defined by Eqns.3.22, 3.23. The charge distribution $\lambda(R,Z)$ in all elements is given in the similar form of Eqn 3.24 as

$$\lambda(R,Z) = \sum_{i=1}^{n} \lambda_i \sum_{e=1}^{m} f_{ie}(R,Z) \qquad (3.36)$$

(This expression is newly derived). If the potentials V_i at the nodes P_i are given, a system of linear equations is given as

$$\begin{bmatrix} A_{11} & A_{12} & \cdots & A_{1n} \\ A_{21} & A_{22} & \cdots & A_{2n} \\ & & & \\ A_{n1} & A_{n2} & \cdots & A_{nn} \end{bmatrix} \begin{bmatrix} \lambda_1 \\ \lambda_2 \\ \\ \lambda_n \end{bmatrix} = \begin{bmatrix} V_1 \\ V_2 \\ \\ V_n \end{bmatrix} \qquad (3.37)$$

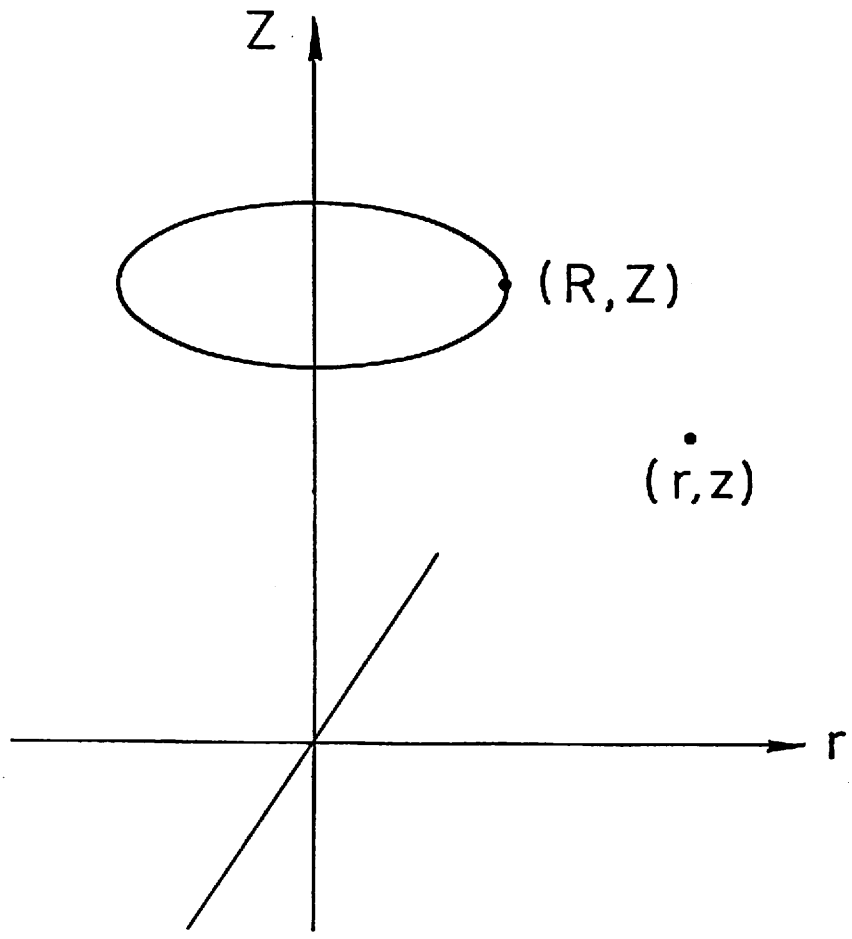

Fig. 3.9. Schematic drawing of axially symmetric three dimensional problem.

where

$$A_{ije} = \int_{s_e} \frac{f_{je}(R,Z)K(k)ds}{\{(r+R)^2+(z-Z)^2\}^{1/2}} \qquad (3.38)$$

$$A_{ij} = \sum_{e=1}^{m} A_{ije}$$

We use here again a Gauss integration formula for calculating A_{ije}. In similarly with the two dimensional problem, A_{iie} has a singular point at $(R,Z)=(r_i,z_i)$; at this point k=1, while K(k) has the singularity at k=1. In order to calculate this element, we use the double exponential formula[3.6] which was developed for calculate a value of a definite integration where an integrand has singularities. Description of the formula is as follows: Suppose that g(x) is an arbitrary function and suppose

$$I = \int_{-1}^{1} g(x)dx \qquad (3.39)$$

If we transform the parameter x into u by

$$x(u) = \tanh(A \sinh u), \ (A = \pi/2)$$

The relation u and x is shown in Fig. 3.10; $u=-\infty$ for x=-1 and $u=+\infty$ for x=1. The integration is then expressed as

$$I = \int_{-\infty}^{\infty} g\{x(u)\} \ A \cosh(u)/\cosh^2\{A \sinh(u)\}dx \qquad (3.40)$$

Applying a trapezoidal integration formula to Eqn 3.40. we obtain the double exponential formula as

$$I = h \sum_{t=-\infty}^{\infty} w_t g(x_t) \qquad (3.41)$$

where

$$x_t = \tanh\{a \sinh(t \cdot h)\}$$

$$w_t = a \cosh(t \cdot h)/\cosh^2\{a \sinh(t \cdot h)\} \qquad (3.42)$$

and where h is the step of the integration. In this formula we have to sum the series $w_t g(x_t)$ from $t=-\infty$ to $t=+\infty$; this is a demerit of the double exponential formula. However this can be removed because the weight factor w_t decreases quickly as $|t \cdot h|$ is increases (see Fig.3.11); for example $w_t = 2.8\times10^{-21}$ at $|t \cdot h| = 3.5$. Thus the contributions of the

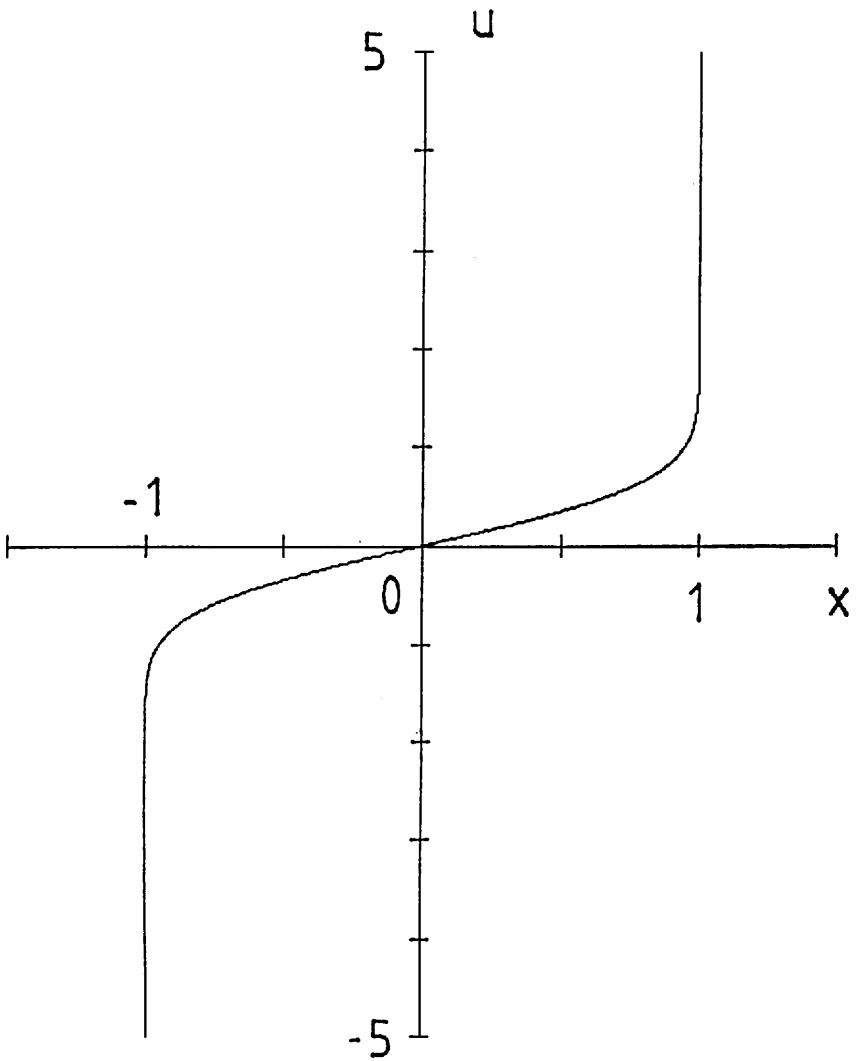

Fig. 3.10. Relationship between u and x, where x(u)=tanh(π/2 sinh u).

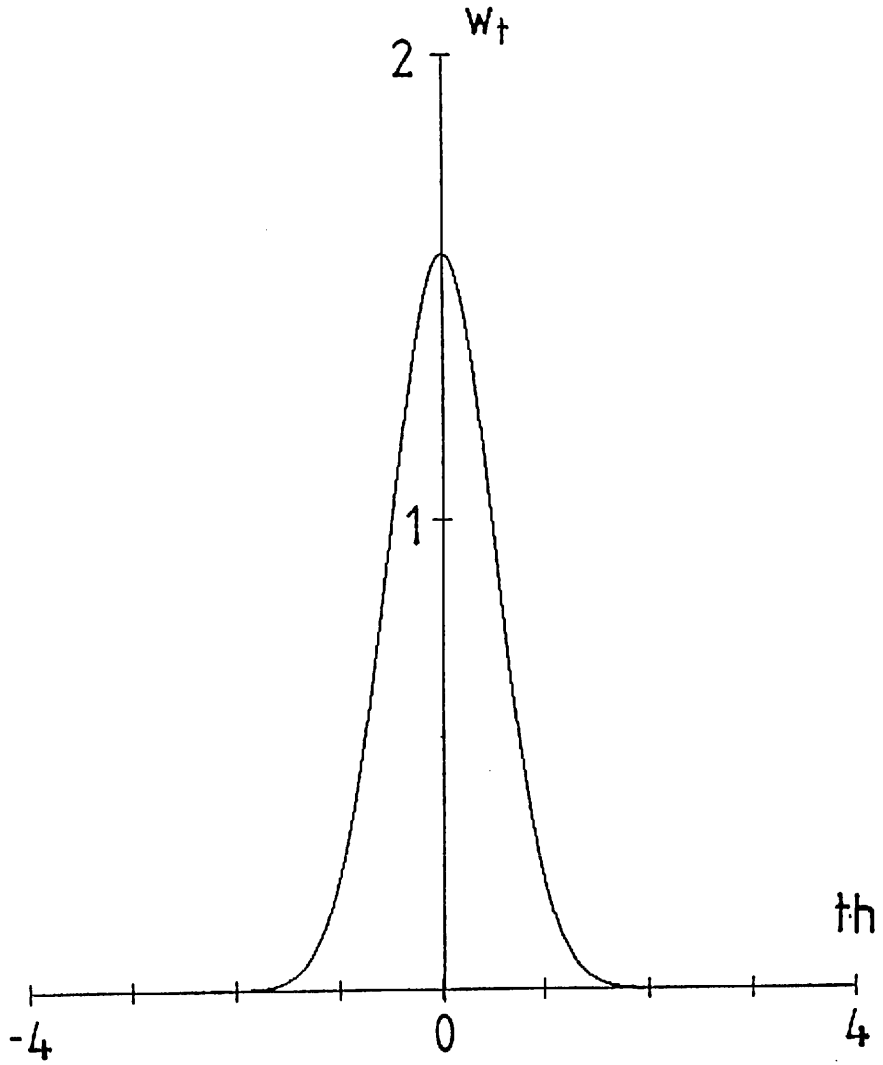

Fig. 3.11. Distribution of weight factor $w_t(th)=\pi/2\ \cosh(t\cdot h)/\cosh^2\{\pi/2\ \sinh(t\cdot h)\}$.

terms of $t > 3.5/h$ can be neglected and we have the formula used in the program ELECTRA

$$I = h \sum_{t=-N}^{N} w_t g(x_t) \ , \ h = 3.5/N \qquad (3.43)$$

Table 3.2 shows the comparison of the double exponential and Gauss integration formulas. It is clearly shown that the value obtained by the double exponential formula has much smaller error than that of the value obtained by the Gauss integration formula.

The expression of the electric field is also complex compared with that of the two dimensional problem. The expression is

$$E_r(r,z) = \int_s \frac{\{R^2-r^2+(z-Z)^2\}E(k)-\{(r-R)^2+(z-Z)^2\}K(k)}{2r\{(r+R)^2+(z-Z)^2\}^{1/2}\{(r-R)^2+(z+Z)^2\}} \lambda(R,Z)ds$$

$$E_z(r,z) = \int_s \frac{(z-Z)E(k)}{\{(r+R)^2+(z-Z)^2\}^{1/2}\{(r-R)^2+(z+Z)^2\}} \lambda(R,Z)ds \qquad (3.44)$$

where E(k) is the elliptic integral of the second kind.

$$E(k) = \int_0^{\pi/2} (1-k^2\sin^2\theta)^{1/2} \, d\theta \qquad (3.45)$$

In order to obtain the potential or the electric field, we have to calculate the values of the complete elliptic integrals of the first and second kind. For this, the cord ELECTRA uses approximation functions[3.7]:

$$K(k) = [\ a_0+a_1m_1+ \ldots+a_4m_1^4] + [\ b_0+b_1m_1+ \ldots +b_4m_1^4]\log(1/m_1)$$
$$m_1 = 1-k$$

a_0	= 1.38629436112	b_0	= .5
a_1	= .09666344256	b_1	= .12498593597
a_2	= .03590092383	b_2	= .06880248576
a_3	= .03742563713	b_3	= .03328355346
a_4	= .01451196212	b_4	= .00441787012

(3.46)

$$E(k) = [\ 1+a_1m_1+ \ldots+a_4m_1^4] + [\ 1+b_1m_1+ \ldots +b_4m_1^4]\log(1/m_1)$$

a_1	= .44325141463	b_1	= .24998368310
a_2	= .06269691220	b_2	= .09200180037
a_3	= .04757383546	b_3	= .04069697526
a_4	= .01736506451	b_4	= .00526449639

(3.47)

The errors of both functions are less than 2×10^{-8}.

Table 3.2 Values of A_{11e} calculated by the double exponential (DEF) and the Gauss integration formulas where $P_1=(1,1)$ and $P_2=(1,2)$.

N	DEF	Gauss
4	.438473	.874649
8	.913275	.886299
12	.891366	.888676
16	.890715	.889542
20	.890704	.889952
24	.890704	.890178
28	.890705	.890315
32	.890704	.890405
36	.890704	.890467
40	.890704	.890511
44	.890704	.890544
48	.890705	.890570
52	.890704	.890589
56	.890704	.890605
60	.890705	.890618
64	.890704	.890628

3.3 INTEGRATION OF THE EQUATIONS OF MOTION

The ray tracing is the process to integrate Lorentz's equation of motion step by step.

$$m\frac{d^2\mathbf{r}}{dt^2} = e(\mathbf{E} + \frac{d\mathbf{r}}{dt} \times \mathbf{B}) \qquad (3.48)$$

where t is time, m is the mass of a particle, **r** is the position vector, and **E** and **B** are the electric and magnetic fields, respectively. Because this equation is a system of ordinal differential equations, many types of numerical integration formula can be used to integrate those equations [3.8].

The most famous and widely used method is a forth order Runge-Kutta method. This method can start without any data except initial conditions, and therefore it can be applied to many types of problems with high flexibility. Another well known method is predictor-corrector method. Although the method has a merit that number of the evaluation of the field is lower than that of the Runge-Kutta method, they have a demerit that they need same previous data to calculate a new step; thus they cannot start integration itself and have to use a special start routine. Furthermore when changing the step size of the integration, a restart routine is necessary. Hence we employ the forth order Runge-Kutta method in the program ELECTRA.

Detail of the calculation

For the simplicity of the calculation, we introduce a normalization to the calculation. We introduce new independent parameter 's' instead of t;

$$t = a \cdot s \ , \ a = \sqrt{m/e} \qquad (3.49)$$

And also put e=1 then Eqn.3.48 can be rewritten as

$$d^2\mathbf{r}/ds^2 = \mathbf{E} + 1/a \ d\mathbf{r}/ds \times \mathbf{B} \qquad (3.50)$$

In this case, the electric rigidity R_e and the magnetic rigidity R_m of an ion having mass m and energy $U = 1/2\ m(dr/ds)^2$ are given as

$$R_e = 2U$$

$$R_m = \sqrt{2mU} \qquad (3.51)$$

When we choose the unit of the electric potential as volt, then, unit of the kinetic energy defined by $U= 1/2m(dr/ds)^2$ is 'electron volt'.

Runge-Kutta method

The procedure of the Runge-Kutta method was given elsewhere [3.8]. Thus only a brief description is given here.

First order differential equations can be solved by the Runge-Kutta method; however Eqn.3.48 is a system of second order differential equations. Therefore we rewrite this to a system of first order differential equations as

$$d\mathbf{r}/ds = \mathbf{v}$$

$$d\mathbf{v}/ds = \mathbf{E} + 1/a\ \mathbf{v}\times\mathbf{B} \qquad (3.52)$$

If we define a vector $\mathbf{x}(s)$ and a vector function $\mathbf{f}(\mathbf{x},s)$ as

$$\mathbf{x}(s) = \begin{bmatrix} x \\ y \\ z \\ v_x \\ v_y \\ v_z \end{bmatrix} \qquad \mathbf{f}(\mathbf{x},s) = \begin{bmatrix} v_x \\ v_y \\ v_z \\ [\mathbf{E} + 1/a\ \mathbf{v}\times\mathbf{B}]_x \\ [\mathbf{E} + 1/a\ \mathbf{v}\times\mathbf{B}]_y \\ [\mathbf{E} + 1/a\ \mathbf{v}\times\mathbf{B}]_z \end{bmatrix} \qquad (3.53)$$

Then we have a simple expression of the differential equations as

$$d\mathbf{x}/ds = \mathbf{f}(\mathbf{x},s) \qquad (3.54)$$

Suppose that h is the step size and that $\mathbf{x}_0 = \mathbf{x}(s_0)$ is given. Then the next step $\mathbf{x}(s_0+h)$ is calculated as

$$\mathbf{f}_1 = \mathbf{f}(\mathbf{x}_0,s_0) \qquad \mathbf{x}_1=\mathbf{x}_0 + h/2\ \mathbf{f}_1$$

$$\mathbf{f}_2 = \mathbf{f}(\mathbf{x}_1,s_0+h/2) \qquad \mathbf{x}_2=\mathbf{x}_0 + h/2\ \mathbf{f}_2$$

$$\mathbf{f}_3 = \mathbf{f}(\mathbf{x}_2,s_0+h/2) \qquad \mathbf{x}_3=\mathbf{x}_0 + h\ \mathbf{f}_3$$

$$\mathbf{f}_4 = \mathbf{f}(\mathbf{x}_3,s_0+h)$$

$$\mathbf{x}(s_0+h)=\mathbf{x}_0 + (h/6)(\mathbf{f}_1 + 2\mathbf{f}_2 + 2\mathbf{f}_3 + \mathbf{f}_4) \qquad (3.55)$$

The main term of the local discretization error of the step is proportional to h^5, and the total discretization error is proportional to h^4 [3.8]. Using this relation, we can estimate the errors by varying the step size.

3.4 ROUTINES OF "ELECTRA"

This section describes the SUBROUTINEs of ELECTRA. Type of the variable is double precision real or integer.

Subroutines for Electric field calculation

1. Two dimensional problem

Three subroutines are prepared for the problem.

1.1 RED2(N0,M0)

This routine reads a data set through the logical unit 1 in order to specify the boundary conditions. The data format is as follows:

(four blank lines)

I_1 v_1 x_1 y_1	(I10, F10.0, F10.0, F10.0)
I_2 v_2 x_2 y_2	(I10, F10.0, F10.0, F10.0)
.....	
I_i v_i x_i y_i	(I10, F10.0, F10.0, F10.0)
.....	
I_n v_n x_n y_n	(I10, F10.0, F10.0, F10.0)

(two blank lines)

The shape of the electrodes is specified by the positions (x_i,y_i) and the potentials are given by v_i. The integer I_i is the number of elements interpolated between (x_{i-1},y_{i-1}) and (x_i,y_i). Accordingly I_1 must be '0' or blank. If a specification of an electrode finishes at (x_{i-1},y_{i-1}) and that of another electrode starts (x_i,y_i) then I_i is '0' or blank. An example is given in Fig.3.12.
The output data of this routine are

N0 : the number of nodes.
M0 : the number of elements

1.2 SUBD2(NG, N0, M0)

This subroutine constructs a system of linear equations and solve it. Therefore this routine must be called after RED2.

The input data for this routine are

NG : the order of the gauss integration formula to be used. Usually

from 2 to 10 is preferable.
N0 : the number of nodes.
M0 : the number of elements.

1.3 VED2(X,Y,NG,V,EX,EY)

This routine obtains the potential V and the electric field (EX,EY) at a point (X,Y) by using the charge distribution obtained by SUB2D. After SUBD2 was executed, this routine can be called whenever the values of potentials or electric fields are required.

The input data for this routine are

X,Y : coordinates of the position where the potential and the field are calculated
NG : the order of the Gauss integration. This value is not necessary to be the same value in SUBD2.

The output data of this routine are

V : calculated electric potential
EX : x component of the calculated electric field
EY : y component of the calculated electric field

2. Axially symmetric three-dimensional problem

Three subroutines are prepared for the problem. The data format of the routines are similar to that of the two dimensional problem.

2.1 REDAX(N0,M0)

This routine is similar to RED2(N0,M0). (Replace x to r and y to z)

2.2 SUBAX(NG,N0,M0)

This routine is similar to SUBD2.

2.3 VEAX(R,Z,NG,ER,EZ)

This routine is similar to VED2(X,Y,NG,EX,EY).

3. Three dimensional problem

For the three dimensional calculation, a routine for the mesh generation like RED2 is not prepared, therefore the user should prepare a mesh generation program for a individual problem. The mesh should be specified by using following common blocks.

```
/AXP/ PX(1000), PY(1000), PZ(1000)
/MEL/ MH1(1000), MH2(1000), MH3(1000)
/VQP/ VP(1000), QP(1000)
/NNM/ N0,M0
```

where

PX(I),PY(I),PZ(I) : coordinates of the I-th node
MH1(J),MH2(J),MH3(J): node numbers consisting J-th element.
For example, if the J-th element consists of i-, j-, k-th node, then MH1(J)=i, MH2(J)=j, MH3(J)=k.
VP(I): value of the potential applied to the I-th node
N0 : the number of the nodes
M0 : the number of the elements

3.2 SUBD3(NG,N0,M0)

This subroutine constructs the system of linear equations and solve it. Therefore this routine must be called after the data of the common blocks are prepared.

The input data for this routine are

NG : the points of the gauss integration formula to be used. Usually from 2 to 10 is preferable.
N0 : the number of nodes.
M0 : the number of elements.

3.3 VED3(X,Y,Z,NG,V,EX,EY,EZ)

This routine obtains the potential and the electric field.

Input data for this routine are

X, Y, Z: the components of the position of the point where the fields are calculated
NG: the order of the gauss integration

Output data of this routine are

V: calculated potential
EX,EY,EZ: the components of the calculated electric field.

4. Routines for ray tracing

Two subroutines were prepared for the ray tracing. The ray tracing routines are independent of other routines of ELECTRA.

The electric field or magnetic field must be specified by using subroutines prepared by the user. Further, a function NRANGE must be used for limiting the calculation range of the space.

4.1 RK2D(XS,YS,AS,US,CS,D,XP,YP,N,NMAX)

This routine calculates ion trajectories in two dimensional space. If there is no magnetic field, this ray tracing routine can also be applied to the axially symmetric three dimensional problems.

Input data for this routine are

XS,YS : coordinates of the initial position of the ion.
AS: angle between direction of the initial motion and x axis (in radian).
US: initial kinetic energy (in electron volt).
CS: mass of the ion. This value can be calculated by using magnetic rigidity (see Eqn.2.51)
D: step size of the integration in length.
NMAX: maximum number of integration step. Calculation will stop when the step number reaches this value.

Output data of this routine

XP(I),YP(I): coordinates of the ion trajectory (I=1,2,...,N)
The dimension of these arrays must be NMAX.
N: number of computed steps.

Field specification

The following routines and a function must be prepared by the user to define the fields.

```
SUBROUTINE  EFILD2(X,Y,EX,EY)
SUBROUTINE  BFILD2(X,Y,BZ)
FUNCTION    NRANGE(X,Y)
```

where

X,Y: coordinates of the position where the potential and field are specified.
EX,EY : components of the electric field
BZ : z component of the magnetic field

NRANGE : if the point (X,Y) is out of range, NRANGE = -1, otherwise
NRANGE = 1

4.2 RK3D(XS,YS,ZS,PX,PY,PZ,AS,US,CS,D,XP,YP,ZP,N,NMAX)

This routine calculates ion trajectories in three dimensional space.

Input data for this routine are

XS,YS,ZS : coordinates of the initial position
PX,PY,PZ : components of direction of the initial motion. Only the ratio is meaningful.
US: initial kinetic energy.
CS: mass of the ion. This value can be calculated by using magnetic rigidity (see Eqn. 2.51)
D: step size of the integration in length.
NMAX: maximum number of integration steps. Calculation will stop when the step number reaches this value.

Output data of the routine

XP(I),YP(I),ZP(I): coordinates of the trajectory (I=1,2,..,N)
N: number of the computed steps

Field specification

The following routines and a function must be prepared by the user to define the fields.

```
SUBROUTINE  EFILD3(X,Y,Z,EX,EY,EZ)
SUBROUTINE  BFILD3(X,Y,Z,BX,BY,BZ)
FUNCTION    NRANGE(X,Y,Z)
```

where

X, Y, Z : coordinates of the point
EX,EY,EZ : components of the electric field
BX,BY,BZ : z component of the magnetic field
NRANGE : if the point (X,Y,Z) is out of range, NRANGE = -1, otherwise
NRANGE = 1

(a)

sample data for RED2

```
        10.      2.0      9.0      ..... point a
3       10.      5.0      6.0
6       10.     11.0      6.0
       -10.      2.0      3.0      ..... point d
6      -10.      5.0      3.0
3      -10.      8.0      3.0
2      -10.     11.0      3.0      ..... point g
```

(b)

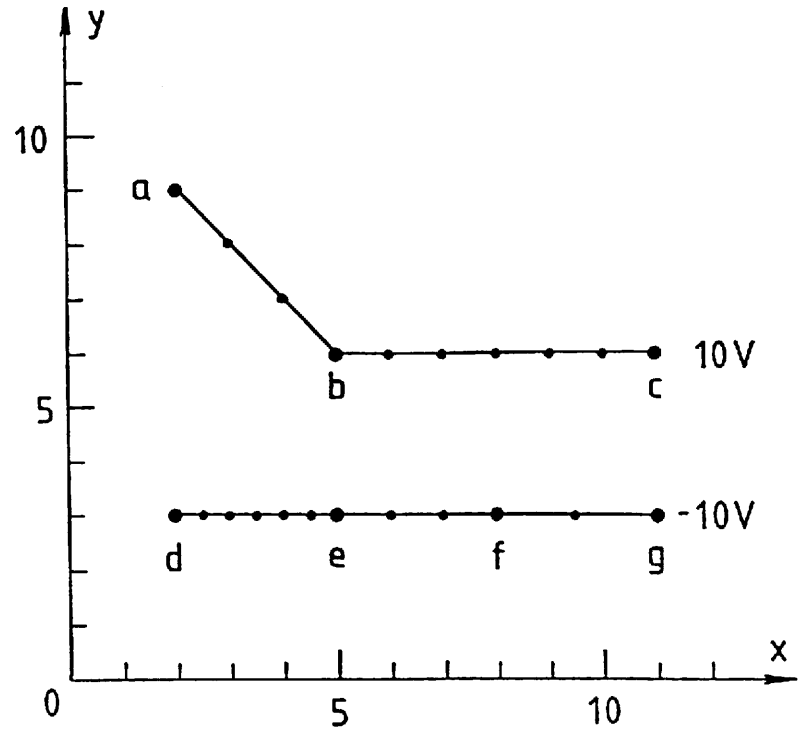

Fig. 3.12. Example and description of the data for RED2.

REFERENCES

[3.1] T. Kohno and T. Takuma, Numerical Calculation Method of Electric Field, Corona, Tokyo, 1980 (in Japanese).

[3.2] R.F. Harrington, Proc. IEEE, 55 (1967) 136.

[3.3] E. Harting and F.H. Read, Electrostatic Lenses, Elsevier, Amsterdam, 1976.

[3.4] C.A. Brebbia, The Boundary Element Method for Engineers, Pentech Press, London,1978.

[3.5] P.J. Davis, Methods of Numerical Integration, Academic Press, New York, 1975.

[3.6] M. Mori, Kyokusen to Kyokumen, Kyoiku Shuppan, Tokyo, 1974 (in Japanese).

[3.7] M. Abramowitz and I.A. Stegun, Handbook of Mathematical Functions, Dover, New York, 1970, p587.

[3.8] P. Henrici, Discrete Variable Methods in Ordinary Differential Equations, John Wiley and Sons, New York, 1968.

4. EXAMPLES OF APPLICATION OF "ELECTRA" TO FRINGING FIELD CALCULATIONS

4.1 FRINGING FIELDS OF QUADRUPOLE LENS

4.1.1 INTRODUCTION

An electrostatic quadrupole lens is recently utilized as an effective focusing element for mass spectrometers. For example, a quadrupole doublet is applied to zoom the mass range on the simultaneous detector [4.1.1]. It is important to know the ion optical effects of a quadrupole lens to design such instruments. The transfer matrices of the main and fringing fields of a quadrupole lens have been calculated up to third-order [4.1.2],[4.1.3]. The matrix elements of the fringing field depend on the fringing field distribution. Thus, in order to estimate those matrix elements, we must know the real fringing field distribution in advance. It is impossible to obtain an analytical expression of the fringing field and therefore either an experimental measurement or a numerical calculation is indispensable. For a magnetic quadrupole lens, it is possible to measure the fringing field distribution experimentally. The field distribution prepared in the program TRIO was obtained by the method. For an electrostatic quadrupole lens, it is very difficult to measure a fringing field distribution by an experimental method. Thus the numerical calculation was necessary. For this purpose, we solved three dimensional Laplace's equation using the program ELECTRA described in chapter 3 and determined the fringing field distribution.

4.1.2 DEFINITE INTEGRALS

Figure 4.1.1 shows the geometry and coordinate system to be studied. Four cylindrical electrodes of radius a_0 and length L_0 are positioned at a distance r_0 from the central axis z. Two thin shield plates with aperture of radius (b) are positioned at distance (d) from the electrodes, respectively. The origin of z axis is chosen on the ideal field boundary, and (h) is the distance from the ideal field boundary to the electrodes. The lens is shielded by a cylinder of radius $4r_0$. In the main region of an electrostatic quadrupole lens of fourfold symmetry, the electric potential V(x,y,z) is independent of z and is assumed to be

$$V(x,y,z) = -k_0/2\ (x^2-y^2) + (\text{sixth order term}) + \ldots\ldots \quad (4.1.1)$$

where k_0 is a field gradient constant. In the fringing region, the potential depends on z as

$$V(x,y,z) = -k(z)/2\ (x^2-y^2) - k''(z)/24(x^4-y^4) + \ldots\ldots \quad (4.1.2)$$

where k(z) is a function of z. Differentiating Eqn.4.1.2 gives a definition of k(z) as

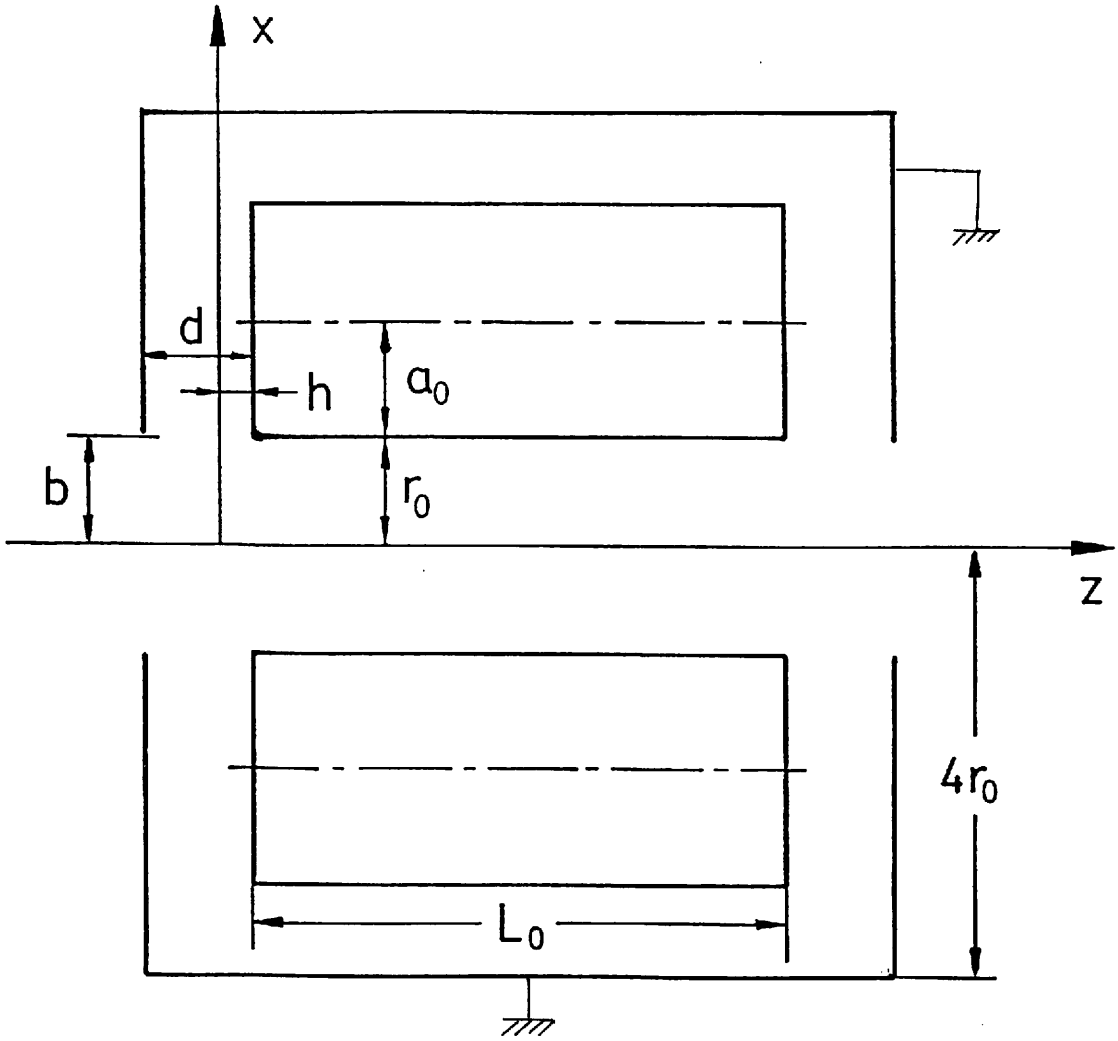

Fig. 4.1.1. Schematic drawing of an electrostatic quadrupole lens.

$$k(z) = - \partial^2 V(0,0,z)/\partial x^2 \qquad (4.1.3)$$

The position of the ideal field boundary z^* is defined [4.1.3] as

$$k_0(z_b - z^*) = \int_{z_a}^{z_b} k(z)dz \qquad (4.1.4)$$

where z_a is the position where $k(z)=0$ and z_b is the position where $k(z)=k_0$. We choose the origin of the z axis so that $z^*=0$. The definition of the definite integrals which is necessary in the third-order matrix elements is as follows [4.1.3].

$$I_1 = k_0^{-1} \int_{z_a}^{z_b} \int_{z_a}^{z} k(z)dzdz - 1/2z_b^2$$

$$I_2 = k_0^{-1} \int_{z_a}^{z_b} z[\int_{z_a}^{z} k(z)dz]dz - 1/3z_b^3$$

$$I_3 = k_0^{-2} \int_{z_a}^{z_b} [\int_{z_a}^{z} k(z)dz]^2 dz - 1/3z_b^3$$

$$I_4 = k_0^{-2} \int_{z_a}^{z_b} k(z)^2 dz - z_b \qquad (4.1.5)$$

These integrals are defined so that the values are independent of z_a and z_b.

4.1.3 CALCULATION METHOD

Field calculation method

The field calculation can be performed by the program ELECTRA. The quadrupole lens field studied here has the following symmetries and a anti-symmetry:

$$\begin{aligned} V(x,y,z) &= V(-x,y,z) \\ V(x,y,z) &= V(x,-y,z) \\ V(x,y,z-z_0) &= V(x,y,-z+z_0) \\ V(x,y,z) &= -V(y,x,z) \end{aligned} \qquad (4.1.6)$$

where z_0 is the z coordinate of the center point of the lens. The charge distribution should have the same symmetries. Taking account of those four symmetries, we can reduce the number of charges by a factor of $(1/2)^4$ and can also reduce the dimension of the system of linear equations by a factor of $(1/2)^8$.

In order to calculate the definite integrals I_1, I_2, I_3, I_4 in Eqn.4.1.5 we have to obtain the function k(z) defined by Eqn 4.1.3. In ordinal method such as finite element method the values of k(z) are obtained by numerically differentiating the potentials at each mesh point. This differentiation is a major source of inaccuracy of the calculation. In

the charge density method, however, k(z) can be obtained directly from the charges by using following equation:

$$k(z)= \int \frac{\partial^2}{\partial x^2}\left(\frac{\sigma(\mathbf{R})}{|\mathbf{r}-\mathbf{R}|} \right) ds \qquad (4.1.7)$$

where $\mathbf{r}=(x,y,z)$ and $\sigma(\mathbf{R})$ is the charge distribution on the lens electrodes.

Calculation of the definite integrals

In the previous section the procedure to obtain the values of k(z) for a finite number of points is discussed, our next step is to calculate the definite integrals using the finite values. In order to calculate the integrals we have to interpolate the calculated values of k(z). A cubic spline function [4.1.6] is applied for the interpolation. The definition of the spline function is as follows: Supposing that sampling points z_i and data $k_i=k(z_i)$ (i=1,2,...,m) are given, then the spline function K(z) is expressed as

$$K(z) = \sum_{i=1}^{m-1} K_i(z) \qquad (4.1.8)$$

where $K_i(z)$ is a third order polynomial defined as

$$K_i(z) = a_i + b_i(z-z_i) + c_i(z-z_i)^2 + d_i(z-z_i)^3 \quad (\text{for } z_i \le z \le z_{i+1})$$

$$= 0 \qquad (\text{for } z < z_i \text{ or } z > z_{i+1}) \qquad (4.1.9)$$

The coefficients a_i, b_i, c_i, d_i are determined from the data set (k_i,z_i) so that $K_i(z)$ satisfy the following equations

$$K_i(z_i) = k_i \qquad (4.1.10)$$
$$K_i(z_{i+1}) = k_{i+1} \qquad (4.1.11)$$
$$K'_i(z_i) = K'_{i-1}(z_i) \qquad (4.1.12)$$
$$K''_i(z_i) = K''_{i-1}(z_i) \qquad (4.1.13)$$

Above conditions introduce 4(m-1)-2 relations among 4(m-1) coeficients, because Eqns. 4.1.12 and 4.1.13 are not defined at i=1. Two additional conditions are, therefore, necessary to determine the parameters uniquely. We introduce following two conditions

$$K''_1(z_1) = 0$$
$$K''_{m-1}(z_m) = 0 \qquad (4.1.14)$$

Once the coefficients of the function $K_i(z)$ is determined, we can integrate K(z) easily, because the function is expressed by simple polynomials.

By using the spline function technique the double integral I_1 is calculated as follows:

First the values of $k(z_i)$ are calculated then we determine the spline function K(z) interpolating those values. Second the values of the definite integrals H_i (i=1,2,..,m) is obtained by integrating the spline function K(z).

$$H_i = \int_{z_1}^{z_i} K(z)dz \qquad (4.1.15)$$

Another spline function H(z) interpolating the values of (z_i,H_i) is then determined. Finally integrating H(z) gives the value of the definite integrals I_1 as

$$I_1 = \int_{z_1}^{z_m} H(z)dz - 1/2z_m^2 \qquad (4.1.16)$$

Other definite integrations I_2,I_3,I_4 also can be calculated using spline function technique.

4.1.4 RESULTS AND CONCLUSION

A special routine which generates the mesh of a quadrupole lens for ELECTRA was newly developed. An example of the generated mesh of 1/16 region of the lens is shown in Fig 4.1.2. The number of the system of a linear equations is 219 and that of elements of whole lens electrodes is 363x16. When the number of sampling points of Gauss integration was 7x7 and the number of sampling points for field distribution was 200, typical computing time is 12 minutes with an IBM 3090-150E computer. Figure 4.1.3 shows the calculated fringing field distribution k(z) in the case of $b=r_0$ and $d=r_0$. The values of the definite integrals which are necessary to estimate the transfer matrices for various lens structures are given in table 4.1.2 where the values of b and d are varied from $0.25r_0$ to $1.25r_0$ and from $0.25r_0$ to $2.0r_0$, respectively.

The values of the definite integrals of a fringing field of quadrupole lenses were calculated by ELECTRA. Until this study, those values were only obtained by experimental methods, because the three dimensional calculations were very difficult. In this study, we can demonstrate that the program ELECTRA can execute those three-dimensional calculations.

REFERENCES

[4.1.1] M. Ishihara and Y. Kammei, Rapid Commun. Mass Spectrm.,3 (1989) 420.
[4.1.2] Y. Fujita and H. Matsuda, Nucl. Instr. Meth., 123 (1975) 495.
[4.1.3] H. Matsuda and H. Wollnik, Nucl. Instr. Meth., 103 (1972) 117.
[4.1.4] R.F. Harrington, Proc. IEEE, 55 (1967) 136.
[4.1.5] T. Mulvey and M.J. Wallington, Rep. Prog. Phys., 36 (1973) 347.
[4.1.6] P.J. Davis, Methods of Numerical Integration, Academic Press, New York, 1975.

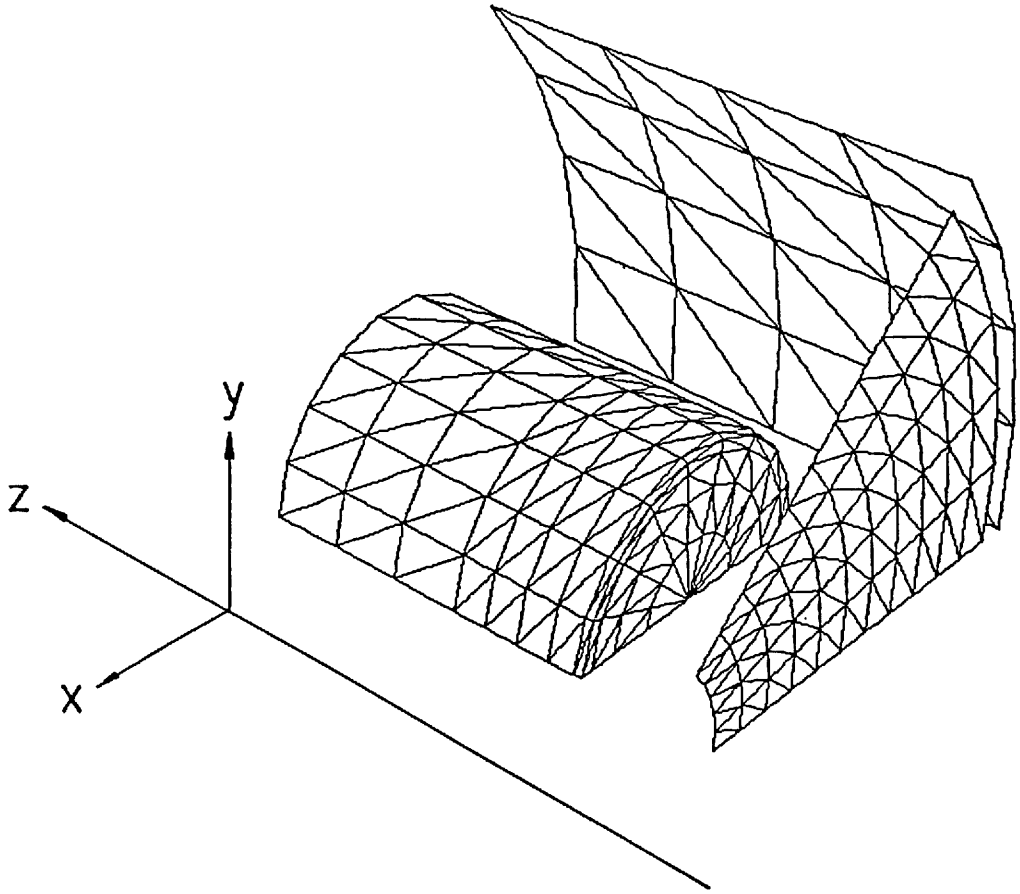

Fig. 4.1.2. Three dimensional mesh of 1/16 region of the quadrupole lens.

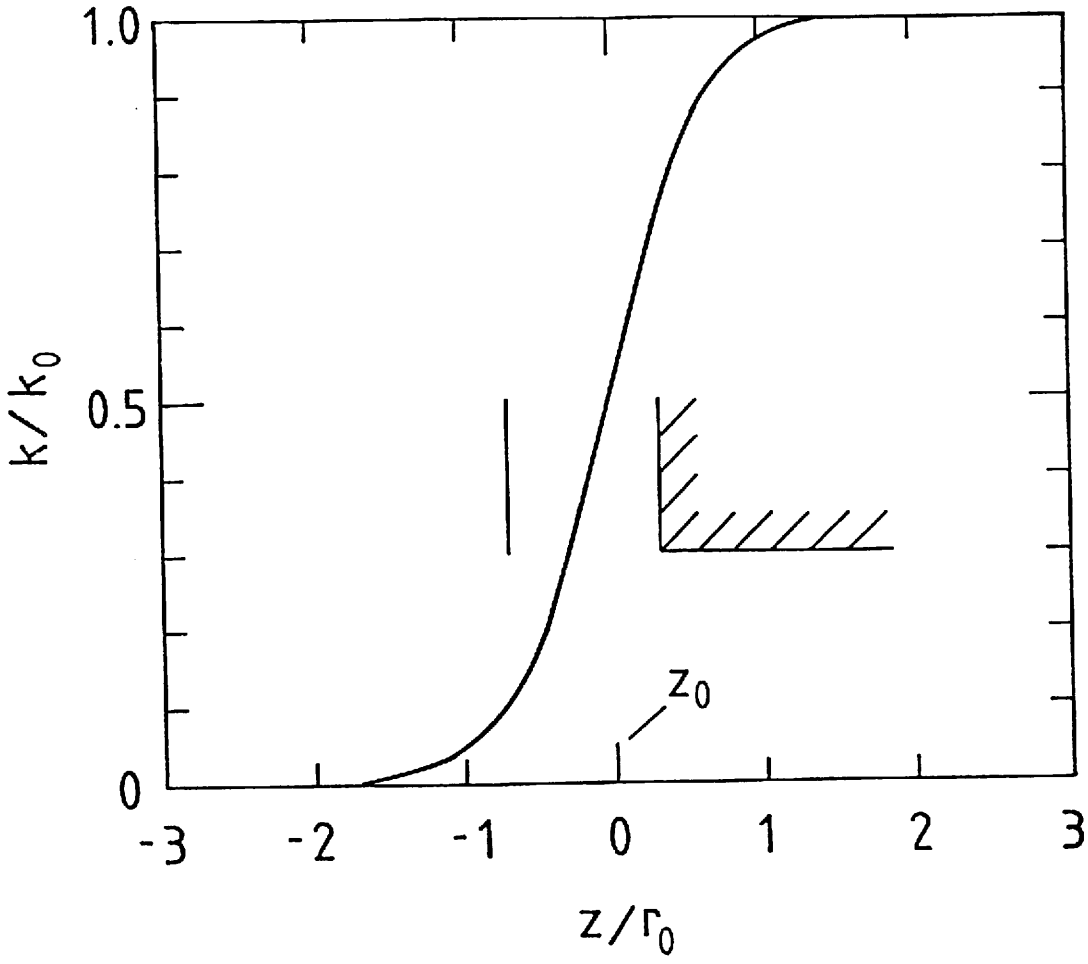

Fig. 4.1.3. A calculated field distribution k(z) for $b=d=r_0$.

Table 4.1.1. Calculated values of definite integrals of fringing fields for quadrupole lenses.

b	d	h	I_1	I_2	I_3	I_4
0.25	0.25	-0.100	0.049	0.005	0.017	-0.170
	0.50	0.073	0.063	0.006	0.024	-0.196
	0.75	0.199	0.085	0.006	0.033	-0.231
	1.00	0.286	0.110	0.005	0.044	-0.266
	1.50	0.390	0.162	-0.004	0.064	-0.321
	2.00	0.443	0.206	-0.022	0.080	-0.357
0.50	0.25	-0.072	0.057	0.004	0.020	-0.186
	0.50	0.091	0.070	0.005	0.026	-0.208
	0.75	0.209	0.089	0.006	0.034	-0.237
	1.00	0.292	0.113	0.005	0.045	-0.269
	1.50	0.393	0.162	-0.004	0.065	-0.321
	2.00	0.443	0.203	-0.019	0.080	-0.356
0.75	0.25	-0.028	0.069	0.004	0.024	-0.206
	0.50	0.117	0.079	0.005	0.029	-0.223
	0.75	0.219	0.095	0.005	0.036	-0.245
	1.00	0.293	0.115	0.004	0.045	-0.271
	1.50	0.384	0.156	-0.002	0.063	-0.316
	2.00	0.433	0.191	-0.013	0.076	-0.348
1.0	0.25	0.068	0.089	0.003	0.031	-0.236
	0.50	0.167	0.097	0.003	0.035	-0.247
	0.75	0.253	0.110	0.003	0.042	-0.264
	1.00	0.313	0.127	0.002	0.049	-0.284
	1.50	0.393	0.163	-0.004	0.065	-0.323
	2.00	0.437	0.196	-0.015	0.078	-0.351

4.2 HIGHER ORDER ABERRATIONS IN THE FRINGING FIELD OF AN ELECTROSTATIC ANALYZER

4.2.1 INTRODUCTION

The fringing field of an electrostatic analyzer (ESA) strongly affects the image aberration of a high resolution mass spectrometer. The ion optical effects of the fringing field of an ESA were calculated by Wollnik [4.2.1] up to a second-order approximation and by Matsuda [4.2.2] up to a third-order approximation. They calculated the ion trajectories analytically by a successive approximation. All ion optical effects are reduced to a matrix transformation at the ideal field boundary. The matrix elements are represented by functions of the few fringing field integrals. The values of those integrals were calculated for various electrode structures [4.2.3].

Complete calculations for the third-order ion optics including the influences of the fringing fields of an ESA have made it possible to design a high performance mass spectrometer. However, the effect of the aberrations higher than third-order were still unknown. Therefore we calculated the effects of the fringing field of an ESA using higher than third-order approximation. We studied the case where the structure of an ESA was a parallel condenser and only the geometrical aberration in the radial plane was estimated. It is, however, very complex to use the successive approximation method for this purpose. Thus we calculated the ion trajectories through the fringing field by a ray tracing method using the program ELECTRA and estimated the effects up to seventh-order. Furthermore we found that one of the fifth-order matrix elements can be estimated from a fringing field integral. Using those results, we simulated the peak broadening of a mass spectrometer caused by the fifth-order effect.

4.2.2 COORDINATE SYSTEM AND GEOMETRY

The coordinate system (x,z) and the structure of the electrodes to be studied are shown in Fig.4.2.1. The thickness of the shield plate is assumed to be small compared with the slit width (2b) of the shield plate, the distance (2k) between the parallel condenser electrodes and the spacing (d) between the shield plate and the condenser electrodes.

Figure 4.2.2 shows the real field distribution E(z) and the ideal field distribution along the z axis. The ideal field boundary z_0 is defined as [4.2.1][4.2.2]

$$\int_{z_b}^{z_a} E(z)\, dz = \int_{z_b}^{z_a} E_0\, dz = E_0\,(z_b - z_0) \qquad (4.2.1)$$

where $E_0 = -V/k$, z_a is a point in the field free region, z_b is a point in the homogeneous part of the parallel condenser and V is the electric potential applied to the electrode. The curvature radius R_0 of the main path at the ideal field boundary is given by

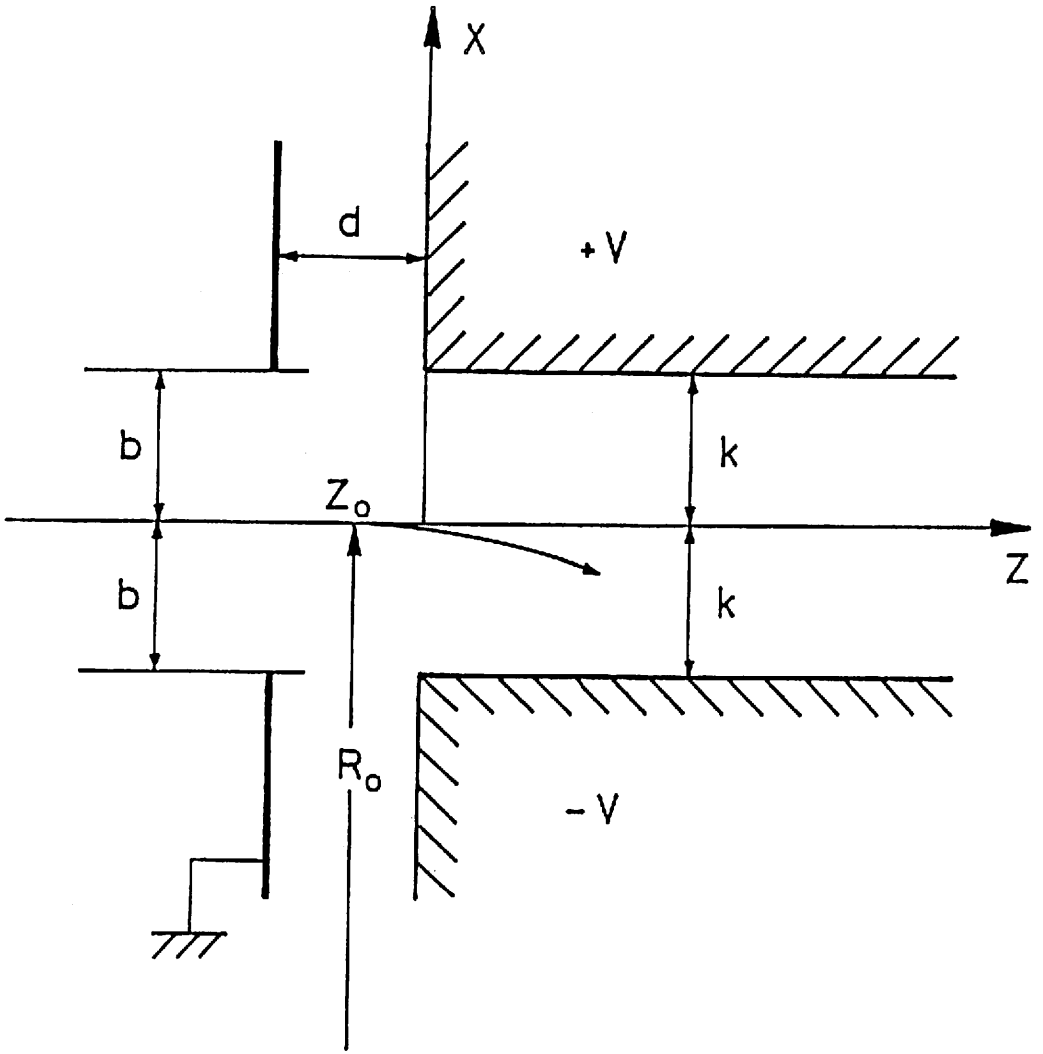

Fig.4.2.1. Structure of the electrodes and coordinate systems in an entrance fringing field of an electrostatic analyzer.

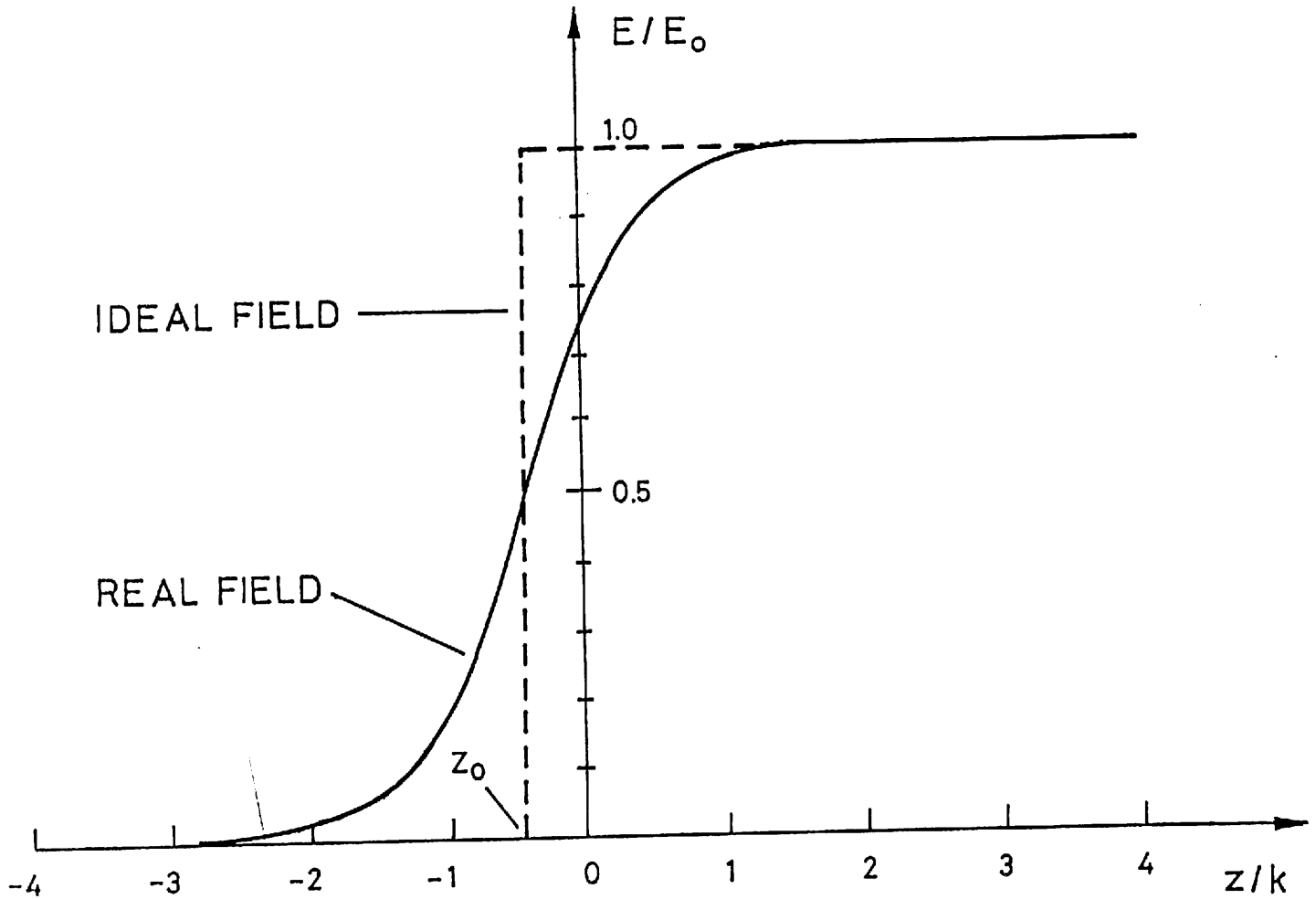

Fig.4.2.2. Real and ideal field distribution of a fringing field of an ESA.

$$R_0 = -2U_0 /(eE_0) \qquad (4.2.2)$$

where e and U_0 are the charge and the energy of the ion, respectively. Usually R_0 is large compared with the distance k : in this paper R_0 = 100k.

4.2.3 ION TRAJECTORY AND MATRIX FORMATION

Figure 4.2.3 shows the real trajectory and the ideal trajectory [4.2.1][4.2.2]. The real trajectory is deflected by the real field and the ideal trajectory is deflected by the ideal field. The ideal trajectory has a break at the ideal field boundary so that it coincides with the real trajectory both in the field free region and in the homogeneous part of the condenser. The effect of the fringing field is reduced to a matrix transformation as follows:

$$x_2 = (x|x)x_1 + (x|\alpha)\tan\alpha_1 + (x|x^2)x_1^2 + (x|x\alpha)x_1 \tan\alpha_1 + (x|\alpha^2)\tan^2\alpha_1 + \ldots\ldots \qquad (4.2.3)$$

$$\tan\alpha_2 = (\alpha|x)x_1 + (\alpha|\alpha)\tan\alpha_1 + (\alpha|x^2)x_1^2 + (\alpha|x\alpha)x_1 \tan\alpha_1 + (\alpha|\alpha^2)\tan^2\alpha_1 + \ldots\ldots \qquad (4.2.4)$$

where x_1 and α_1 are the displacement and the inclination angle from the optical axis respectively at the entrance side of the ideal field boundary, x_2 and α_2 are at the exit side and $(x|x),(x|\alpha),\ldots$ are the transfer matrix elements of the fringing field. Here we study only the matrix elements related to x and α. If we know the real field distribution, we can calculate those matrix elements up to third-order. For example $(\alpha|x^3)$ is given by [4.2.2]

$$(\alpha|x^3)R_0^2 = -4/3I_5 \qquad (4.2.5)$$

where

$$I_5 = E_0^{-2} \int_{z_a}^{z_b} E'(z)\, dz$$

It is possible to approximate the predominant effect of the fringing field to a thin lens, because the range of the fringing field is relatively narrow compared with that of the homogeneous pert. In this approximation, the lens action $\Delta(\tan\alpha) = \tan\alpha_2 - \tan\alpha_1$ only depends on x_1 and does not dependent on α_1; thus we can put $\alpha_1 = 0$ in this study. Then Eqn.4.2.4 can be reduced to

$$\tan\alpha_2 = (\alpha|x)x_1 + (\alpha|x^2)x_1^2 + (\alpha|x^3)x_1^3 + (\alpha|x^4)x_1^4 + (\alpha|x^5)x_1^5 + (\alpha|x^6)x_1^6 + (\alpha|x^7)x_1^7 \qquad (4.2.6)$$

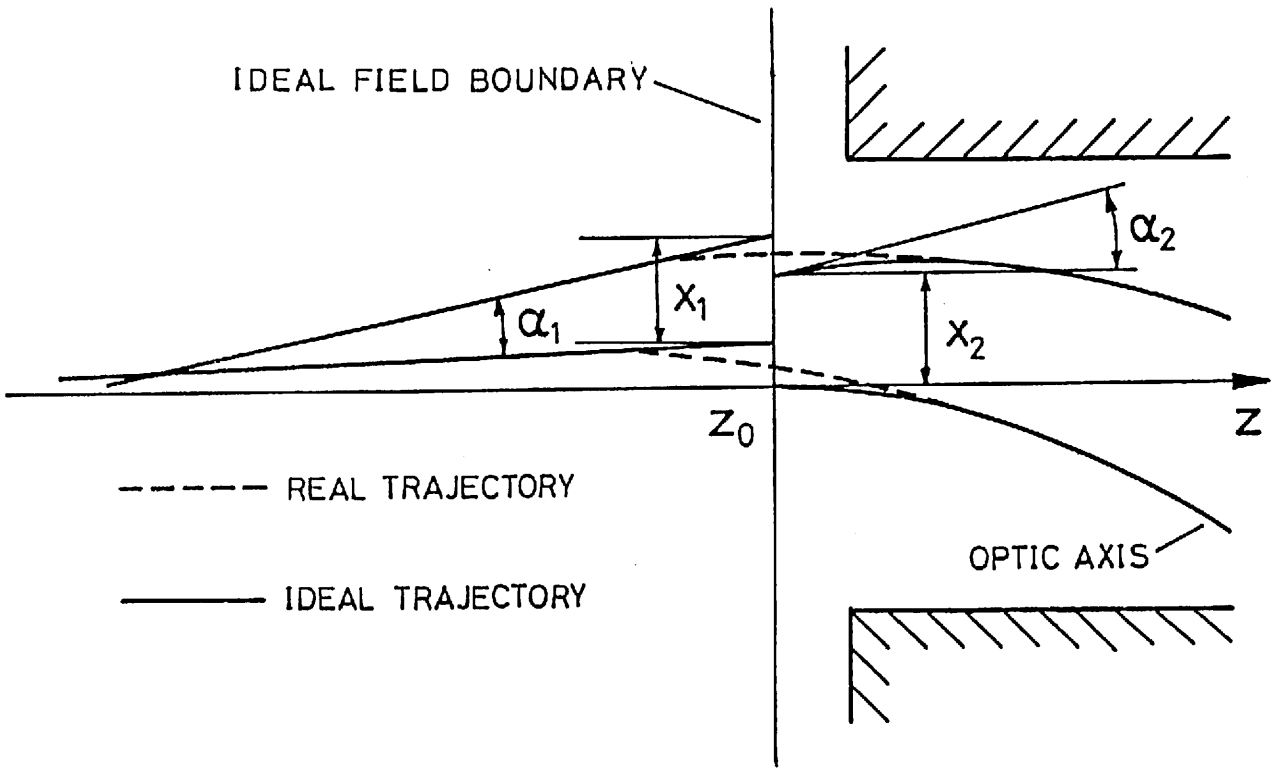

Fig.4.2.3. Real and Ideal ion trajectories in the fringing field of an ESA. The angles α_1, α_2 and the distances x_1, x_2 are defined.

If a real trajectory is calculated by a ray tracing method, the ideal trajectory can be expressed analytically from the calculated trajectory. Then the values of $\tan\alpha_2$ are obtained as a function of x_1 and the transfer matrix elements can be obtained by fitting those values to Eqn.4.2.6.

4.2.4 NUMERICAL CALCULATION METHOD

For numerical calculation of the trajectories, the program ELECTRA described in chapter 3 was adopted. Figure 4.2.4 shows an example of the calculated potential distribution for b=d=k; where the surface of the electrodes was divided into 450 linear elements in this calculation. It is shown that the potential distributes nonlinearly in the fringing region; this causes higher order aberrations.

For integrating the equations of motion, a fourth-order Runge-Kutta method was used. The integration was done from z_a = -5k, where $E_x/E_0 < 10^{-3}$, to z_b = 5k, where $(E_0 - E_x)/E_0 < 10^{-4}$. The interval of each step of the integration was about 0.1k. The initial condition x_1 was varied from -0.5k to 0.5k by 0.05k step.

The calculated value of $\tan\alpha_2$ were fitted to a seventh-order polynomial of x_1 by using a least squares method to obtain the values of the coefficients. Since the accuracy of these values depends on the choice of the order of the polynomial, it is important to determine the order. In general, the accuracy increases as the order of the polynomial increases. However it is expected that those terms of Eqn.4.2.6 which are higher than a certain order are smaller than the numerical inaccuracy of $\tan\alpha_2$. In this case the highest accuracy is obtained when the polynomial of this order is used. In order to determine this order, we used a difference table of $\tan\alpha_2$. For all cases in this study, the sixth difference of $\tan\alpha_2$ was approximately a liner function of x_1, and the eighth difference of $\tan\alpha_2$ was a random function of x_1. This indicates that $\tan\alpha_2$ can be well approximated by a seventh order polynomial of x_1. Thus we used a seventh-order polynomial to obtain the matrix elements. We used, in addition, a ninth-order polynomial to estimate the effects of the order of the polynomial.

In order to calculate the fringing field integral such as I_5 included in Eqn.4.2.5, it is required to integrate and differentiate the function E(z) numerically; for this, a spline function technique [4.2.6] was used. To reduce the round error, all calculations in this study were performed in double precision; this was essential to this study.

4.2.5 RESULTS AND DISCUSSION

Matrix elements

Figure 4.2.5 gives the values of $|(\alpha|x^i)(k/2)^i|$ (i = 3,4,5,7) for d/k = 0.5 to 2.0 where b=k and Ro = 100k. The dimensionless value $|(\alpha|x^i)(k/2)^i|$ indicates the i_{th}-order effect for $x_1 = \pm$ k/2. The sixth-order effect can be neglected, because it was smaller than the calculation error. It can be seen that the fifth-order effect is most serious in the effects higher than third-order effects and other effects are sufficiently smaller than the third-order effect. The ratio $|(\alpha|x^5)(k/2)^5| : |(\alpha|x^3)(k/2)^3|$ increases with decreasing value of

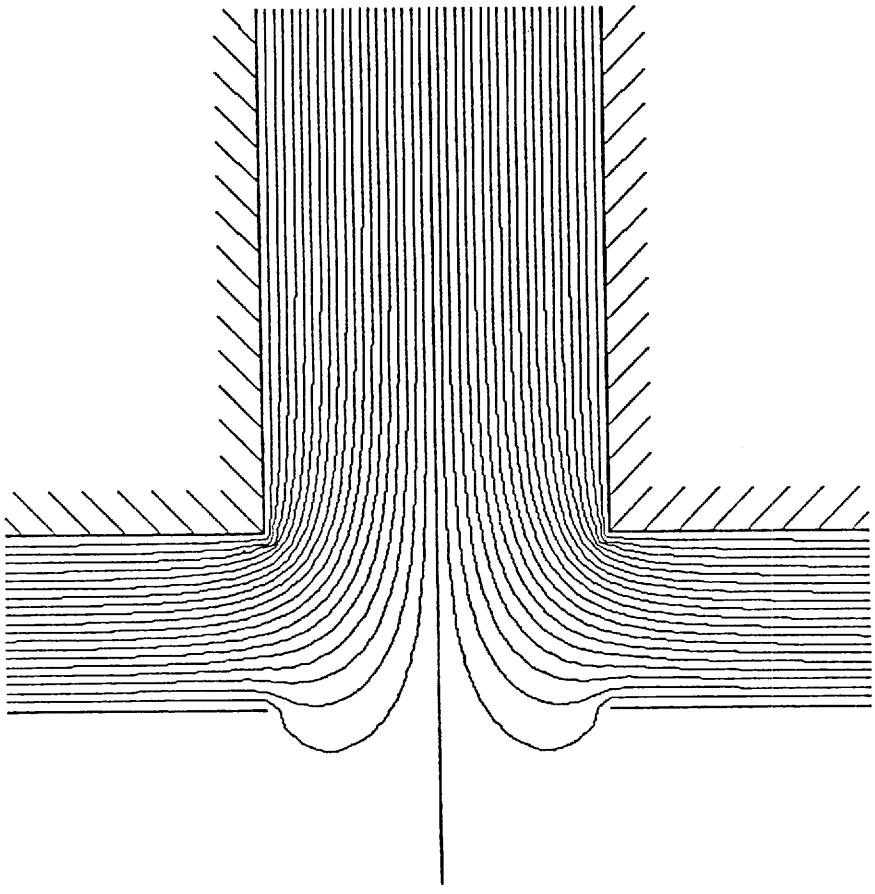

Fig.4.2.4. Plot of 5% equipotential of the fringing field for d=b=k calculated by ELECTRA. The surface of the electrodes are divided into about 450 linear elements in this calculation.

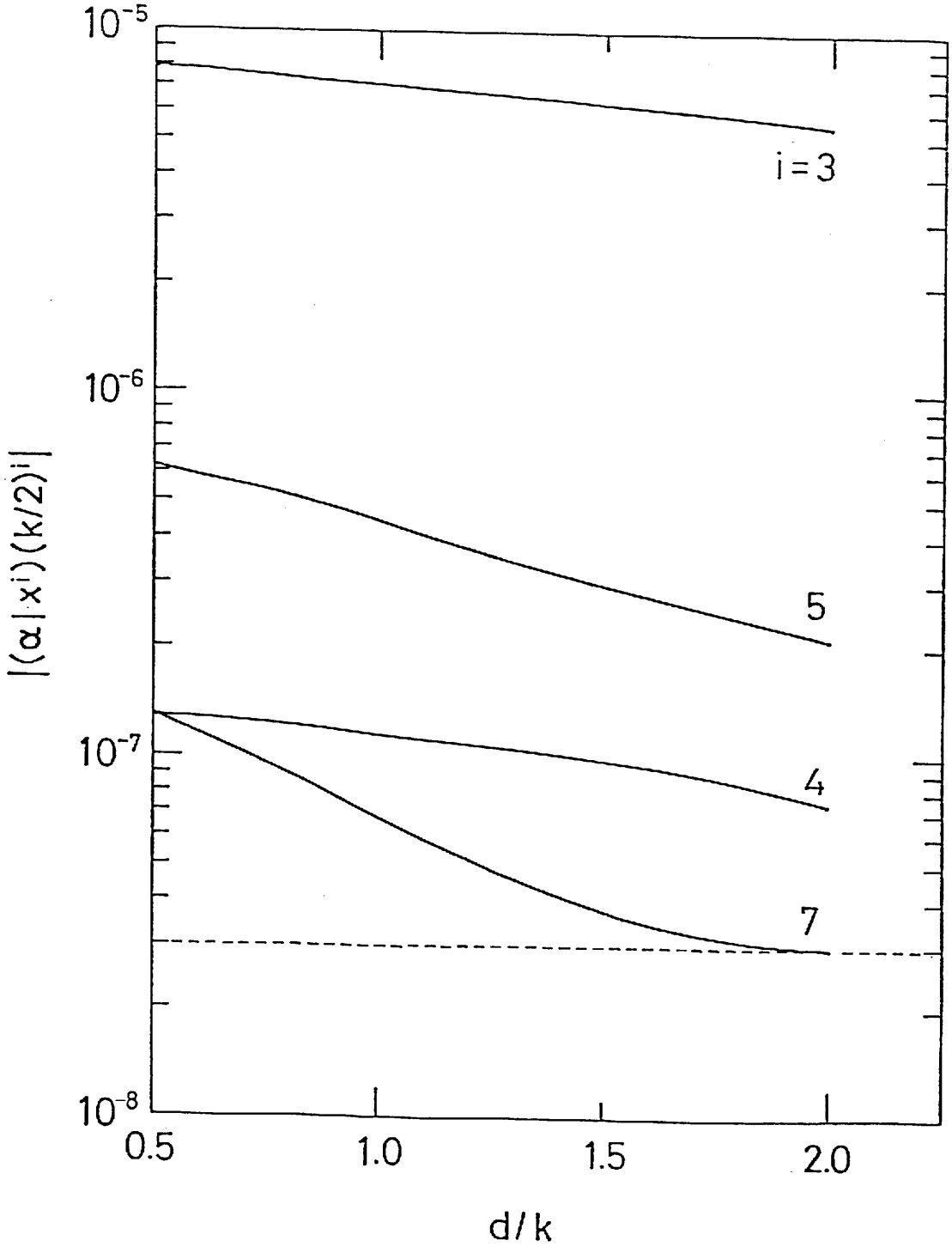

Fig.4.2.5. Higher order effects of the fringing field as a function of d/k, where b=k. The broken line indicates resulted calculation error.

d/k. This indicates that the fifth-order effect is important when the range of the fringing field is narrower.

In order to estimate the reliability of the ray tracing method, the value of $(\alpha|x^3)$ calculated by this method was compared with those calculated from Eqn.4.2.5. The disagreement between two methods is less than 0.4%. Accordingly we can estimate that the calculated values of $(\alpha|x^3)$ have inaccuracies about 0.4% or less. In other words, the values of $|(\alpha|x^3)(k/2)^3|$, which are about 7×10^{-6}, have the error of 3×10^{-8} or less . Furthermore it is expected that the values of $|(\alpha|x^i)(k/2)^i|$ have the error of around 3×10^{-8}. The effects of the order of the polynomial which was used to obtain the matrix elements were not larger than this expected error. This was estimated by using a ninth-order polynomial in place of the seventh-order polynomial.

Fifth-order matrix element

On the analogy of Eqn.4.2.5, we found that the matrix element $(\alpha|x^5)$ is given by

$$(\alpha|x^5)R_0^2 = cI_9 \qquad (4.2.9)$$

where

$$c = -0.25 \pm 0.01$$

$$I_9 = E_0^{-2} \int_{z_a}^{z_b} E''^2(z)\, dz$$

The constant c is obtained by fitting the values of $(\alpha|x^5)$ and I_9 to Eqn.4.2.9 using a least squares method (see Fig.4.2.6). The values of I_5 and I_9 for typical electrode structures are given in table 4.2.1.

4.2.6 CONCLUSION

The program ELECTRA was adopted for precise calculations of the ion optical effects of the fringing field of an ESA and the matrix elements up to seventh-order were estimated. The third-order matrix elements obtained by the ray tracing method were in good agreement with those obtained by the analytical calculation. It was found that a fifth-order fringing field effect is most significant of the effects higher than third order. The fifth-order matrix element is simply given by Eqn.4.2.9.

REFERENCES

[4.2.1] H. Wollnik, Nucl. Instrum. Meth., 52 (1967) 250.
[4.2.2] H. Matsuda, Nucl. Instrum. Meth., 91 (1971) 637.
[4.2.3] Z.H. Hu, T.Matsuo and H.Matsuda, Int. J. Mass Spectrom. Ion Phys., 42 (1982) 145.

[4.2.4] T. Mulvey and M.J. Wallington, Rep. Prog. Phys., 36 (1973) 347.

[4.2.5] T. Kohno, T. Takuma, Numerical Calculation Method of Electric Field, Corona Publishing Co., Tokyo Japan (1980)[in Japanese].

[4.2.6] P.J. Davis and P. Rabinowitz, Methods of Numerical integration, Academic Press Inc., (1975).

[4.2.7] T. Matsuo, H. Matsuda, Y. Fujita and H. Wollnik, Mass Spectrosc., 24 (1976) 19.

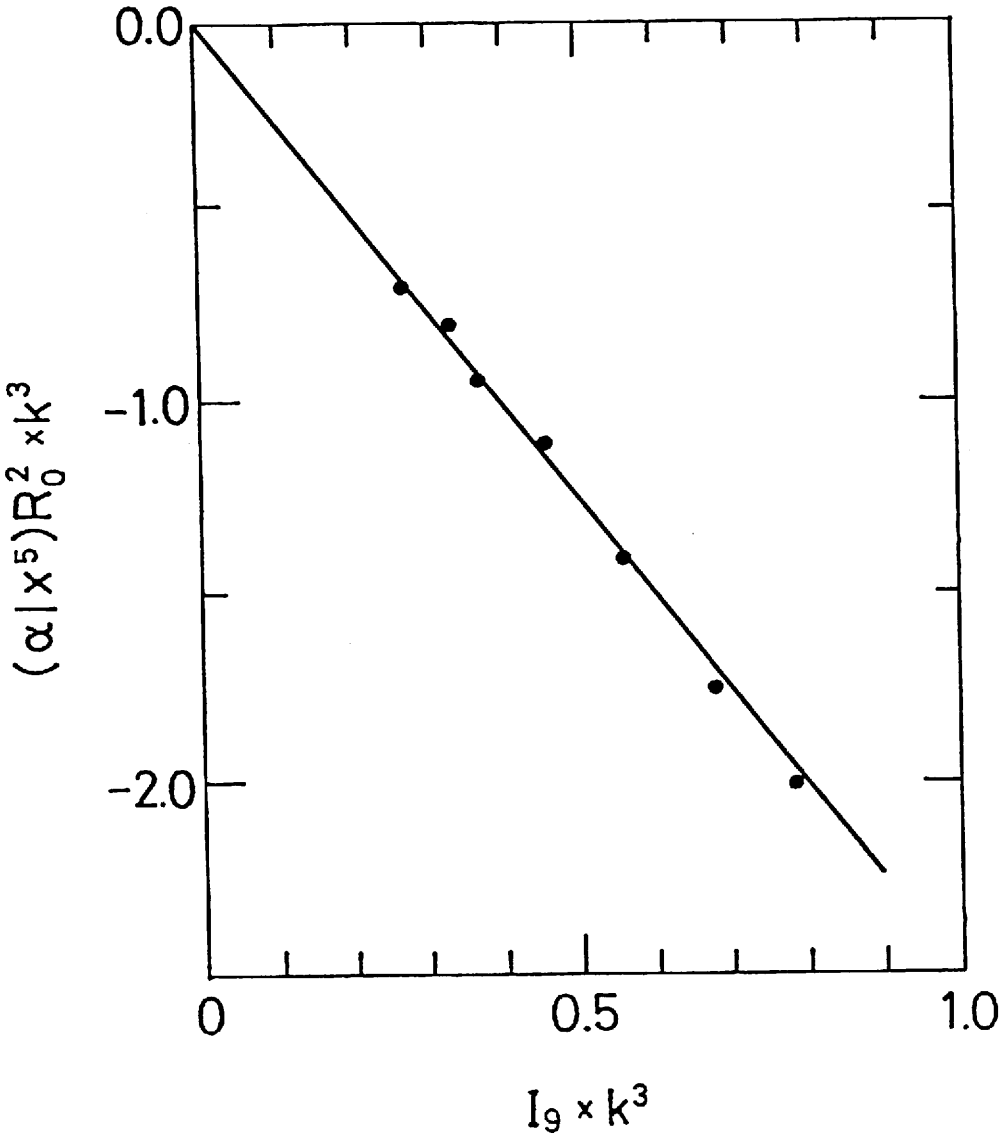

Fig.4.2.6 The relationship between the fifth order matrix element $(\alpha|x^5)$ and the fringing field integral I_9.

Table 4.2.1

Values of integrals for the fringing fields of electrostatic analyzers.

b/k	d/k	$I_5 \times k$	$I_9 \times k^3$
1.00	0.500	0.470	0.784
1.00	0.750	0.453	0.678
1.00	1.000	0.431	0.558
1.00	1.250	0.405	0.452
1.00	1.500	0.381	0.370
1.00	1.750	0.358	0.332
1.00	2.000	0.338	0.271
0.30[a]	0.485	0.724	3.266
0.72[b]	0.254	0.567	1.398
0.20[c]	0.508	0.769	4.658

a. b. c. These electrode structures are prepared in the computer program TRIO (Ref.4.2.7).

4.3 INFLUENCE OF HIGHER ORDER EFFECTS AND IMPERFECT BOUNDARY SHAPE OF MAGNET ON IMAGE ABERRATION

4.3.1 THE FIFTH-ORDER IMAGE ABERRATION IN THE FRINGING FIELD OF AN ELECTROSTATIC ANALYZER

The fifth-order matrix element $(\alpha|x^5)$ of the fringing field of an electrostatic analyzer (ESA) is obtained in the previous section 4.2; let us now estimate the image aberration of our prototype mass spectrometer constructed at our research laboratory whose ion optical system is similar to a grand scale mass spectrometer at Osaka University [4.3.1]. The displacement x at the collector slit of a mass spectrometer is expressed as

$$x=A_x\, x_0 + A_\alpha \tan\alpha_0 + A_{\alpha\alpha} \tan^2\alpha_0 + A_{\alpha\alpha\alpha} \tan^3\alpha_0 + \ldots \qquad (4.3.1)$$

where x_0 and α_0 are the displacement and inclination angle at the source slit, respectively and A_x, A_α, $A_{\alpha\alpha}$,....are the overall aberration coefficients. In general we have to use fifth order matrices to calculate the fifth-order aberration coefficients, but it is very difficult to obtain the fifth order matrices. We can, however, use a convenient approximation using first order matrices to estimate fifth order aberration. Three first-order transfer matrices are introduced in this estimation, i.e. the transfer matrix [C] representing the ion optical effect before the fringing field, [F] the fringing field and [B] after the fringing field. The overall transfer matrix [A] of a mass spectrometer is then obtained by the matrix multiplication [A]=[B][F][C]. In a first-order approximation, the displacement x_1 and the inclination angle α_1 at the entrance side of the boundary of the fringing field are given by

$$\begin{bmatrix} x_1 \\ \tan\alpha_1 \end{bmatrix} = \begin{bmatrix} (x|x)_c & (x|\alpha)_c \\ (\alpha|x)_c & (\alpha|\alpha)_c \end{bmatrix} \begin{bmatrix} x_0 \\ \tan\alpha_0 \end{bmatrix} \qquad (4.3.2)$$

where $(x|x)_c$,.... are the matrix elements of [C]. Similarly, x_2 and α_2 at the exit side of the boundary of the fringing field and x_3 and α_3 at the collector slit are expressed to the first-order approximation as

$$\begin{bmatrix} x_2 \\ \tan\alpha_2 \end{bmatrix} = \begin{bmatrix} (x|x)_f & (x|\alpha)_f \\ (\alpha|x)_f & (\alpha|\alpha)_f \end{bmatrix} \begin{bmatrix} x_1 \\ \tan\alpha_1 \end{bmatrix} \qquad (4.3.3)$$

$$\begin{bmatrix} x_3 \\ \tan\alpha_3 \end{bmatrix} = \begin{bmatrix} (x|x)_b & (x|\alpha)_b \\ (\alpha|x)_b & (\alpha|\alpha)_b \end{bmatrix} \begin{bmatrix} x_2 \\ \tan\alpha_2 \end{bmatrix} \qquad (4.3.4)$$

where $(x|x)_f$,.... are the matrix element of [F] and $(x|x)_b$,... are the matrix element of [B]. In the following discussion, we introduce the fifth-order matrix element $(\alpha|x^5)_f$ of [F]. Then, using the definition of the matrix formation, we can express the inclination $\tan\alpha_2'$ at the exit side of the boundary of the fringing field including $(\alpha|x^5)_f$ as

$$\tan\alpha_2' = (\alpha|x)_f\, x_1 + (\alpha|\alpha)_f \tan\alpha_1 + (\alpha|x^5)_f\, x_1^5 \qquad (4.3.5)$$
$$= \tan\alpha_2 + (\alpha|x^5)_f\, x_1^5$$

where we use Eqn.4.3.3. By using Eqn.4.3.2, the fifth-order term is expressed as

$$(\alpha|x^5)_f\, x_1^5 = (\alpha|x^5)_f\, (x|\alpha)_c^5 \tan^5\alpha_0 \qquad (4.3.6)$$

where we neglect the displacement x_0, because usually x_0 is negligibly small. Substituting $\tan\alpha_2'$ into Eqn.4.3.4 in place of $\tan\alpha_2$ and using Eqns.4.3.5, 4.3.6, we obtain the displacement x_3' at the collector slit including the fifth-order aberration as

$$x_3' = (x|x)_b\, x_2 + (x|\alpha)_b \tan\alpha_2 + (x|\alpha)_b\, (\alpha|x^5)_f + (x|\alpha)_c^5 \tan^5\alpha_0$$
$$= x_3 + A_{\alpha\alpha\alpha\alpha\alpha}\tan^5\alpha_0 \qquad (4.3.7)$$

where

$$A_{\alpha\alpha\alpha\alpha\alpha} = (x|\alpha)_b\, (\alpha|x^5)_f\, (x|\alpha)_c^5$$

and where $A_{\alpha\alpha\alpha\alpha\alpha}$ is the fifth-order aberration coefficient caused by the matrix element $(\alpha|x^5)_f$, which can be given by Eqn.4.2.9.

4.3.2 THE IMAGE ABERRATION CAUSED BY THE IMPERFECT BOUNDARY SHAPE OF A SECTOR MAGNETIC

Shape of the boundary

In the ion optical calculation by TRIO [4.3.1], the shape of the boundary of the magnet is assumed to be a circle having the radius ρ_0 and is expressed as

$$\rho(\theta) = \rho_0 \qquad (4.3.8)$$

where $\rho(\theta)$ and θ are defined in Fig.4.3. In the practical magnet, the shape cannot be exactly expressed by Eqn.4.3.8, because the magnet pole piece has a finite size and thus Eqn.4.3.8 is not exactly fulfilled near the edge of the pole piece. In this case, $\rho(\theta)$ should depend on θ and can be expressed by the power series expansion as

$$\rho(\theta) = \rho_0 + \rho_1\theta^1 + \rho_2\theta^2 + \rho_3\theta^3 + \rho_4\theta^4 + \rho_5\theta^5 + \rho_6\theta^6 + \ldots \qquad (4.3.9)$$

where $\rho_1, \rho_2, \rho_3, \ldots$ are coefficients. Higher order aberration in an ion optical system must arise from the higher order effect of the Eqn.4.3.9. Ideally, it should be possible to determine the constants using either an experimental measurement or a numerical calculation. Since these determination are almost impossible in actual case, we assume the boundary shape by polynomial as given in Eqn.4.3.9.

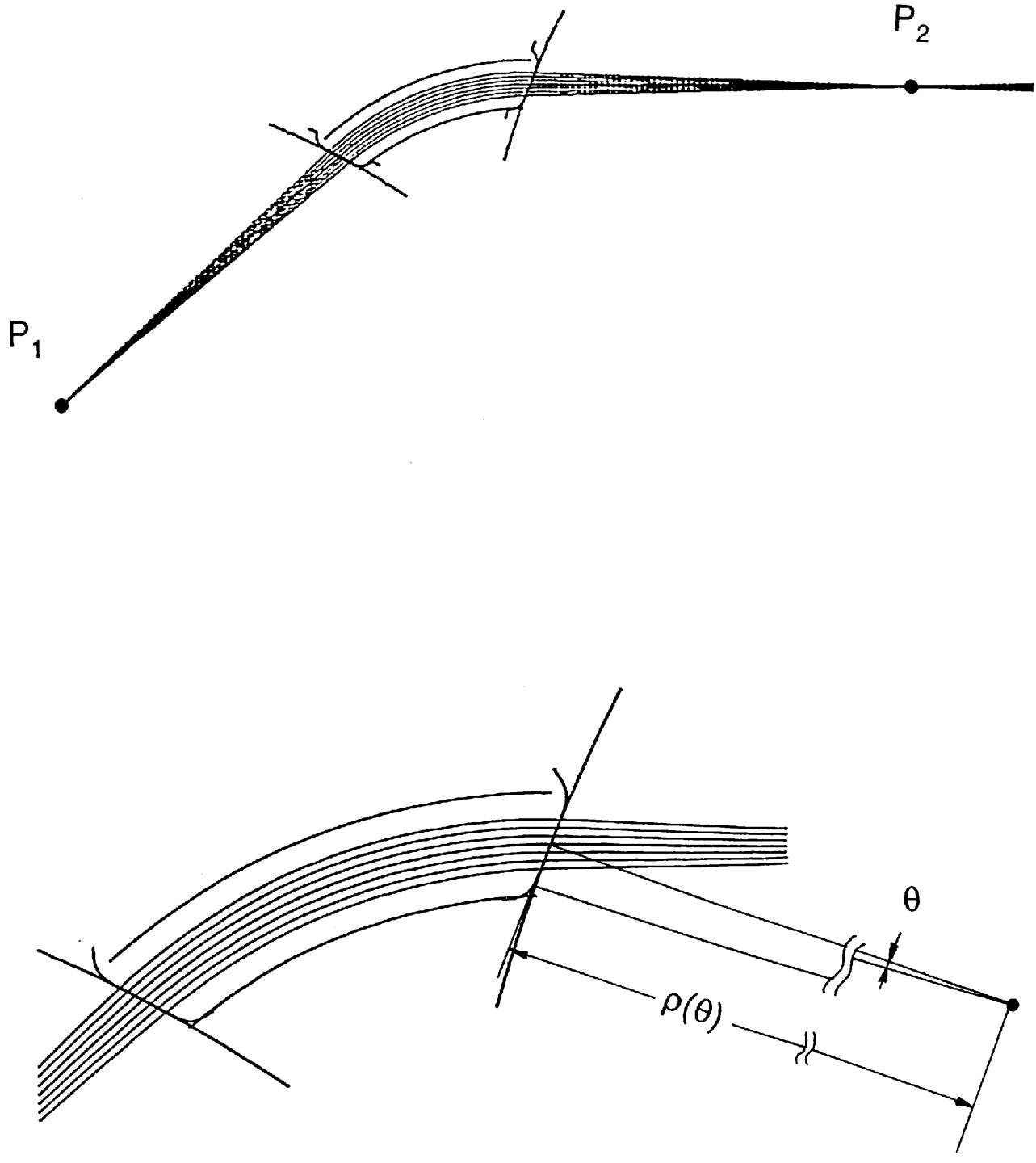

Fig. 4.3.1. Schematic drawing of a sector magnet and the ion calculated ion trajectries.

Ion trajectory calculation

The ion trajectories through a magnet were calculated by the program ELECTRA. The boundary of a magnet was given analytically by using Eqn.4.3.9. Figure 4.3.1 shows an example of the calculated ion trajectories. The ion optical effect was estimated as follows:

1) The ion trajectories leave from the position P_1 with arbitrary inclination angle α were calculated.
2) The displacement (aberration) $x(\alpha,\rho_1,\rho_2,\rho_3,\rho_4,\rho_5,\rho_6)$ of the ion from the optical axis at the focusing point P_2 was obtained from the calculated trajectories as a function of α, $\rho_1,\rho_2,....,\rho_6$.
3) The aberration caused by the imperfect boundary shape $\Delta x(\alpha,\rho_1,\rho_2,\rho_3,\rho_4,\rho_5,\rho_6)$ was estimated by the following expression

$$\Delta x(\alpha,\rho_1,\rho_2,\rho_3,\rho_4,\rho_5,\rho_6) = x(\alpha,\rho_1,\rho_2,\rho_3,\rho_4,\rho_5,\rho_6) - x(\alpha,0,0,0,0,0,0) \quad (4.3.10)$$

Image aberration of an ion optical system

We can now estimate the effect in a single magnet having imperfect boundary, the next step is to estimate the image aberration of a whole system. Suppose a system consisting a magnet and other ion optical components and characterize it by transfer matrices [A] and [B], where [A] is related to the region from the source slit to the position P_1 and [B] is related to the region from the position P_2 to the collector slit. In this case, the relationship between the inclination angle α_0 at the source slit and α_1 at P_1 is expressed in the first order approximation as

$$\alpha_1 = (\alpha|\alpha)_A\alpha_0 \quad (4.3.11)$$

where $(\alpha|\alpha)_A$ is a matrix element of [A]. The displacement Δx_2 at P_2 caused by the effect of the imperfect boundary is obtained from Eqns.4.3.10 and 4.3.11 as

$$\Delta x_2 = \Delta x\{(\alpha|\alpha)_A\alpha_0,\rho_1,\rho_2,\rho_3,\rho_4,\rho_5,\rho_6\} \quad (4.3.12)$$

This displacement is magnified by the matrix [B] then we obtain the displacement (aberration) at the collector slit as

$$\Delta x_c = (x|x)_B\ \Delta x\{(\alpha|\alpha)_A\alpha_0,\rho_1,\rho_2,\rho_3,\rho_4,\rho_5,\rho_6\} \quad (4.3.13)$$

where $(x|x)_B$ is a matrix elements of [B].

4.3.3 IMAGE ABERRATION OF A HIGH TRANSMISSION MASS SPECTROMETER

The relationship between the displacement (aberration) x_c at the collector slit and the

inclination angle α_0 at the source slit was obtained experimentally using the prototype mass spectrometer employing a QQBQE geometry [4.3.2]. The aberration coefficients of the instrument calculated up to third-order by TRIO is sufficiently small. However, for widely spread beam, the observed aberration was larger than the expectation. The difference between the third-order calculation and the experimental result is discussed.

Effect of the fifth-order aberration

Figure 4.3.2 shows the experimental and the calculated results of the relationship between the displacement Δx_c and the inclination angle α_0, where two kind of calculated values are shown: (a) Result from the third-order calculation by TRIO; (b) Result including the fifth order effect of fringing fields of ESA discussed in section 4.2 and the definite integrals for the quadrupole lenses discussed in section 4.1. It is shown that both calculations cannot explain the experimental result of large Δx_c. In this case, the fifth order effect of the ESA or the fringing field integrals of the quadrupole lenses are not major source of the large aberration.

Boundary shape of the magnet

Figure 4.3.3 shows the effect of the imperfect boundary shape of the magnet together with the experimental data. The parameters ρ_1, ρ_2,...,ρ_6 was determined so as to fit the experimental data. The calculated deviation can well explain the experimental data. Accordingly we can conclude that the large aberration observed for the case of very widely spread beam is probably caused by the imperfect boundary shape of the magnet.

REFERENCES

[4.3.1] T. Matsuo, H. Matsuda, Y. Fujita and H. Wollnik, Mass Spectrosc., 24(1976) 19.
[4.3.2] H. Matsuda, T. Matsuo, Y. Fujita,T. Sakurai and I. Katakuse, Int .J. Mass Spectrom. and Ion Proc., 91 (1989) 1.

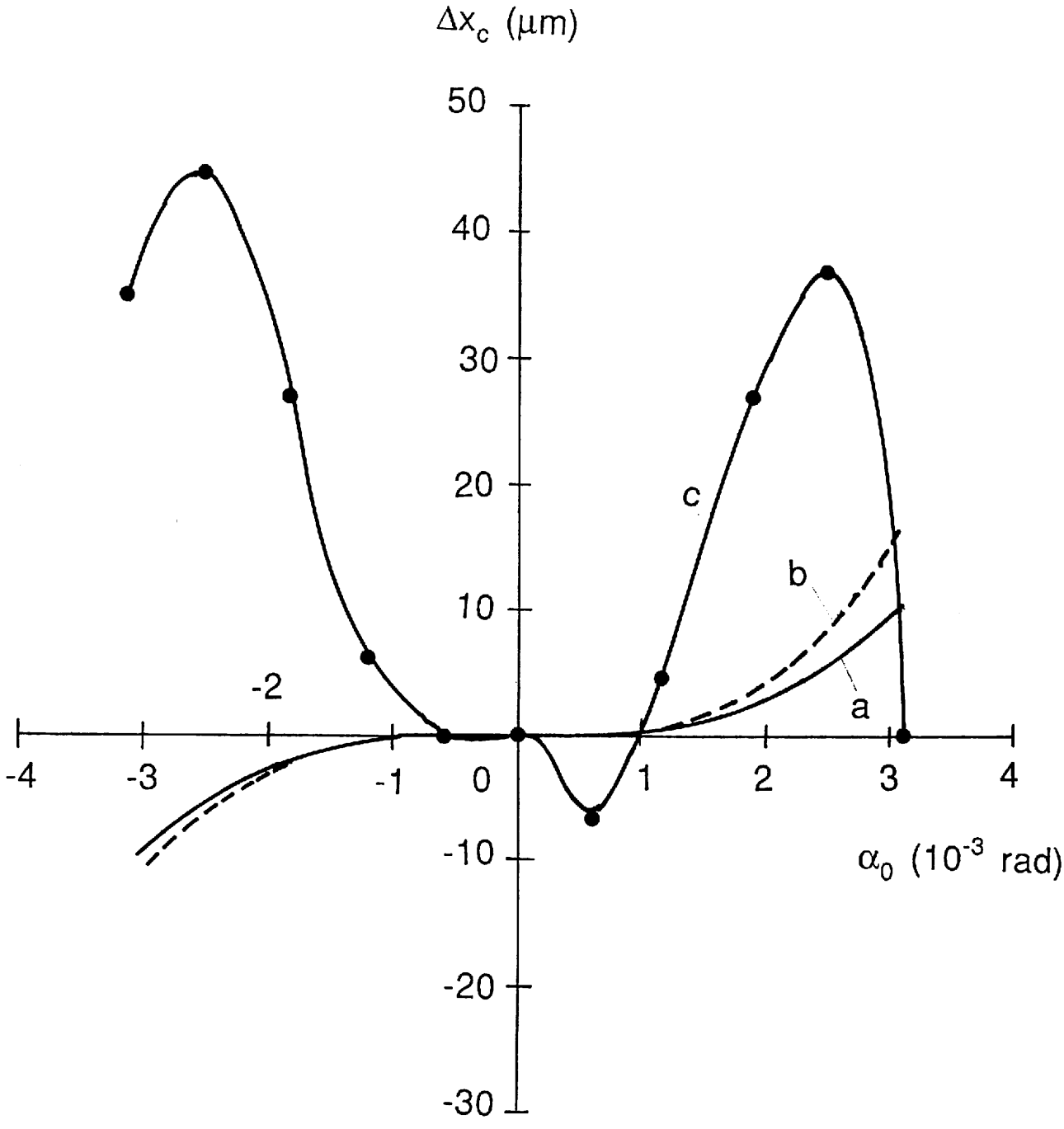

Fig. 4.3.2. Relationship between the inclination angle α_0 and the displacement Δx_c: (a) calculated by TRIO, (b) including fifth order aberration in the ESA and calculated fringing field distributions of quadrupole lenses,(c) experimental result.

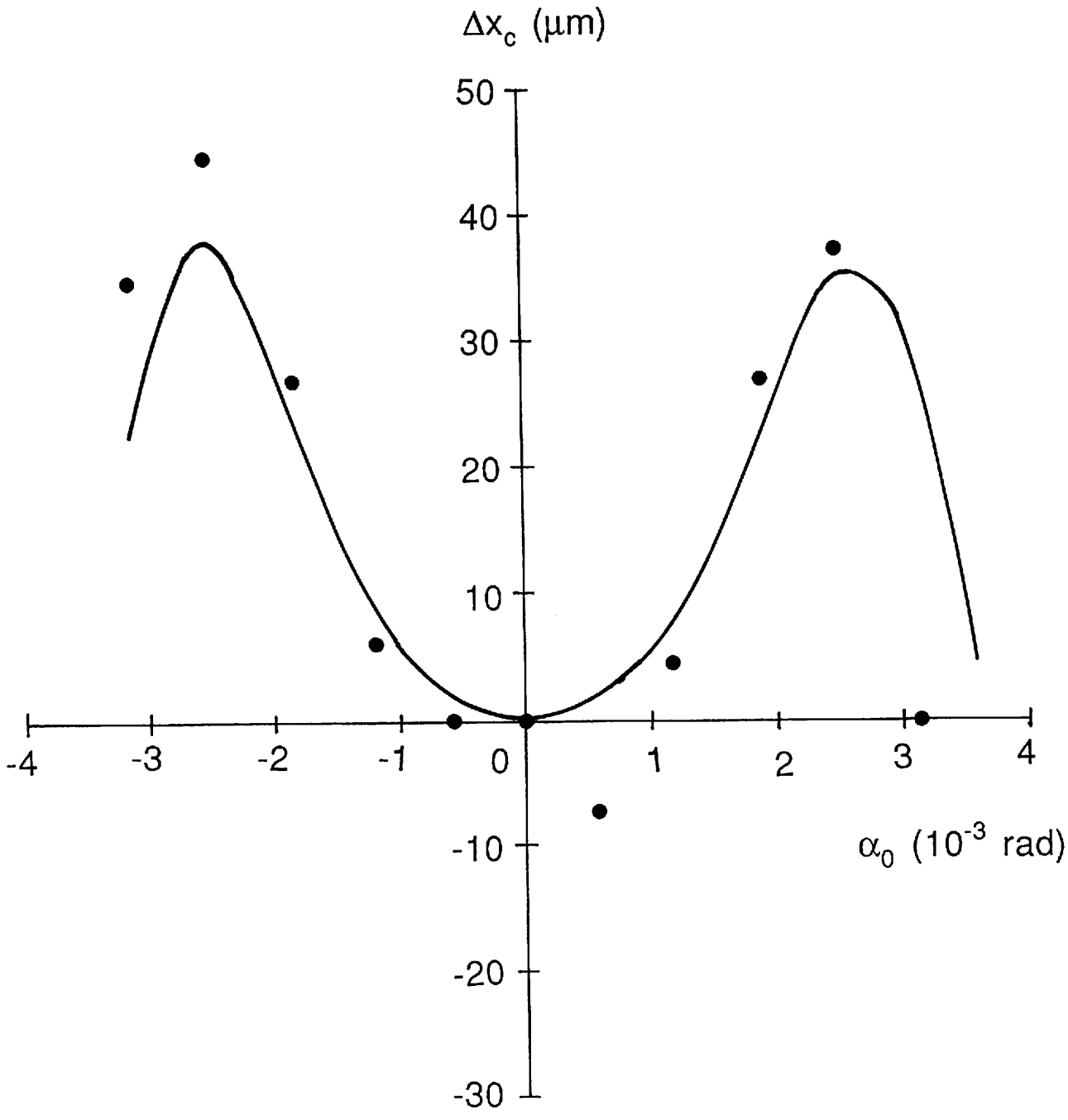

Fig. 4.3.3. Relationship between the inclination angle α_0 and the displacement Δx_c caused by imperfect boundary shape of the magnet. The experimental data (●) are also shown.

5. COMBINATION OF 'ELECTRA' AND 'MSPLEX'

5.1 DESIGN OF AN NMR MAGNET

5.1.1 INTRODUCTION

The magnetic field **B** obtained by an unsaturated pole piece can be expressed by a scalar magnetic potential V_m as

$$\mathbf{B} = \nabla \cdot V_m \qquad (5.1)$$

The scalar potential can be calculated by the program ELECTRA discussed in chapter 3. As an example of this type of calculations, the design of a shape of a magnet pole piece for an NMR spectrometer is described here. For a magnet of an NMR spectrometer, the homogeneity of the magnetic field in the region where sample material is located is very important. In the case of a wide gap magnet, the shape of the pole piece have to be well designed because the homogeneity depends on the shape of the pole piece. To find the optimum shape is, however, a tedious and time consuming process. In order to determine the optimum shape of the pole piece, the program MSPLEX was combined to ELECTRA. This combination of the field calculation program and the optimization program is very powerful. The charge density method is very suitable for this calculation, because the mesh generation of this method is quite simple.

5.1.2 CALCULATION METHOD

Let us design, as an example, a electromagnet with 10 cm gap width and 12.5 cm diameter pole piece (see Fig 5.1a). It is required that the homogeneity of the magnetic field in the region of the center of the magnet of 2.5 cm cubic is very high. The homogeneity η is defined

$$\eta = 1/12 \sum_{i=1}^{12} [\{B(r_i) - B\}^2 / B^2]^{1/2} , \quad B = 1/12 \sum_{i=1}^{12} B_i \qquad (5.2)$$

$$r_i = 0.1i \text{ (cm)} , \; i = 1,2,...,12$$

When the pole piece is an ordinal flat shape, the calculated value of homogeneity is only 2.6×10^{-3}. The homogeneity η depends on the positions (R_k, z_k) of the surface of the pole piece. For simplicity, the six points of the surface of the pole piece are varied and the r coordinate of these points are fixed: R_1=1.0, R_2=2.0, R_3=3.0, R_4=4.0, R_5=5.0, R_6=6.25. Then what we have to do is to find the positions z_k that minimize the function $\eta(z_1, z_2, ..., z_6)$. The values of this function are minimized by using ELECTRA and MSPLEX.

The calculation procedure is as follows: (1) The parameters z_k is given from

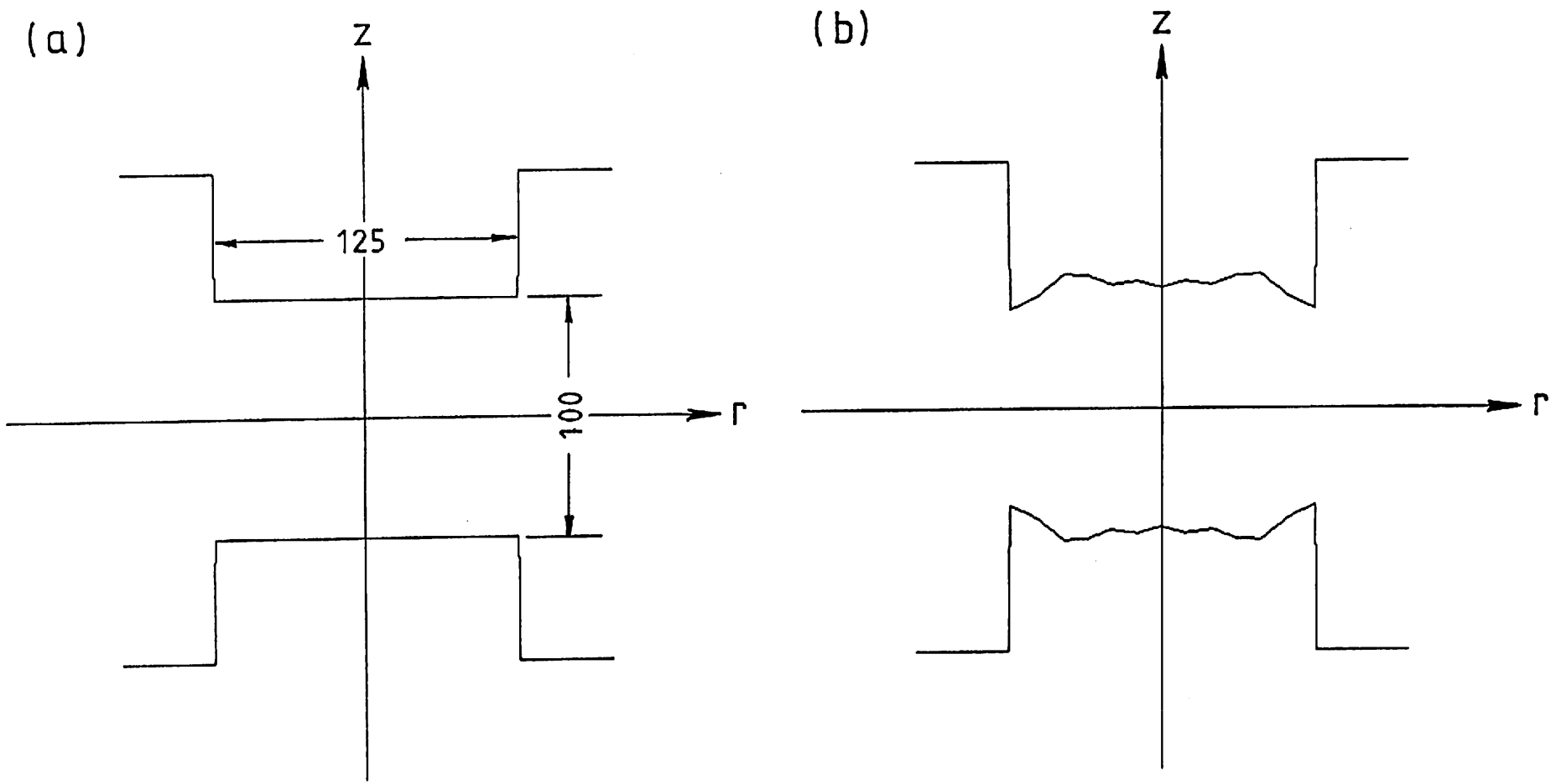

Fig. 5.1. Drawing of shapes of pole piece (a) before (b) after optimization.

MSPLEX; (2) ELECTRA calculate the magnetic fields under the given parameter and then the homogeneity η is evaluated; (3) By varying the parameters z_k on the basis fo the simplex method, the parameters approach the optimum values.

5.1.3 RESULTS AND DISCUSSION

Figures 5.1a,b shows the initial and the final shapes of the pole piece. The homogeneity of each search step are shown in Fig.5.2. The final homogeneity was 1.6×10^{-5}; the homogeneity is 160 times improved by 100 iterations. The computation time for the calculation was about 20 minutes with an HP 9000-370 computer (Engineering Work Station).

In this study, the automatic design of the shapes of the boundaries becomes possible. This will be helpful for design or improve wide gap magnets.

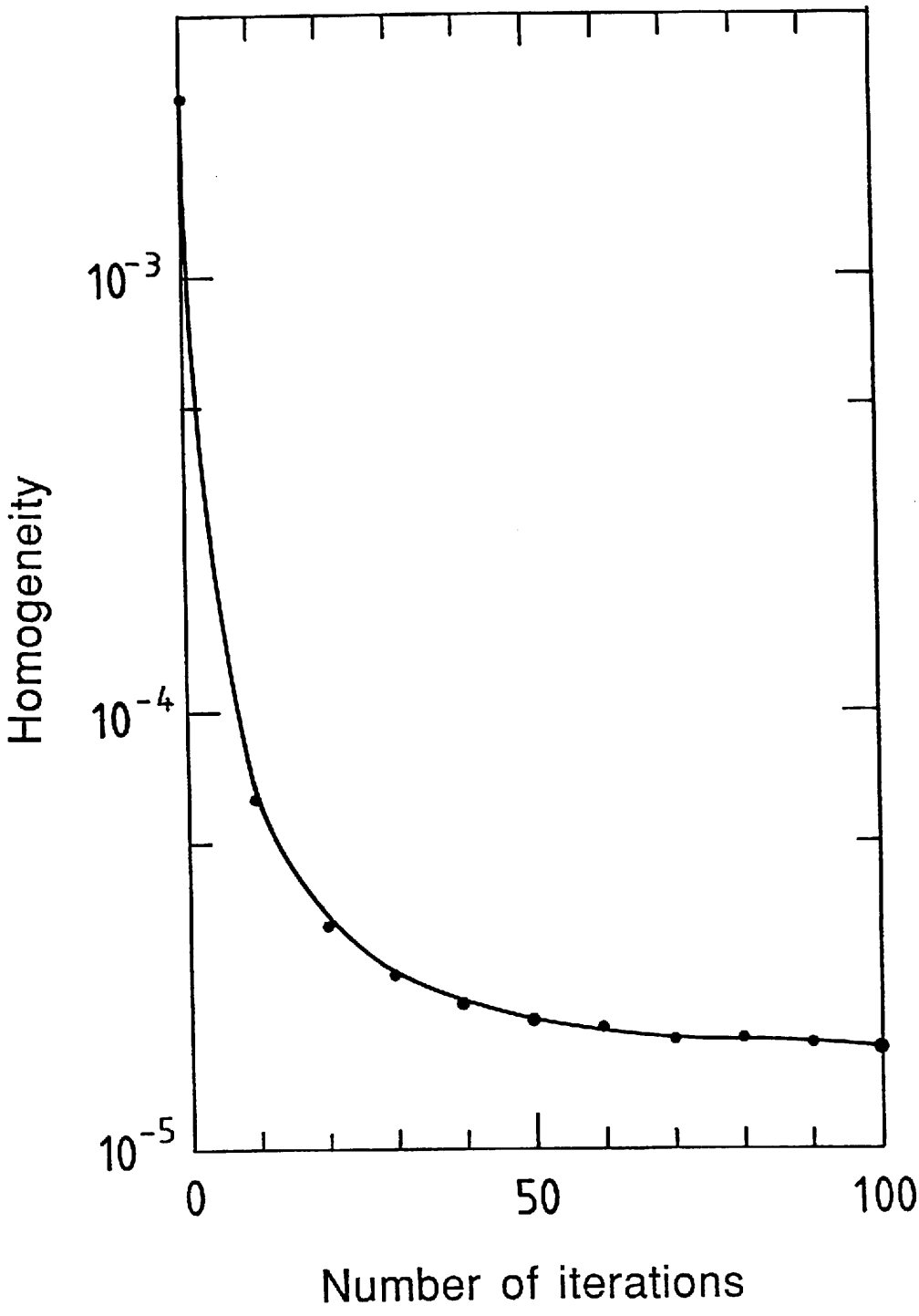

Fig. 5.2. Calculated homogeneity vs number of iterations.

5.2 RETARDATION LENS FOR HYBRID MASS SPECTROMETER

5.2.1 INTRODUCTION

In recent years tandem mass spectrometry has been developed rapidly as a powerful tool for analysis of organic and inorganic compounds [5.1]. The principle of this method is that first a parent ion is selected by first mass analyzer(MS1), second it is dissociated to daughter ions and finally the daughter ion mass spectrum is recorded by second mass analyzer(MS2). Many types of instruments have been proposed and constructed: for example four sector instruments consisting of two double focusing mass analyzers discussed in Chapter 2.4., multi-quadrupole instruments [5.2] and hybrid instruments consisting of a double focusing mass analyzer as MS1 and quadrupole mass filter as MS2 [5.3]. In the last system, special considerations are required for the 'matching' of ion beam profile between two mass analyzers. In case of the hybrid instrument, the main difficulty of the 'matching' arises from the large kinetic energy difference in between MS1 and MS2. The kinetic energy of ions in a sector type mass analyzer is in the order of keV; on the other hand, that in a quadrupole mass filter is around 10 eV. In this case, therefore, a retardation lens between MS1 and MS2 is absolutely necessary.

A direct simulation of ion trajectories using a ray tracing method was introduced to design such lens system. We demonstrate here the ability of the program ELECTRA combined with the program MSPLEX for designing such retardation lens.

5.2.2 THEORETICAL DESCRIPTION OF THE PROBLEM

Figure 5.3 shows a schematic block diagram of the hybrid mass analyzer consisting of a sector mass analyzer and a quadrupole mass filter. The retardation lens is located between the sector mass analyzer(MS1) and the quadrupole mass filter (MS2).

Let us discuss the determination of lens potentials V_1, V_2, V_3 of an axially symmetric lens system consisting of three lens plates shown in Fig. 5.4. In the design of the lens system, we have to determine lens geometry and lens potentials. Ideally we can search for both optimum lens geometry and applied potentials; however, we focus here the discussion on the determination of the applied lens potentials for a given lens structure.

Figure 5.3 also shows the diagram of the potential among the optical axis. MS1 is usually kept in the earth potential, while the potential of MS2 is 99.7% of the source potential V_a. Therefore the kinetic energy of the ion has to decrease by a factor of 3/1000.

Ion optical consideration of 'figure of merit'

In order to determine the optimum lens potential, we have to define the figure of merit of the system; let us discuss this here. Let $P_i(x_i,\alpha_i)$ is an ion optical position vector at the entrance of the lens system and $P_o(x_o,\alpha_o)$ is that at the exit. The

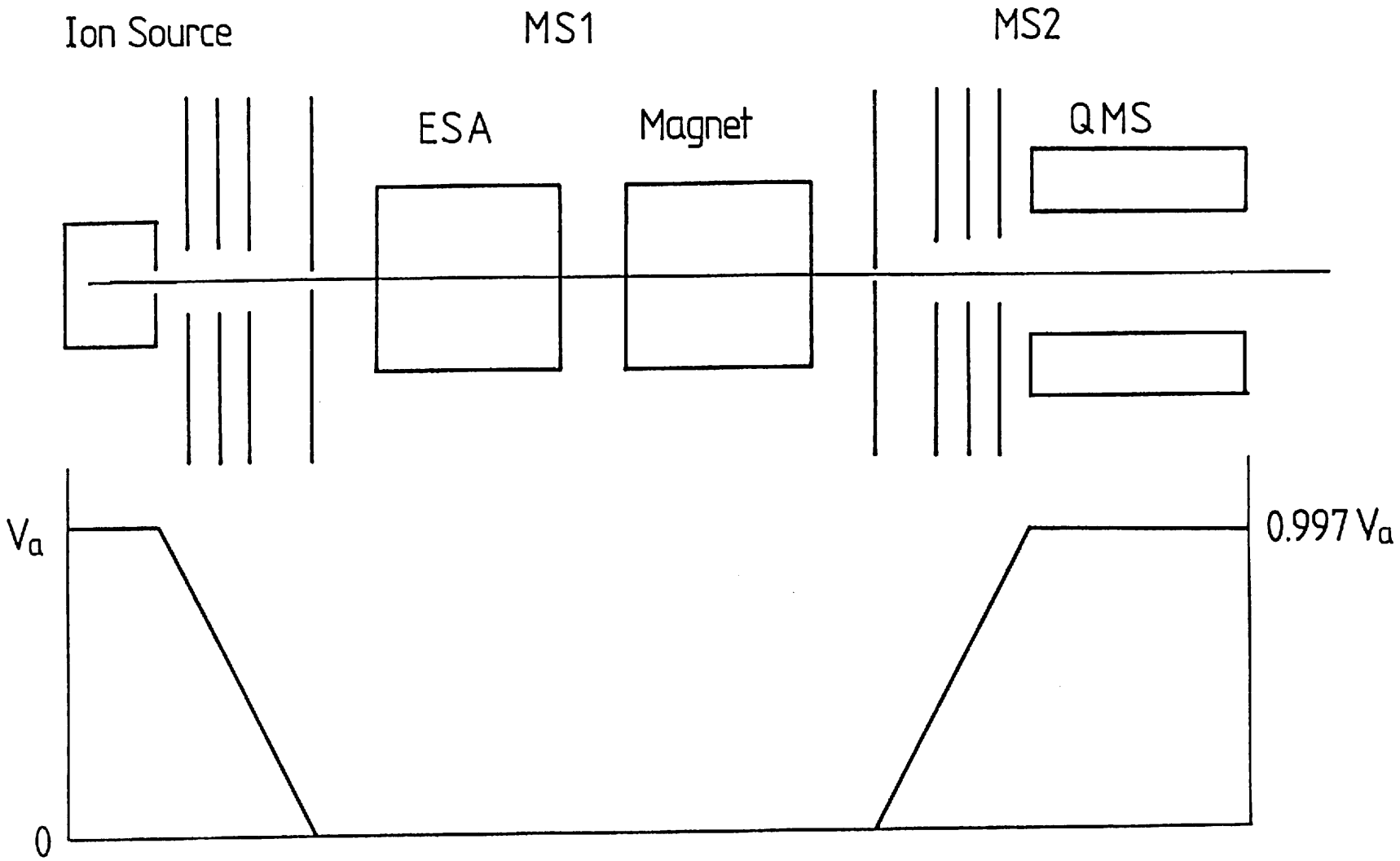

Fig. 5.3. Schematic drawing of a hybrid mass spectrometer and its potential distribution.

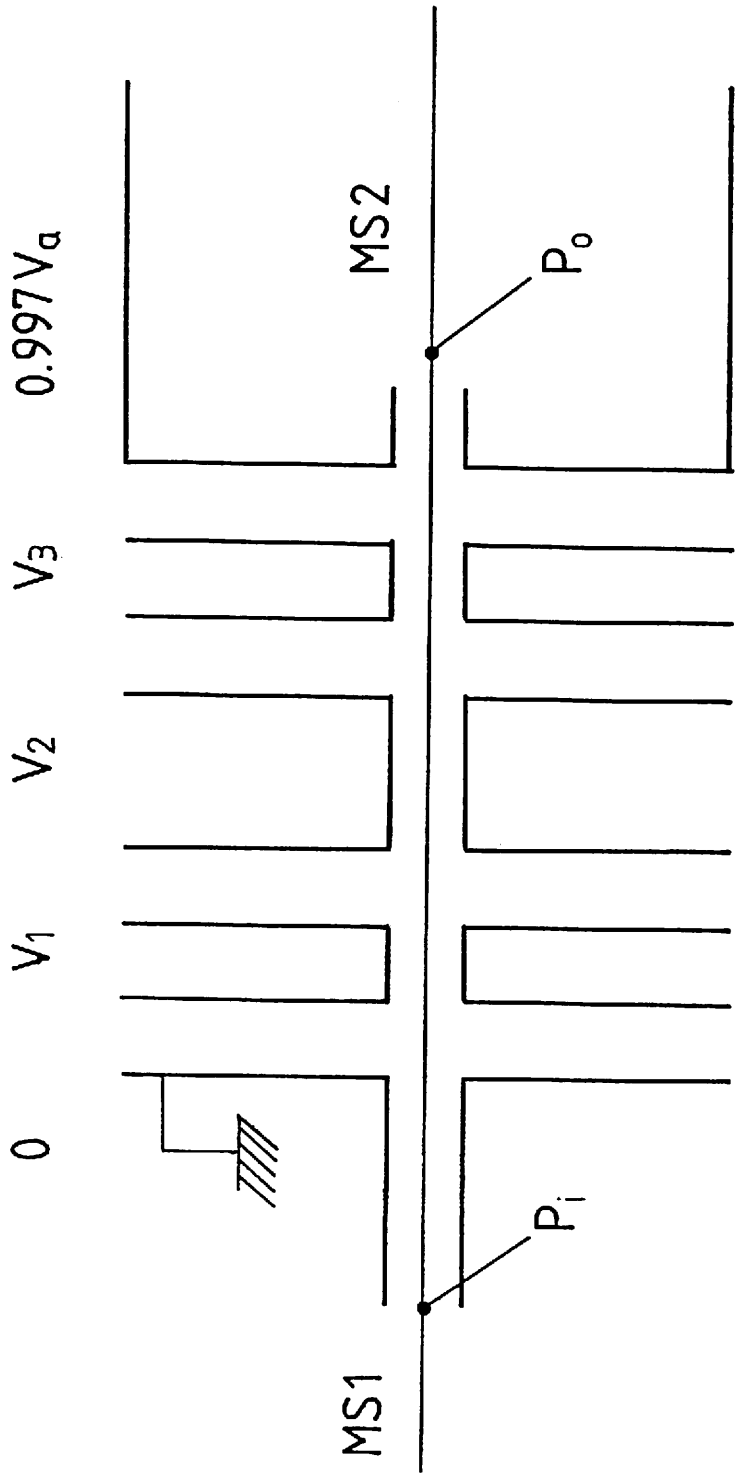

Fig. 5.4. Schematic drawing of the retardation lens to be studied.

relationship between these two vectors can be expressed by a first order transfer matrix as

$$\begin{bmatrix} x_o \\ \alpha_o \end{bmatrix} = \begin{bmatrix} (x|x) & (x|\alpha) \\ (\alpha|x) & (\alpha|\alpha) \end{bmatrix} \begin{bmatrix} x_i \\ \alpha_i \end{bmatrix} \qquad (5.3)$$

The determinant of the matrix is given [5.2.4] as

$$\begin{vmatrix} (x|x) & (x|\alpha) \\ (\alpha|x) & (\alpha|\alpha) \end{vmatrix} = \sqrt{(V_i - V_a)/(V_o - V_a)} \qquad (5.4)$$

When $V_i = V_o$, the value is unity; however in the case of the retardation lens system discussed here, the value of the determinant of the matrix becomes 18.25. Therefore the matrix elements tend to have large values ; this means that the beam tends to diverse. In order to optimize the ion transmission through MS1 to MS2, the divergence of the beam has to be minimized.

Suppose that the ion beams from MS1 have following conditions

$$-x_m \le x_i \le x_m$$

$$-\alpha_m \le \alpha_i \le \alpha_m \qquad (5.5)$$

and suppose that MS2 accepts the ion beam having following conditions

$$-x_s \le x_o \le x_s$$

$$-\alpha_s \le \alpha_o \le \alpha_s \qquad (5.6)$$

Then we can define a function $F(V_1,V_2,V_3)$ to be minimized as

$$F(V_1,V_2,V_3) = \{ |(x|x)|x_m + |(x|\alpha)|\alpha_m \}/x_s + \{ |(\alpha|x)|x_m + |(\alpha|\alpha)|\alpha_m \}/\alpha_s \qquad (5.7)$$

The first term of the function is the maximum beam size normalized by the maximum acceptable beam size and the second term is the maximum inclination angle normalized by the maximum acceptable inclination angle.

5.2.3 CALCULATION METHODS

In this study, $F(V_1,V_2,V_3)$ is calculated as follows: first, two trajectories of paraxial trajectories are calculated by ELECTRA: second, the transfer matrix is obtained from Eqn.5.3 using the results of the trajectory calculation: finally the function $F(V_1,V_2,V_3)$ is evaluated from the obtained matrix elements.

The potentials V_1, V_2, V_3 are optimized by the program MSPLEX. The calculation

procedure is as follows: (1) the values of the potentials of the nodes on the lens electrodes are given by MSPLEX: (2) then ELECTRA calculate the electric field and ion trajectories. In this process, once the coefficients of the system of the linear equations (see chapter 3) have been calculated, then they are stored and are unnecessary to recalculate, because these coefficients do not change as far as the geometry of the lens system dose not change:(3) the function $F(V_1,V_2,V_3)$ is evaluated from the calculated trajectories.

5.2.4 RESULTS AND DISCUSSION

Step size

We have to check the influence of a step size in the trajectory calculation. The relationship between the error E in the trajectory and the step size h of the integration is estimated as

$$E \propto h^4 \qquad (5.8)$$

Accordingly we should check the accuracy of the ray tracing by changing the step size. Figure 5.5 shows the influence of the step size on the calculated trajectories, where the step size h is varied from 10mm to 4mm. It is clearly shown that the step size less than 6mm gives enough accuracy.

Determination of lens potential

We assume here the beam conditions from MS1 (x_m,α_m) and the acceptance of MS2 (x_s,α_s) as

x_m = 1.0 mm $\quad \alpha_m$ = 0.01 rad

x_s = 1.0 mm $\quad \alpha_s$ = 0.1 rad

Figure 5.6. shows the ion trajectories in the case of before optimizing the lens potentials: V_1=0.50V_a, V_2= 0.90V_a, V_3= 0.98V_a. It is clearly shown that the ion beam widely spreads at the entrance of the MS2. In this case the transfer matrix of the lens system is calculated to

$$\begin{bmatrix} -3.05 & -94.1 \\ -0.01 & -6.45 \end{bmatrix}$$

Figure 5.7 shows the ion trajectories after optimizing the lens potential:V_1 = 0.649V_a, V_2= 0.847V_a, V_3= 0.950V_a. For obtaining this condition, twenty steps were required in the optimizing processes. The transfer matrix of the lens system becomes

$$\begin{bmatrix} -1.23 & -17.0 \\ 0.01 & -14.6 \end{bmatrix}$$

Compared with Fig. 5.6, the ion beam shown in Fig 5.7 is well focused at the entrance of the MS2.

From the results in this section, we can conclude that the program ELECTRA is very powerful for the design of lens systems where the applied lens potential and the kinetic energy of the charged particle vary widely. It is also shown that the combination of ELECTRA and MSPLEX has an excellent ability for automatic design of ion optical systems.

REFERENCES

[5.1] F.W. McLafferty, Ed., Tandem Mass Spectrometry, John Wiley and Suns, New York, 1983.

[5.2] R.A. Yost and C.G. Enke, Anal. Chem. 51 (1979) 1251A.

[5.3] J.D. Ciudek, J.W. Amy and R.G. Cooks, Int. J. Mass Spectrm. Ion Processes 65 (1985) 141.

[5.4] P. Grivet, Electron optics Part 1, Pergamon Press, Oxford, 1972.

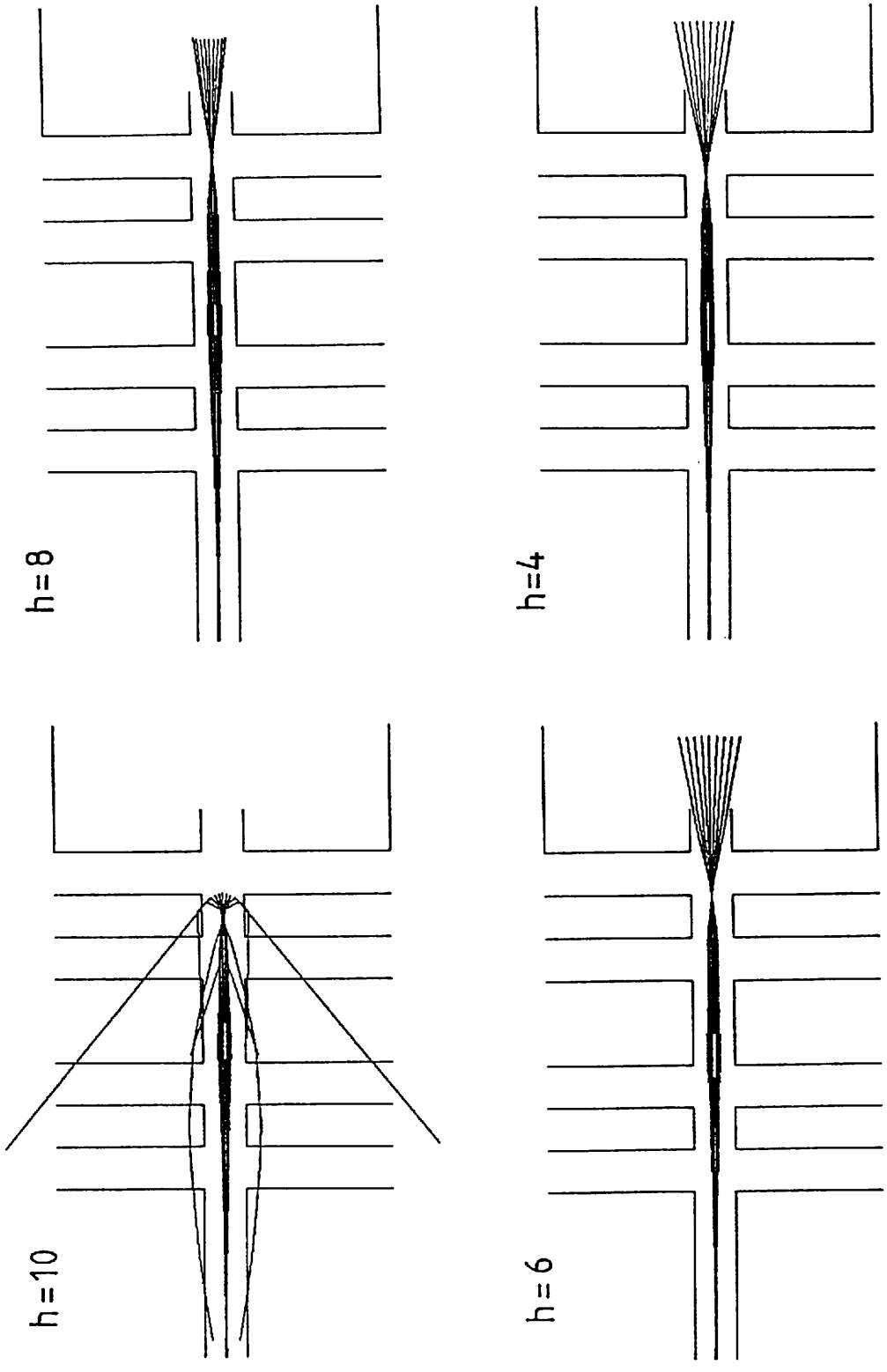

Fig. 5.5. Influences of the step size h on calculated ion trajectories.

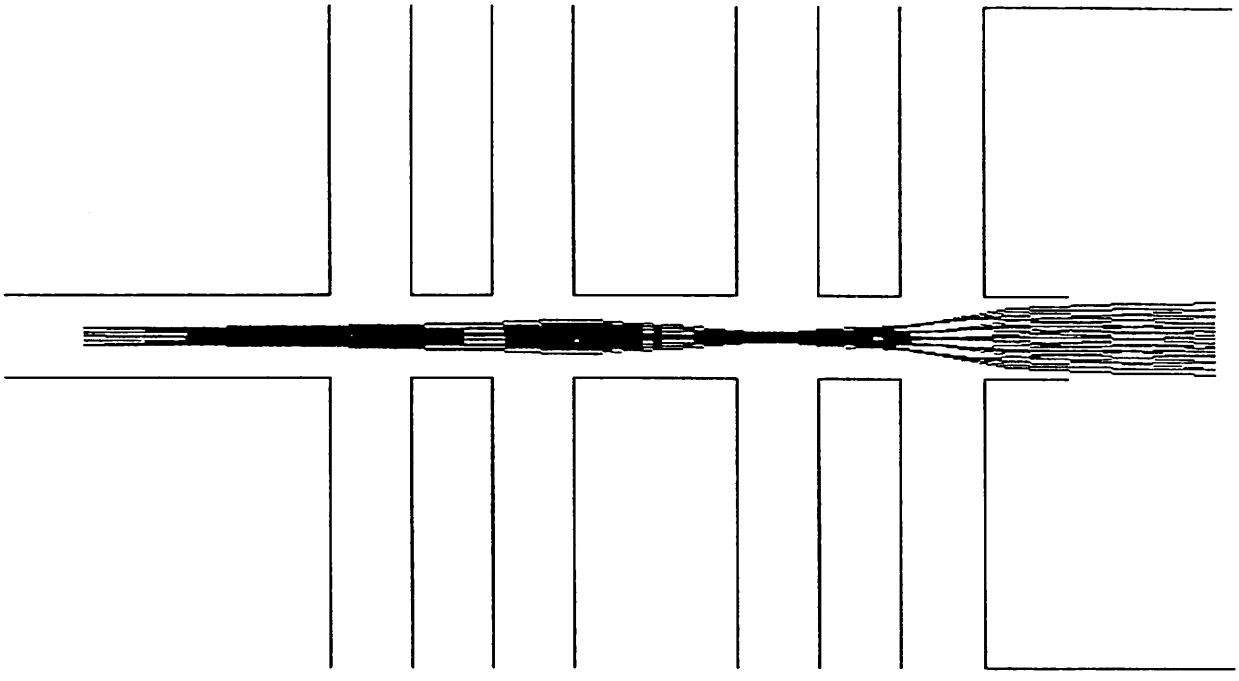

Fig. 5.6. Ion trajectories before optimization.

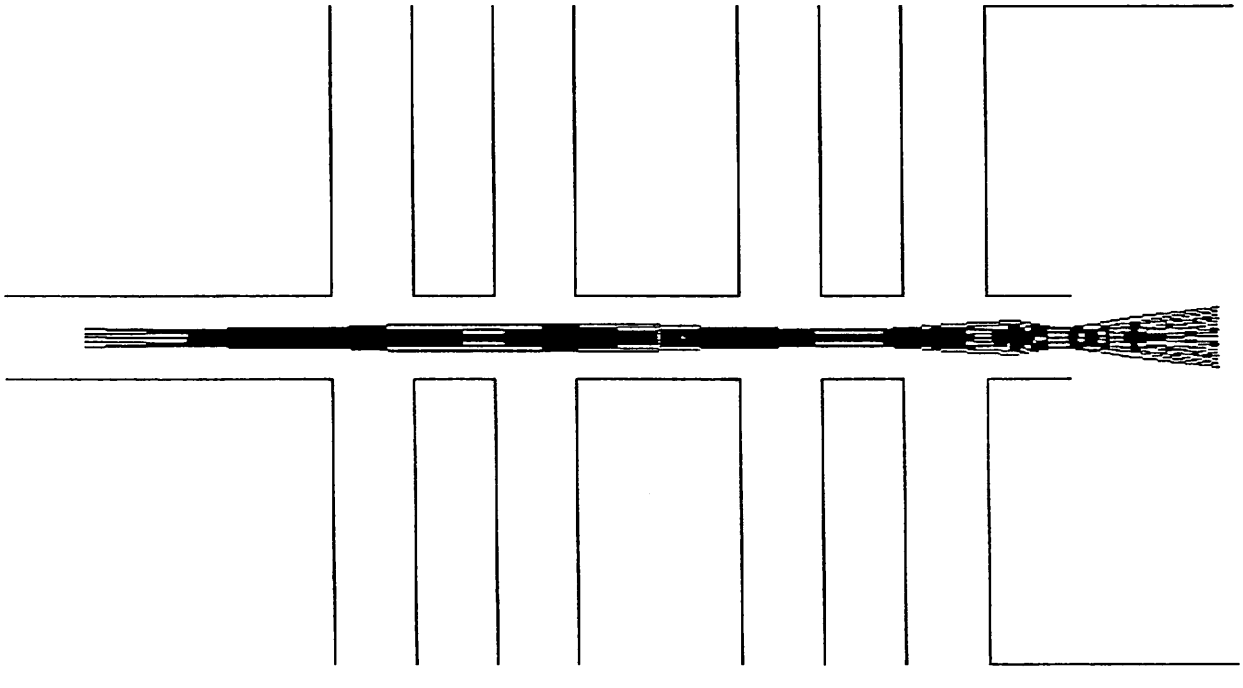

Fig. 5.7. Ion trajectories after optimization.

6. CONCLUSION

(1) The development of ion optics.

The method of calculation and optimization of ion trajectories in electric and magnetic fields was investigated, especially for widely spread ion beam. Two computer programs have been developed: One is the parameter search program MSPLEX based on the simplex method. The other is the ray tracing program ELECTRA based on the charge density method and the Runge-Kutta method.

(2) The design and construction of a high performance mass spectrometer and a tandem mass spectrometer.

A new high performance mass spectrometer having large radius of magnet was proposed and constructed. Though having large radius r_m = 0.72m, the magnet size is acceptable by choosing the small deflection angle w_m =40° and the higher order aberrations are satisfactory small. Mass resolution, mass range were examined by experiments and turned out to be in good agreement with theoretical expectations. The mass spectra of organic biopolymer such as bovine insulin were successfully obtained.

A tandem mass spectrometer consisting of two new mass spectrometers was proposed and constructed. The quadrupole triplet interface was introduced to connect two mass spectrometers efficiently. By selecting suitable electric potential of quadrupole, two types of operation (1) MS/MS mode and (2) enhanced resolution mode could be executed. In MS/MS operation, we could demonstrate the characterization of hemoglobin variant quite easily.

An apparatus which can vary the mass dispersion on focal plane was proposed and constructed in order to detect weak intensity ion beams having different masses simultaneously.

(3) The application of the ray tracing program ELECTRA

The large image aberrations due to wide spread of ion beams were observed by experiments. They could be well explained by the ray tracing calculations. The higher order effects in the fringing fields of electrostatic analyzer and quadrupole lens were estimated. It was impossible to treat such phenomena by an ordinary transfer matrix method.

The methods of design of a wide gap magnet having high homogeneity and a retardation lens system were investigated. These two systems will produce interest results in the near future.

APPENDIX

The relationship between $A_\gamma=(x|\gamma)_A$ and $\theta_\alpha$is obtained as follows: By using matrix elements of [A], θ_α is given by[2.5.5]

$$\tan\theta_\alpha = -\,(\alpha|\alpha)_A((x|\gamma)_A(\alpha|\alpha)_A - (x|\alpha)_A(\alpha|\gamma)_A)/(\,(x|\alpha\gamma)_A-(\alpha|\alpha)_A-(x|\alpha)_A(\alpha|\alpha\gamma)_A) \tag{A-1}$$

Similar to Eqns 2.5.7,2.5.8 in chapter 2, we obtain

$$\begin{vmatrix} (x|\alpha)_A & (x|\gamma)_A \\ (\alpha|\alpha)_A & (\alpha|\gamma)_A \end{vmatrix} = \begin{vmatrix} (x|x)_C & (x|\alpha)_C \\ (\alpha|x)_C & (\alpha|\alpha)_C \end{vmatrix} \begin{vmatrix} (x|\alpha)_B & (x|\gamma)_B \\ (\alpha|\alpha)_B & (\alpha|\gamma)_B \end{vmatrix} = \begin{vmatrix} (x|\alpha)_B & (x|\gamma)_B \\ (\alpha|\alpha)_B & (\alpha|\gamma)_B \end{vmatrix} \tag{A-2}$$

Here we use the conservation of phase space volume:

$$\begin{vmatrix} (x|x)_C & (x|\alpha)_C \\ (\alpha|x)_C & (\alpha|\alpha)_C \end{vmatrix} = 1 \tag{A-3}$$

The values of the second order elements of [C] related to x, α and γ such as $(x|xx)_C$, $(x|x\alpha)_C$, $(x|\alpha\alpha)_C$, $(x|x\gamma)_C$, $(x|\alpha\gamma)_C$, $(x|\gamma\gamma)_C$, $(\alpha|xx)_C$, $(\alpha|x\alpha)_C$,$(\alpha|\alpha\alpha)_C$, $(\alpha|x\gamma)_C$, $(\alpha|\alpha\gamma)_C$, $(\alpha|\gamma\gamma)_C$ are zero[4]. Thus we obtain

$$\begin{bmatrix} (x|\alpha)_A & (x|\alpha\gamma)_A \\ (\alpha|\alpha)_A & (\alpha|\alpha\gamma)_A \end{bmatrix} = \begin{bmatrix} (x|x)_C & (x|\alpha)_C \\ (\alpha|x)_C & (\alpha|\alpha)_C \end{bmatrix} \begin{bmatrix} (x|\alpha)_B & (x|\alpha\gamma)_B \\ (\alpha|\alpha)_B & (\alpha|\alpha\gamma)_B \end{bmatrix} \tag{A-4}$$

and using Eqn(A-3) we obtain

$$(x|\alpha)_A(\alpha|\alpha\gamma)_A - (x|\alpha\gamma)_A(\alpha|\alpha)_A = (x|\alpha)_B(\alpha|\alpha\gamma)_B - (x|\alpha\gamma)_B(\alpha|\alpha)_B \tag{A-5}$$

By using the focusing condition, $(x|\alpha)_A = 0$, $(\alpha|\alpha)_A$ can be given as

$$(\alpha|\alpha)_A = -((x|\alpha)_A(\alpha|\gamma)_A - (x|\gamma)_A(\alpha|\alpha)_A) \,/\, (x|\gamma)_A \tag{A-6}$$

By substituting Eqns(A-2),(A-5) and (A-6) into Eqn(A-1) , the relationship between the mass dispersion A_γ and θ_α is given as

$$\tan\theta_\alpha = K \,/\, A_\gamma \tag{A-7}$$

where

$$K = -\,\{(x|\gamma)_B(\alpha|\alpha)_B - (x|\alpha)_B(\alpha|\gamma)_B\}^2/\{(x|\alpha\gamma)_B(\alpha|\alpha)_B - (x|\alpha)_B(\alpha|\alpha\gamma)_B\} \tag{A-8}$$

The constant K only depends on the original double focusing system (from the source slit to the exit of the magnetic sector).

ACKNOWLEDGEMENTS

The author would like to express his sincere appreciation to Professor Takekiyo Matsuo of Osaka University, under whose guidance the work was conducted and completed. He also wishes to express sincere gratitude to Professor Tadanori Minamisono of Osaka University for encouragement and many useful suggestions and advice. He expresses his thanks to Mr. Yoshihiro Kammei and the staff of MS group of JEOL Ltd. Akishima Tokyo for their technical supports throughout this study. Many thanks are also due to Associate Professor Itsuo Katakuse for his encouragement and the technical suggestions of measuring cluster spectra, to Medical Dr. Yoshinao Wada of Osaka Medical Center for Maternal and Child Health for the provision of hemoglobin variant samples and the discussion concerning to biological problem, and to Dr. Toru Sakurai for enlightening discussions of basic ion optics and proof reading of the original manuscript. Acknowledgment is due to the staff of Matsuo laboratory for help with the preparation of this thesis.

He would like to express his thanks and appreciation to Professor Klaus Biemann of Massachusetts Institute of Technology for the provision of instrument time of a tandem mass spectrometer and for kind guidance of the basic knowledge of peptide chemistry. He is much indebted to Professor Hisashi Matsuda for guiding him into the field of mass spectrometry.